Soft X-ray Spectroscopy of Organic and Organometallic Molecules and Polymers

A Thesis Submitted to the
College of Graduate Studies and Research
In Partial Fulfillment of the Requirements
For the Degree of Doctor of Philosophy
In the Department of Chemistry
University of Saskatchewan
Saskatoon, Saskatchewan

By
Edwige Otero

PERMISSION TO USE

In presenting this thesis in partial fulfillment of the requirements for a postgraduate degree from the University of Saskatchewan, I agree that the libraries of this University may make it freely available for inspection. I further agree that permission for copying of this thesis in any manner, in whole or in part, for scholarly purposes may be granted by Dr. S.G. Urquhart who supervised my thesis work or, in his absence, by the department Head of the Department of Chemistry or the Dean of the College of Graduate Studies and Research in which my thesis work was done. It is understood that any copy or publication or use of this thesis or parts thereof for financial gain shall not be allowed without my written permission. It is also understood that due recognition shall be given to me and to the University of Saskatchewan in any use which may be made of any material in my thesis.

Request for permission to copy or to make other use of material in this thesis in whole or in part should be addressed to:

The Head
Department of Chemistry
University of Saskatchewan
Saskatoon, Saskatchewan
Canada S7N 5C9

ABSTRACT

In this thesis, two aspects of research in soft X-ray absorption spectroscopy chemistry are explored. The first objective was to measure the natural circular dichroism of small chiral organic molecules at soft X-ray wavelengths. The second objective was to characterize the electronic structure and spectra of a series of organometallic polymers.

The goal of the first part of this thesis was to enhance the sensitivity of Near Edge X-ray Absorption Fine Structure (NEXAFS) spectroscopy to the intrinsic "handedness" of chiral organic molecules. The phenomenon of X-ray natural circular dichroism (XNCD) has been well described by theoreticians; however, there have been few successful measurements reported, mainly due to the weakness of the effect and the difficulty of preparing suitable samples. The fourth chapter of this thesis outlines the requirements for XNCD experiments and the efforts made to prepare appropriate samples.

The goal of the second part was to use NEXAFS spectroscopy as an analytical technique for the elemental and chemical characterization of innovative materials based on organoiron compounds. The interpretation of transition metal compounds by NEXAFS spectroscopy is difficult due to complex interactions between the metal and its surroundings. Two approaches are commonly used; an atomic multiplet model and a covalent bonding model, which lead to conflicting spectral assignments. Earlier NEXAFS studies of metallocene complexes were found to be lacking as these two models were not adequately rationalized. Owing in part to greatly improved instrumental sensitivity and to efficient theoretical calculations, the interpretation of NEXAFS spectra for a series of metallocene and metal arene complexes was refined. Enhanced understanding of the spectroscopy of these compounds eventually contributed to the characterization of a series of organometallic polymeric materials.

Underlining these studies is the remarkable complementarity of NEXAFS spectroscopy and chemistry. A comprehensive understanding of the chemistry of the samples examined in the measurement of XNCD is shown to be crucial for a successful advancement of this spectroscopy. In return, optimization of soft X-ray spectroscopy of metallocenes is demonstrated to remarkably benefit the understanding of the organometallic polymers.

ACKNOWLEDGMENTS

I would like to express my gratitude to my supervisor, Professor Stephen G. Urquhart, for his teaching and his guidance throughout the years. I wish to thank him for the professional and personal values he communicated to me. Learning by his side has been an enjoyable and captivating experience.

I would like to thank the members of my advisory committee: Professor A. Baranski, Professor B.H. Kraatz, Professor A. Moewes, and Professor M. Majewski for the valuable discussions.

I wish to acknowledge Professor N. Kosugi for his support in using his GSCF3 code and R. Wilks for his help in using StoBe program. I also thank Professor I. Stary, Travis Bessanger, P.O. Shipman and Professor A.S. Abd-El-Aziz for providing some of the compounds investigated for this thesis. I am also grateful to the members of the Physic Machine Shop and of the Chemistry-Electronic Shop of the University of Saskatchewan, and the beam-line scientists from the Advanced Light Source, the Synchrotron Radiation Centre and the Canadian Light Source.

I am also thankful to the great group members I have had the opportunity to work with, Dr. Juxia Fu, Ryan Cooney, Danielle Covelli, Lisa Blair, Eric Christensen, Remy Coulombe, Stephen Christensen and Dr. Brian Haines. They made the days a lot shorter and more worthwhile too.

Je souhaite remercier mes parents pour leur affection et leur compréhension. Je me suis souvent inspirée de leurs encouragements et de leurs conseils durant toutes ces années.
Finally I wish to thank my brother and his family, Idralyne, Mike, Sabine, Stephanie, Elise, Antoine, Rosette and Richard for preserving my sanity throughout graduate studies.

TABLE OF CONTENTS

LIST OF TABLES

LIST OF FIGURES

The permissions to use and reproduce all figures included in this dissertation have been granted to Edwige OTERO and are available upon request to:

Dr S.G. Urquhart

Department of Chemistry

University of Saskatchewan

Saskatoon, Saskatchewan

Canada S7N 5C9

LIST OF ABBREVIATIONS

[7]-H: Heptahelicene

AEY: Auger Electron Yield

ALS: Advanced Light Source

AO: Atomic Orbital

BE: Binding Energy

BM: Bending Magnet

Bz: benzene

CACAO: Computer Aided Composition of Atomic Orbital

CD: Circular Dichroism

CLS: Canadian Light Source

Cp: cyclopentadiene

CSRF: Canadian Synchrotron Radiation Facility

CVD: Chemical Vapour Deposition

DCM: Double Crystal Monochromator

DFT: Density Functional Theory

DSC: Differential Scanning Calorimetry

E_1: electric dipole transition moment

E_2: electric quadrupole transition moment

EHMO: Extended Hückel Molecular Orbital

EICVOM: Equivalent Ionic Core Virtual Orbital Model

EM: Electromagnetic

EPU: Elliptically Polarized Undulator

eV: electron Volt

EXAFS: Extended X-ray Absorption Fine Structure

GSCF: Gaussian Self Consistent Field

GTO: Gaussian Type Orbital

HF: Hartree-Fock

HMO: Hückel Molecular Orbital

HOMO: Highest Occupied Molecular Orbital

ID: Insertion Device

IP: Ionization Potential

IR: Infrared

ISEELS: Inner Shell Electron Energy Loss Spectroscopy

IUPAC: International Union of Pure and Applied Chemistry

IVO: Improved Virtual Orbital

LBNL: Lawrence Berkeley National Laboratory

LCAO: Linear Combination of Atomic Orbital

LCP: Left Circular Polarized

M_1: magnetic dipole transition moment

MLCT: Metal-to-Ligand Charge Transfer

MO: Molecular Orbital

NEXAFS: Near Edge X-ray Absorption Fine Structure

OD: Optical Density

ORD: Optical Rotatory Dispersion

OSA: Order Sorting Aperture

PEY: Partial Electron Yield

PMT: Photomultiplier Tube

RCP: Right Circular Polarized

SCF: Self-Consistent Field

SGM: Spherical Grating Monochromator

SM: Spectromicroscopy

SRC: Synchrotron Radiation Centre

SR-IVO: Shielding-Refined Improved Virtual Orbital

STO: Slater Type Orbital

StoBe: Stockholm-Berlin

STXM: Scanning Transmission X-ray Microscopy

TEM: Transition Electron Microscope

TEY: Total Electron Yield

TV: Term Value

UV: Ultra Violet

XAS: X-ray Absorption Spectroscopy

XLCD: X-ray Natural Linear Dichroism

XNCD: X-ray Natural Circular Dichroism

Z: atomic number

ZP: Zone Plate

CHAPTER 1 INTRODUCTION

NEXAFS spectroscopy is a unique tool for studying the elemental and chemical composition of a sample. It can also probe the electronic and geometric structure around selected atoms as well as local molecular orientation and magnetism. In order to introduce this unique tool, the theory of X-ray absorption is reviewed in §**1.1,** followed by a detailed description of NEXAFS spectroscopy in §**1.2**.

Chirality is a property of any object that is not superimposable on its mirror image. It is highly relevant in chemistry and biochemistry as proteins, nucleic acids and oligosaccharides are made of chiral molecules, specifically amino acids and sugars. One of the particularities of chiral molecules is that mirror image compounds will absorb left and right circular polarized light differently. A review of photon polarization is presented in §**1.3.1**. This spectroscopic effect, named circular dichroism (CD) has been observed for long wavelength radiation such as infrared and ultraviolet but has only recently been observed for circular polarized X-rays. The objective of the first research project presented in this thesis is to determine if NEXAFS spectroscopy, with circular polarized X-rays, is sensitive to the handedness of small chiral organic molecules. Natural X-ray absorption dichroism is not only observed with circular polarized light but also with linear polarized light; i.e. X-ray Natural Linear Dichroism (XNLD). In order to appreciate the distinction between the two phenomena involved in each absorption processes, i.e. XNCD and XNLD, the theory of XNLD is outlined in §**1.3.2** and the theory underlining XNCD along with the motivations for studying this effect are presented in §**1.3.3**.

Metal arene based materials are attracting increasing interest, with applications in polymer, molecular electronics and bioorganometallic sciences. The presence of the transition metal species in the polymer backbone or side chain was found to be very effective in optimising polymer solubility, as well as the material's electric, magnetic, optical, redox and mechanic properties.[1-3] The second project described in this thesis makes use of the remarkable sensitivity of NEXAFS spectroscopy to elemental and chemical composition to characterize metal arene functionalized polymers as well as the ultra violet (UV) induced fragmentation of the polymers' metal moieties.

By inspecting the literature, it was found that the interpretation of NEXAFS spectra of transition metal compounds relies on two competing models, the atomic multiplet theory[4] and the covalent bonding model.[5-8] To determine which model was most appropriate for the study

of metal arene polymers, the NEXAFS spectra of metallocene complexes were first investigated. The two competing models are described in §**1.4.1** along with a review on previous NEXAFS studies of metallocenes. The outcomes of this initial study were used to assign the spectra of substituted metal arene monomers for which the identity of the substituents was found to significantly affect the NEXAFS spectra. The metal arene polymers were examined and the UV-induced fragmentation process investigated. Relevant information on the electronic configuration, the structure and the effects of substitution on the properties of the metal arene monomers are reviewed in §**1.4.2**. The photolytic process of metal decoordination is also discussed in this section.

1.1 X-ray Absorption Spectroscopy

The absorption of light by a substance is the result of energy and angular momentum transfer from the electromagnetic (EM) radiation to the atoms and/or molecules present in the absorber. For X-rays the energy carried by the EM ranges from few electron volts (eV) to several tens of keV, which is enough to promote, upon absorption, an electron from a core orbital into an unoccupied valence orbital or into the continuum. The energy required for the latter process depends on the binding energy (BE) of the core electron. As BE is related to atomic number (Z), the energy required to excite an electron from a core orbital, or a core shell (K, L, M…), is characteristic of the elements present in the absorber. The probability of such processes to occur can be measured as a function of incident X-ray energy leading to spectra similar to that in **Figure 1.1**.

X-ray absorption spectra are characterized by step-like discontinuities or edges, emphasized in **Figure 1.1** by red lines and observed at energies corresponding to the BE of electrons; for Cr $2p_{3/2}$ and $2p_{1/2}$ electron BE= 574.1 eV and 583.8 eV, Mn $2p_{3/2}$ and $2p_{1/2}$ electron BE= 638.7 eV and 649.9 eV, Fe $2p_{3/2}$ and $2p_{1/2}$ electron BE= 706.8 eV and 719.9 eV and Ni $2p_{3/2}$ and $2p_{1/2}$ electron BE= 852.7 eV and 870.0eV.

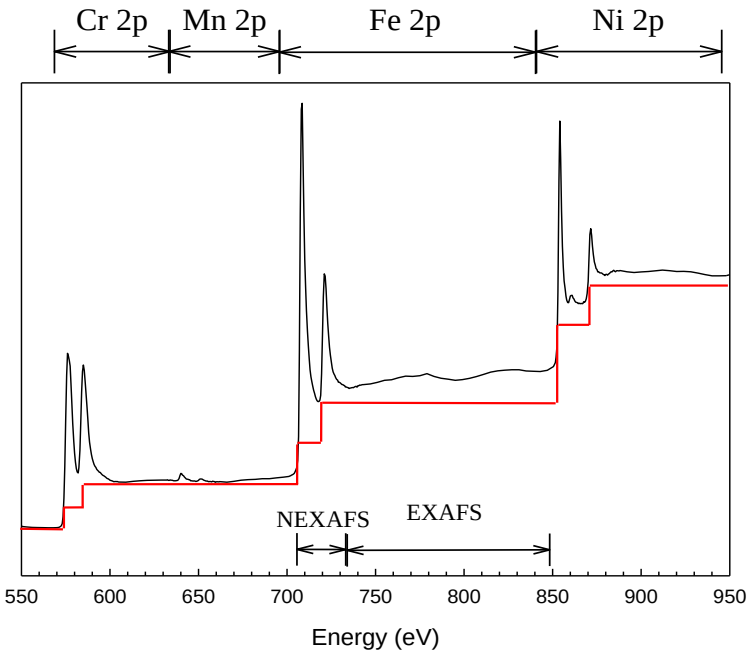

Figure 1.1 NEXAFS and EXAFS spectra of stainless steel alloy recorded at chromium 2p, manganese 2p, iron 2p and nickel 2p absorption edges. [Sample provided by Syncrude Canada Ltd., Figure courtesy of B. Haines, 2007][9]

The magnitude of the jump is related to the concentration, the density and the absorption coefficient of the absorbing element in the sample.

Near the absorption edges (±10 eV), discreet features, whose origins are related to the chemistry of the absorber, may be present. The examination of these fine structures is referred to as Near Edge X-ray Absorption Fine Structures (NEXAFS)[a] Spectroscopy. The research described in this thesis contributes to an improved understanding and application of NEXAFS spectroscopy. Further information on this technique will be presented in the following section.

At several tens of electron volts above the absorption edge, additional structures can be observed due to scattering of photoelectrons by their neighbouring atoms. Examination of these structures provides information on the distance between the ionized atom and its neighbours and is referred to as Extended X-ray Absorption Fine Structures (EXAFS) Spectroscopy[a]. As EXAFS was not used for this thesis, it will not be discussed further.

[a] Note that several acronyms have been used to refer to both techniques. For reasons of consistency with our published works we will be using NEXAFS and EXAFS throughout this entire document.

1.2 Near Edge X-Ray Absorption Fine Structure (NEXAFS) Spectroscopy

The BE of an electron is defined as the minimum energy necessary to ionize or excite an electron to the continuum. This ionization energy, or ionization potential (IP), is typically measured by XPS spectroscopy, but can also be estimated from the position of the absorption edges observed in X-ray Absorption Spectroscopy (XAS) spectra.[10] The removal of an electron from a core orbital creates a hole in the core orbital and a deshielding of the nucleus. The Coulombic attraction between the deshielded nucleus and the remaining electrons is enhanced, affecting the energy of all orbitals, including the unoccupied orbitals. Due to this core hole effect, the orbital energies shown by NEXAFS do not match the ground state energy. Transition to unoccupied orbitals may happen at energies below the IP, leading to the presence of fine structures observed below the absorption edge. These fine structures are insightful of the chemistry of the absorber, including the functional groups present, the electronic and geometric structure around the excited atom, local molecular orientation and magnetism.

X-ray absorption can be described by the *X-ray absorption cross-section* (σ_x) defined as the number of electrons excited per unit time divided by the number of incident photons per unit time per unit area. This probability of transition from the initial $|i\rangle$ to the final $|f\rangle$ state is described by Fermi's golden rule in the one-electron approximation by:[10]

$$\sigma_x \propto \left|\langle f|V(t)|i\rangle\right|^2 \rho_f(E) \qquad \textbf{Equation 1.1}$$

where ρ_f (E) is the energy density of the final states and V(t) a time-dependent perturbation describing the interaction between the electromagnetic wave, of vector potential $\boldsymbol{A}$, with an electron of charge $-e$, mass m and linear momentum operator $\boldsymbol{p}$:

$$V(\mathrm{t}) = \frac{e}{mc}\boldsymbol{A} \cdot \boldsymbol{p} \qquad \textbf{Equation 1.2}$$

The vector potential can be written for a photon of wave vector $\mathbf{k}$ ($|\mathbf{k}| = 2\pi/\lambda$) and polarization electric field vector $\boldsymbol{\varepsilon}$ interacting with an electron at position r as:

$$\boldsymbol{A} = \boldsymbol{\varepsilon}\, e^{i\mathbf{k}\cdot \mathrm{r}} \qquad \textbf{Equation 1.3}$$

which can be expanded in a truncated Taylor series into:

$$\boldsymbol{A} = \boldsymbol{\varepsilon}\,(1 + i\mathbf{k} \cdot \mathrm{r}) \qquad \textbf{Equation 1.4}$$

provided that $\mathbf{k} \cdot \mathrm{r} << 1$. By integrating equations (1.4), (1.3) and (1.2) into (1.1):

$$\sigma_x \propto |\langle f|\, \boldsymbol{\varepsilon} \cdot \boldsymbol{p} + i(\boldsymbol{\varepsilon} \cdot \boldsymbol{p})(\mathbf{k} \cdot \mathrm{r})\, |i\rangle|^2 \rho_f(\mathrm{E}) \qquad \textbf{Equation 1.5}$$

The first part of the expansion $|\langle f|\boldsymbol{\varepsilon}\cdot\boldsymbol{p}\,|i\rangle|^2$ relates to the interaction between the electric field vector ($\boldsymbol{\varepsilon}$) of the electromagnetic radiation with the transition electric dipole moment (E_1 term). This electric dipole interaction is responsible for most of the photoelectronic effects at wavelengths greater than 10^{-10} m, and in the dipole approximation only this term is considered.

The second part $|\langle f|\,i(\boldsymbol{\varepsilon}\cdot\boldsymbol{p})(\mathbf{k}\cdot r)|i\rangle|^2$ is the origin of higher order terms, such as the electric quadrupole moment (E_2) and the magnetic dipole moment (M_1). The relevance of $E_1 \cdot E_2$ and $E_1 \cdot M_1$ cross terms in X-ray absorption process will be discussed later as they are crucial to XNCD.

The final state can be a continuum state (photoionization) where the excited electron is localized in the potential of the core excited ion or a bound state (photoexcitation) where the excited electron is localized in the potential of an overall neutral atom or molecule. In the second case, the σ_x is sensitive to the functional group containing the core-excited atom and the spectral absorption fine structures are assigned to transitions from the core excited orbital to Rydberg and unoccupied molecular orbitals. The sensitivity of NEXAFS spectroscopy to functional groups is illustrated in **Figure 1.2**.

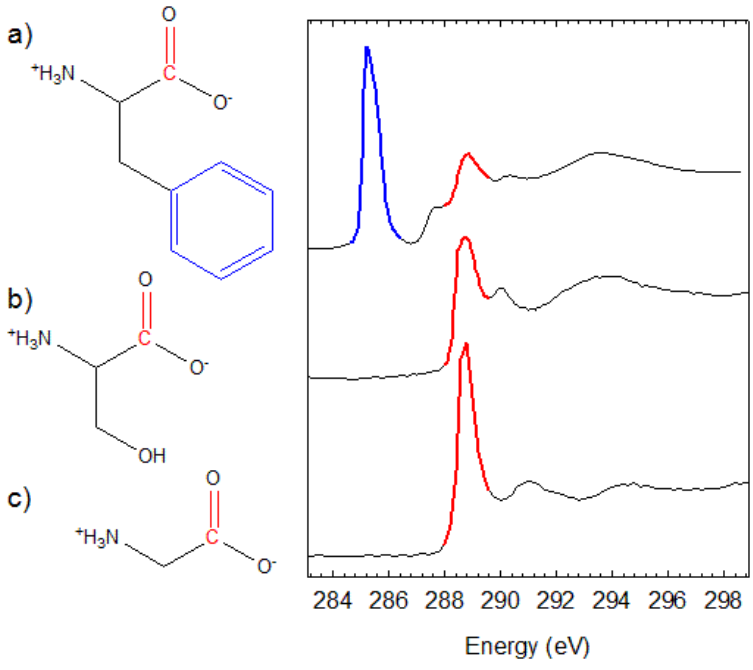

Figure 1.2 Example of the sensitivity of NEXAFS spectroscopy at C 1s edge to functional groups in amino acids; a) phenylalanine, b) serine and c) glycine in solid state.

1.3 Dichroism in X-ray Absorption Spectroscopy

The first objective of the research presented in this thesis is to investigate the sensitivity of NEXAFS spectroscopy toward the handedness of chiral organic molecules. After a brief description of light polarization, X-ray Natural Linear Dichroism (XNLD) and X-ray Natural Circular Dichroism (XNCD) in non-magnetic chiral samples will be introduced. X-ray dichroism in magnetic samples leads to X-ray Magnetic Linear Dichroism (XMLD) and X-ray Magnetic Circular Dichroism (XMCD). As the investigation of magnetic samples was outside the scope of the research objectives, XMLD and XMCD will not be described in detail.

1.3.1 X-ray polarization

In a classical approach, light is described as an electromagnetic wave composed by an electric and magnetic field (respectively E and H), which oscillate at right angles to one another and perpendicular to the propagation direction k, as described in **Figure 1.3**.

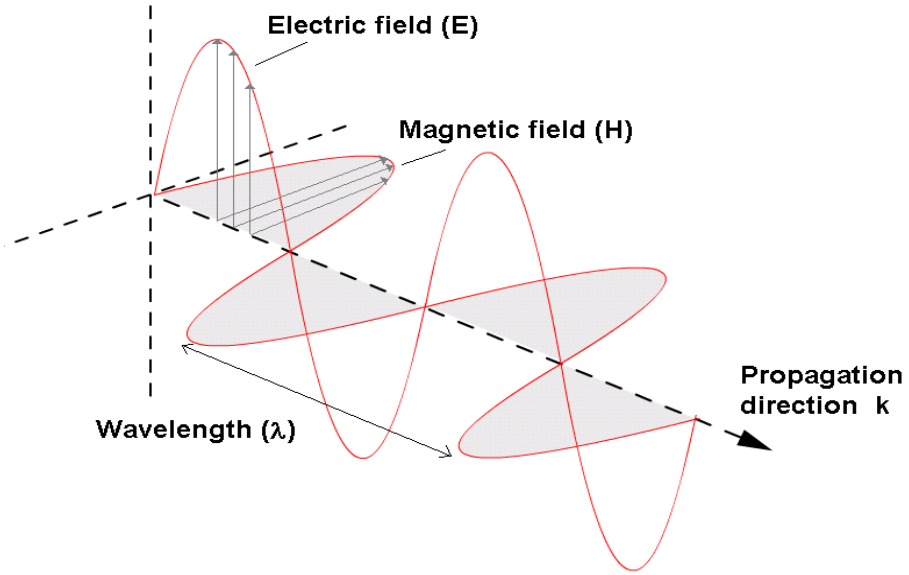

Figure 1.3 Schematic representation of electromagnetic radiation where the electric field (E) and the magnetic field (M) oscillate at right angles to one another, normal to the propagation direction k.

To simplify the explanation, we first look only at the electric field. The electric field is stressed over the magnetic field because its contribution to photon absorption phenomena is more important than the contribution of the magnetic component.

The polarization of light refers to the propagation of the electric field as described by the electric field vector. When the electric field vector oscillates in a single plane, the light is linearly polarized. When the electric field vector describes an ellipse or a helix, the light is elliptically or circularly polarized; both plane and circular polarized radiations are presented schematically in **Figure 1.4**.

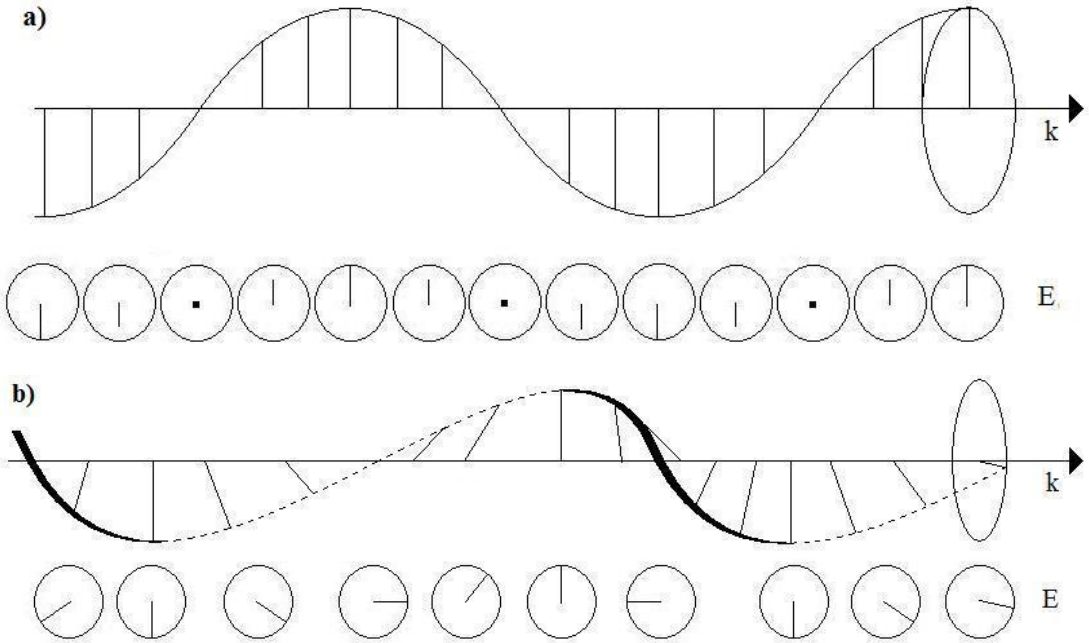

Figure 1.4 Schematic representation of a) plane polarized light and b) circular polarized light.

In a Cartesian coordinate system, the electric field E of a light wave propagating in the z direction can be dissociated into two components:

$$E_x = \boldsymbol{\varepsilon}_x E_{0x} e^{i(\psi_x)} \quad \text{and} \quad E_y = \boldsymbol{\varepsilon}_y E_{0y} e^{i(\psi_y)} \qquad \textbf{Equations 1.6-a and b}$$

where E_0 and ψ are the amplitude and the phase of the light waves, with:

$$\psi = \omega t - \mathbf{k}z + \delta \qquad \textbf{Equation 1.7}$$

where ω is the frequency, $\mathbf{k} = 2\pi/\lambda$ and $(\delta_x - \delta_y)$ = phase difference between ψ_x and ψ_y. The quantities $\boldsymbol{\varepsilon}_x$ and $\boldsymbol{\varepsilon}_y$ are the normalized unit vectors that describe the state of polarization of the electric fields, they can be written as a column vector:[11]

$$\boldsymbol{\varepsilon} = \begin{pmatrix} \cos\alpha \\ \sin\alpha \end{pmatrix} \qquad \textbf{Equation 1.8}$$

where α is the azimuth of polarization relative to the x axis. This approach is referred to as the Jones matrix calculus and offers the advantage over other classical approaches to account for the relation between amplitude and phase in the superposition of two waves.[12]

Linear polarized light can be decomposed into two linear polarized waves propagating in the z direction and oscillating respectively in the xz and yz planes, as represented in **Figure 1.5-a**, for which $(\delta_x - \delta_y) = 0$.

Circular polarized light may as well be described as the superposition of two linear polarized waves, as represented in **Figure 1.5-b**, for which $(\delta_x - \delta_y) = \pm 90°$ and where the electric polarization vectors for right and left circular polarized light may be written as:

$$\boldsymbol{\varepsilon\pm} = \frac{1}{\sqrt{2}}\begin{pmatrix} 1 \\ \pm i \end{pmatrix} \qquad \textbf{Equation 1.9}$$

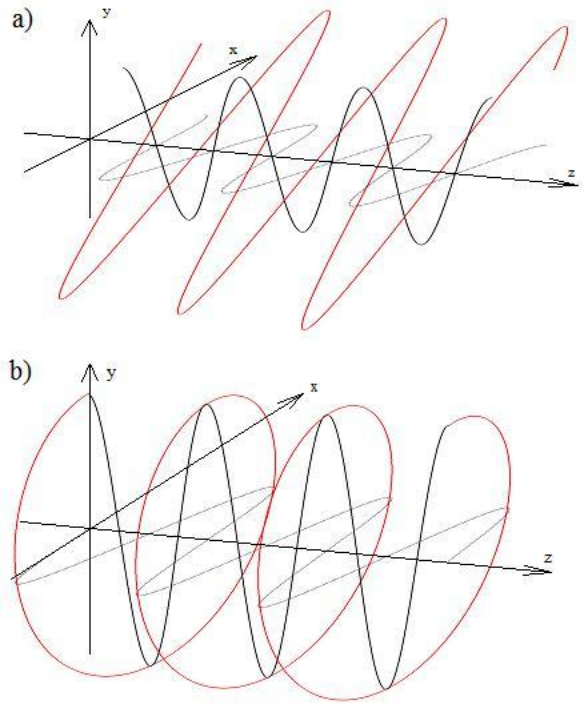

Figure 1.5 Schematic representation of a) linear polarized light (red curve) and b) circular left polarized light (red curve) as resultants of two linear polarized waves (black and grey curves) propagating in the z direction and oscillating along the x and y axis with phase sifts of 0º and 90º respectively.

By convention, when looking at the beam coming towards you, an anticlockwise rotation corresponds to left circularly polarized light (LCP), as represented in **Figure 1.5-b**, and a clockwise rotation corresponds to right polarized light (RCP).

Unpolarized light, such as the light emitted by the sun or an incandescent light bulb, is a convolution of all possible polarizations; i.e.: linear, circular and elliptical. For simplicity the theory of light interaction with matter is often based on a model where light is linearly polarized. Yet the polarization of the EM radiation leads to different absorption mechanisms.

In the next two sections the absorption of linear and circular polarized light by matter will be described with emphasis on the phenomenon that takes place at X-ray wavelengths.

These descriptions of the interaction of light with matter are done using a semiclassical approach where the radiation is treated as a classical electromagnetic wave (e.g. **Figure 1.3**) and the atoms and molecules are considered as quantum objects. An alternative description makes use of the quantum mechanical treatment of light where the radiation field is quantized as well. In a quantum mechanics approach circular polarization of light is accounted for in the sign of the photon spin angular momentum $\pm\hbar$, where $\hbar = h/2\pi$ and h is the Planck constant (6.626×10^{-34} J.s). While this quantum electrodynamics description is more complete it is much more cumbersome to treat and the semiclassical approach is often preferred as it is considered more intuitive. Also, for this reason the quantum mechanical treatment of light is not considered in this thesis.

1.3.2 X-ray Natural Linear Dichroism (XNLD)

X-ray Natural Linear Dichroism is a difference in absorption of linear polarized light (vertical versus horizontal) due to an anisotropic charge distribution in the sample.[13] In the dipole approximation, high order terms such as E_2 and M_1 are ignored and σ_x depends only on: modified from[10]

$$\sigma_x \propto |\langle f|\, \boldsymbol{\varepsilon} \cdot \boldsymbol{p}\, |i\rangle|^2 \propto \cos^2\delta \qquad \textbf{Equation 1.10}$$

where δ is the angle between electric field vector $\boldsymbol{\varepsilon}$ and the electric transition dipole moment (μ_{if}), defined by:

$$\mu_{if} = \langle f|\, \mathbf{p}\, |i\rangle \qquad \textbf{Equation 1.11}$$

The momentum operator $\mathbf{p}$ corresponds here to the electric dipole moment operator $\boldsymbol{\mu}$ that is defined, for N particles of charge q_i and position vector r_i by:[14]

$$\mathbf{p} = \boldsymbol{\mu} = \sum_{i=1}^{N} q_i r_i \qquad \textbf{Equation 1.12}$$

In the context of XAS this means that the intensity of spectral features associated with XNLD will be greater for transitions where the electric field vector $\boldsymbol{\varepsilon}$ points in the same direction as the electric transition dipole moment μ_{if}.

XNLD is illustrated in **Figure 1.6** for carbon monoxide molecules absorbed on Pt(111) with the molecular axis perpendicular to the substrate surface. In the case of a transition from a 1s orbital, the transition dipole moment coincides with the maximum

density of the unoccupied molecular orbital. The maximum density of the π* orbital in CO is oriented perpendicular to the molecule axis (**1.6-a**) while the σ* orbital is aligned along the molecule axis (**1.6-b**). An intense feature associated with the C 1s→$\pi^*_{(C=O)}$ transition is observed when **ε** (or E in **Figure 1.6**) is collinear with the π* maximum density, corresponding to the X-ray propagation direction normal to the Mo substrate surface. As the incident angle between the X-rays and substrate is changed, the intensity of the peak associated with the C 1s→$\pi^*_{(C=O)}$ transition decreases while the peak corresponding to the C 1s→$\sigma^*_{(C=O)}$ transition increases.

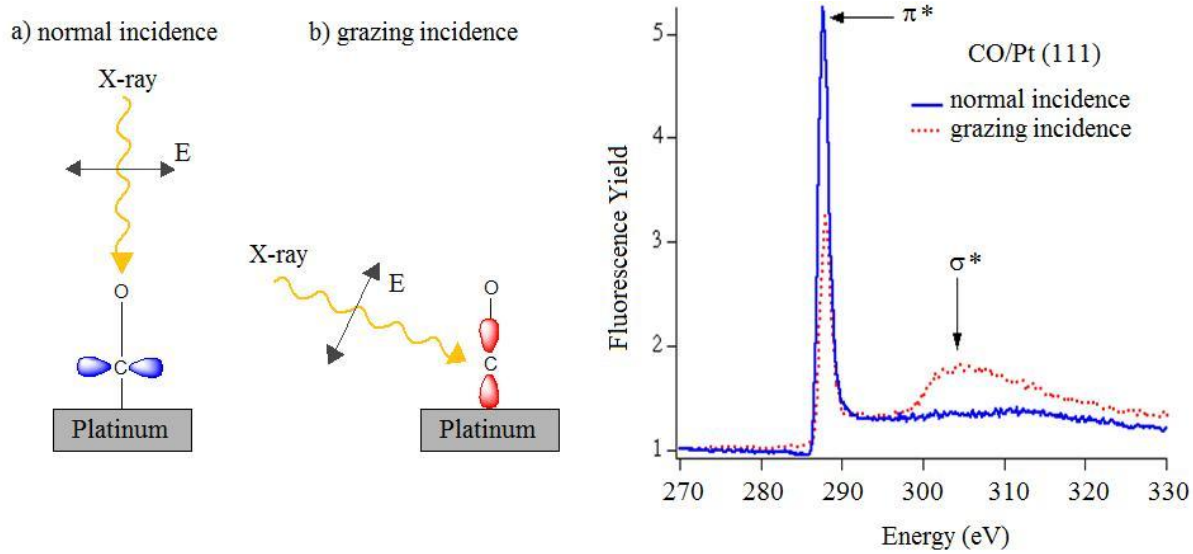

Figure 1.6 X-ray absorption linear polarization dependence of carbon monoxide (CO) molecules adsorbed on Platinum. a-blue spectrum: illustration of π* orbital and C 1s NEXAFS spectrum of CO recorded with normal incident X-ray beam; b-red spectrum: illustration of σ* orbital and C 1s NEXAFS spectrum of CO recorded at grazing X-ray incidence angle. [Data courtesy of B. Haines]

XNLD has been used successfully to determine the orientation of molecules in highly ordered assemblies such as glycine monolayers on copper.[15,16] Three models were proposed for the binding of glycine: bridging, unidentate and flat-lying (see **Figure 1.7-a**). Glycine monolayer NEXAFS spectra recorded at C 1s, N 1s and O 1s edges for different sample orientations with respect to the electric field vector of the incident radiation showed polarization dependences (see **Figure 1.7-b**). With the help of Density Functional Theory calculations (DFT), the authors were able to determine that the variations in intensity observed for resonances assigned to π* and σ* transitions were distinctive of the flat lying binding model.

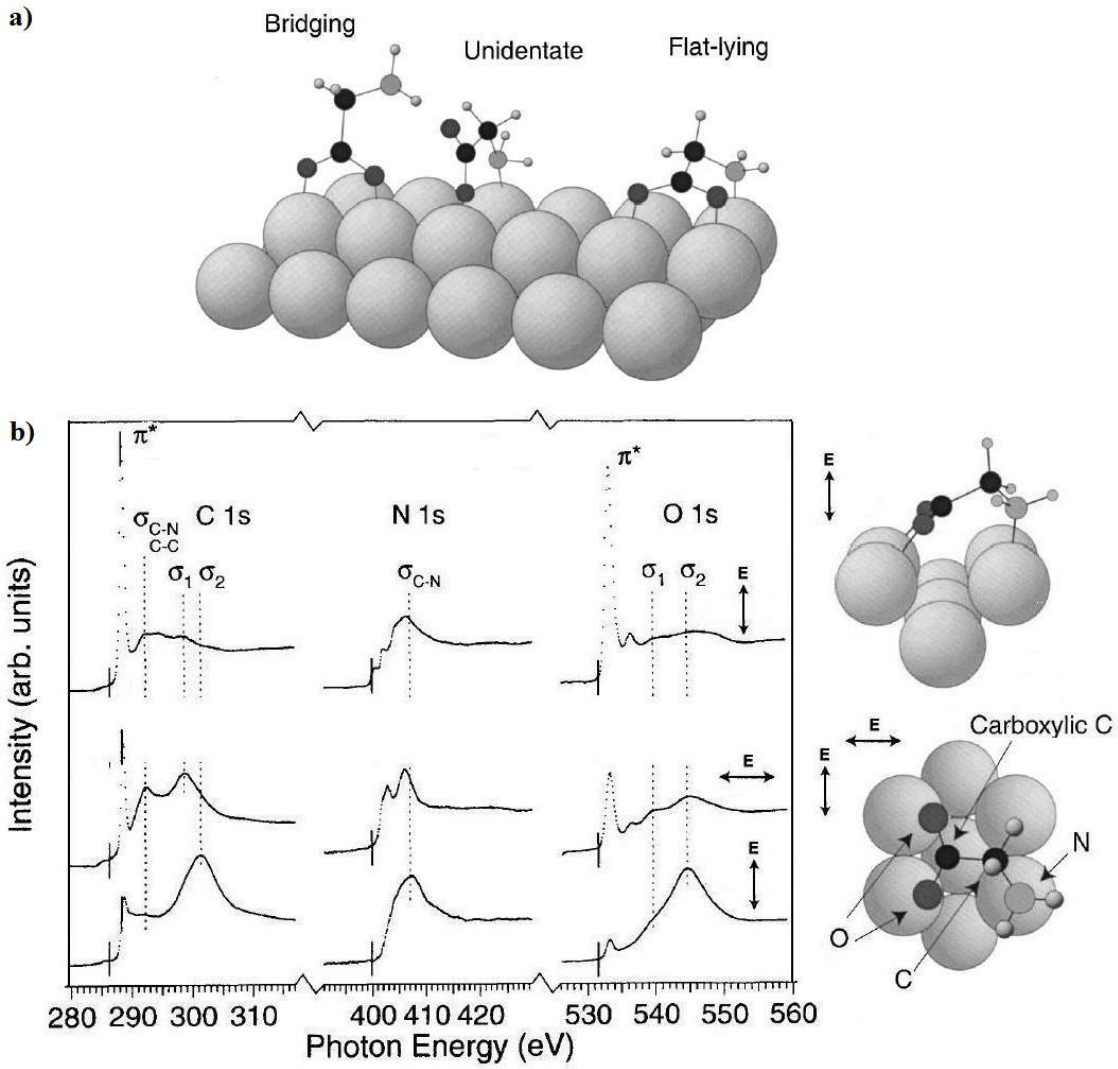

Figure 1.7 a) Schematic representation of three possible binding model of glycine on copper.[16] [Reprinted with permission from Journal of Chemical Physics, 112, M. Nyberg, J. Hasselström, O. Karis, N. Wassdahl, M. Weinelt, A. Nilsson and L.G.M. Pettersson, The electronic structure and surface chemistry of glycine adsorbed on Cu(110),5420-5427, Copyright 2000, American Institute of Physics.] b) C 1s, N 1s and O 1s, NEXAFS spectra of glycine adsorbed on copper and schematic representation of flat-lying binding model of glycine on copper.[15] [Reprinted with permission from Surface Science, 407, J. Hasseltröm, O. Karis, M. Weinelt, N. Wassdahl, A. Nilsson, M. Nyberg, L.G.M. Pettersson, M.G. Samant and J. Stöhr, The adsorption structure of glycine adsorbed on Cu(110); comparison with formate and acetate/Cu(110), 221-236, Copyright 1998, with permission from Elsevier.]

1.3.3 X-ray Natural Circular Dichroism (XNCD)

X-ray Natural Circular Dichroism is a difference in absorption of circular polarized light (left versus right) due to anisotropic charge distribution in chiral samples. Chirality is defined as the property of objects to not superimpose on their mirror images and will be described in greater detail in **Chapter 4**.

In the expression of the absorption cross section:

$$\sigma_x \propto |\langle f|\boldsymbol{\varepsilon}\cdot\boldsymbol{p} + i(\boldsymbol{\varepsilon}\cdot\boldsymbol{p})(\mathbf{k}\cdot r)|i\rangle|^2 \rho_f(E) \qquad \textbf{Equation 1.5}$$

as mentioned in **§1.2**, the presence of the second part, i.e. $|\langle f|i(\boldsymbol{\varepsilon}\cdot\boldsymbol{p})(\mathbf{k}\cdot r)|i\rangle|^2$, is associated with higher order terms, i.e. electric quadrupole moment (E_2) and the magnetic dipole moment (M_1). These higher order terms are associated with interference terms which mix the transition electric dipole – electric quadrupole moments ($E_1 \cdot E_2$ cross term) and electric dipole – magnetic dipole moments ($E_1 \cdot M_1$ cross term).[17] It is these higher order cross terms that are responsible for the anisotropic absorption of LCP and RCP light in non magnetic material.

The transition electric quadrupole moment (E_2) resembles two electric dipole moments back-to-back and is related to space handedness around the absorbing atom.[17] As the space handedness of a chiral object is opposite to that of its mirror image, the transition electric quadrupole moments of two enantiomers (i.e.: two non superimposable mirror images) are expected to be non superimposable mirror images as well.

Left and right circular polarized light have opposite space handedness and their interaction with a chiral molecules is expected to lead to $(E_1 \cdot E_2)^L$ and $(E_1 \cdot E_2)^R$ cross terms of opposite sign.

The contribution of the $E_1 \cdot E_2$ cross term to circular dichroism was demonstrated by Barron to only exist in specific oriented systems and to vanish in randomly oriented systems.[18] Optical activity at UV-wavelengths in non-oriented systems therefore arises from the other higher order term, $E_1 \cdot M_1$.[18,19]

Magnetic dipole moments (M_1) arise during transitions involving circular charge redistribution. As for $E_1 \cdot E_2$, space handedness around the absorbing atom causes M_1 in two enantiomers to be non superimposable mirror images. Also $E_1 \cdot M_1$ cross terms associated with the absorption of left or right circular polarized light are expected to have opposite signs. Unlike the $E_1 \cdot E_2$ effect, $E_1 \cdot M_1$ effect is present for both oriented and non-oriented systems.

The dissymmetry g-factor[b] is defined as:

$$g = 2 \times \frac{\sigma_{LCP} - \sigma_{RCP}}{\sigma_{LCP} + \sigma_{RCP}} \qquad \textbf{Equation 1.13}$$

where σ_{LCP} and σ_{RCP} are the absorption cross sections recorded with LCP and RCP light respectively. XNCD effects can then be displayed in a graphical manner by plotting g-factor values as a function of energy. In absence of circular dichroism the g-factor is equal to zero over all energies. In presence of circular dichroism, XNCD spectra are characterized by positive and negative deviations observed at energies where either $(E_1 \cdot E_2)^L > (E_1 \cdot E_2)^R$ or $(E_1 \cdot E_2)^L < (E_1 \cdot E_2)^R$ and where either $(E_1 \cdot M_1)^L > (E_1 \cdot M_1)^R$ or $(E_1 \cdot M_1)^L < (E_1 \cdot M_1)^R$. XNCD spectra recorded from two enantiomers are expected to be symmetric around the energy axis.

At optical wavelength, $E_1 \cdot M_1$ cross terms are much larger than $E_1 \cdot E_2$ cross terms and dominate the UV-CD spectra. At X-ray wavelengths, the contribution of M_1 and E_2 multipoles to the photoelectronic effect is quite small and only a few recent studies have been successful in recording XNCD spectra.

The first XNCD measurements performed in the late 90s were successful for only a few crystals: α-$LiIO_3$ at iodine L_1, L_2 and L_3 edges, $Na_3[Nd(digly)_3] \cdot 2NaBF_4 \cdot 6H_2O$ (digly = dianion of diglycolic acid) at Nd L_3 edge and $2[Co(en)_3Cl_3]NaCl \cdot 6H_2O$ (en = ethane-1,2-diamine) at Co K edge.[17,20-22] For all crystals XNCD effect was due to $E_1 \cdot E_2$ interferences and the authors supported their assignments by calculating XNCD spectra for which they obtained remarkably good agreement with experimental results. **Figure 1.8** presents experimental NEXAFS spectrum of $Na_3[Nd(digly)_3] \cdot 2NaBF_4 \cdot 6H_2O$ recorded at Nd L_3 edge, along with the XNCD spectra measured from the two enantiomorphic single crystals.[17,21] As expected the very weak XNCD spectra recorded from two enantiomers are mirror images around the energy axis. The authors showed that the CD was associated with the chiral pathway of the multiple scattered photoelectron.[17] Specifically, multiple scattering calculations showed that XNCD effects only arose for four (or higher) scattering paths; backscattering (two paths) and three paths (triangle) created achiral scattering geometries. This shows that the XNCD is associated with chiral core excited states; an effect we wish to explore at soft x-ray wavelengths.

---

[b] In literature the dissymmetry g-factor is also referred to as Kuhn asymmetry factor or the anisotropy ratio.

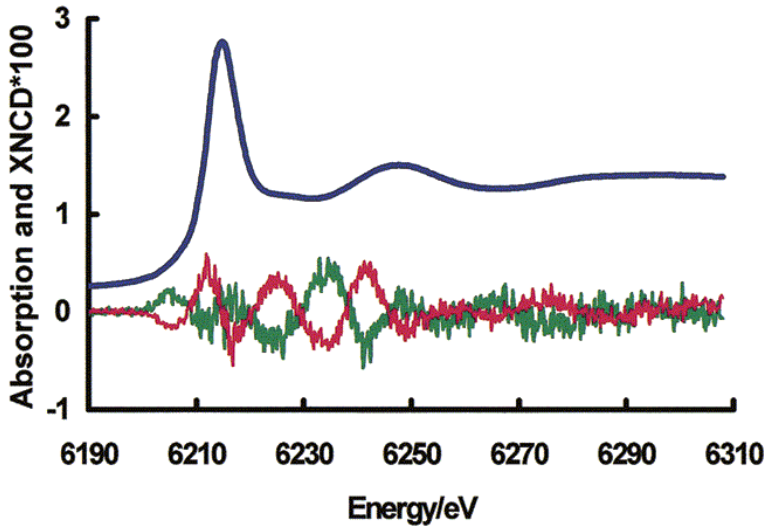

Figure 1.8 Experimental Nd L_3 edge of enantiomorphic crystals of $Na_3[Nd(digly)_3]\cdot 2NaBF_4\cdot 6H_2O$ (digly = dianion of diglycolic acid) (blue) and $XNCD_{E1E2}$ signal x100 (green and red).[17] [Reprinted with permission from Journal of Physical Chemistry B, 105, R.D. Peacock and B. Stewart, Natural Circular Dichroism in X-ray Spectroscopy, 351-360, Copyright 2001, American Chemical Society.]

The measurement of XNCD spectra from a powder sample of $2[Co(en)_3Cl_3]NaCl\cdot 6H_2O$ at Co K edge led to an almost featureless curve.[23] As mentioned previously $E_1\cdot E_2$ cross term cancels out in randomly oriented samples, therefore the authors suggested that the extremely weak structures observed in the XNCD spectra of $2[Co(en)_3Cl_3]NaCl\cdot 6H_2O$ may originate from the weak $E_1\cdot M_1$ interferences.

The measurement of XNCD associated with $E_1\cdot M_1$ cross term only is in fact very challenging. Theoretical studies have predicted for organic compounds, i.e. containing low atomic number elements, and at K absorption edge a magnitude of g-factor on the order of 10^{-8} to 10^{-3}.[17]

In **Chapter 4** efforts made to select appropriate organic molecules and optimize the sample preparation in attempt to observe $XNCD_{E1M1}$ effect from organic molecules will be described.

1.4 NEXAFS spectroscopy of metallocene and metal arene monomers and polymers

Ferrocene-based materials have found a wide application in molecular electronics and bioorganometallic materials.[24-29] With the development of new synthetic routes, ferrocene-based polymers and macromolecules are being increasingly examined. Recent studies show

that the presence of ferrocene moieties in polymers' backbone or side chains can improve the processability of the polymer as well as its electric, magnetic, optical, redox and mechanic properties.[30-33] Such ferrocene based materials could have potential applications as photonic devices, variable refractive-index materials, magnetic and semiconducting nanomaterials, composite materials, ceramic and coating agents, to name a few.[1-3]

NEXAFS spectroscopy is often used to investigate the bonding in transition metal compounds. The spectral assignment is subject to two competing models, atomic multiplet theory[4] and covalent bonding model.[6-8]

We are interested in the use of NEXAFS spectroscopy to characterize the electronic structure of metal arene compounds and functionalized polymers and the UV-induced fragmentation of the polymers' metal moieties[34-36]. For these studies, it is essential to understand the sensitivity of NEXAFS spectroscopy to bonding (via covalent bonding and electronic delocalization effects) as well as atomic electronic structure (via atomic multiplet effects) in metallocenes and metal arene complexes.

The relevance of the atomic multiplet and covalent bonding models to the assignment of organometallic NEXAFS spectra will be discussed in the next section. Information on metal arene complexes and functionalized polymers will be presented in the following section.

1.4.1 XAS of Organometallics

The atomic multiplet theory is based on the electronic structure of the metal atom, as perturbed by angular momentum interactions and the crystal field environment of the metal atom. In an isolated atom, multiplet splitting arises from the lifting of atomic orbital (AO) degeneracies (e.g. d^4, d^6, etc) into states due to electron correlation and exchange interaction effects associated with electron spin and orbital angular momentum. For example, a 3d atom with a d^2 configuration will have ^1S, ^1D, ^1G, ^3P and ^3F states. When in an ionic compound, this atomic electron configuration is further perturbed by inter-atomic Coulombic interactions, described by crystal field theory. Core excitation in NEXAFS spectroscopy (e.g; 2p $\rightarrow$ 3d transitions) creates additional complications, as the unpaired electrons in the core hole orbital and the optical orbital will lead to new spin-spin and spin-orbit interactions.[37] This model has been used to assign the NEXAFS spectra of metal cations in a wide range of crystal field splitting environments with the help of atomic multiplet calculations.[4]

On the other hand the importance of conjugation between metal 3d orbitals and ligand π* orbitals in the interpretation of NEXAFS spectroscopy of transition metal complexes has been indicated in several studies.[38-45] In the investigation of planar Ni $3d^8$ and Cu $3d^{9,10}$ low spin complexes, the presence of an intense band at the L_2 and L_3 edges was assigned to metal-to-metal transitions (2p → 3d), followed by satellite peaks at a few electron-volts higher energy.[38-41] These satellite features were assigned as a transition to a molecular orbital showing strong metal-covalent character, and identified as a metal-to-ligand charge transfer or MLCT transition (2p → $3d_{metal}/\pi^*_{ligand}$). These assignments were supported by Hartree-Fock-based static exchange approximation and DFT calculations.[39] In the study of $K_2Ni(CN)_4 \cdot H_2O$, Ni(dimethylglyoximato)$_2$ and $[(n\text{-}C_4H_9)_4N]_2$ [Ni(maleonitriledithiolato)$_2$] complexes, the authors were able to relate the variation in intensity of the MLCT transition observed for $K_2Ni(CN)_4 \cdot H_2O$ > Ni(dimethylglyoximato)$_2$ > $[(n\text{-}C_4H_9)_4N]_2$ [Ni(maleonitriledithiolato)$_2$] to the decrease in the back-donation strength amongst these three complexes.[40,41]

In the studies performed by Hitchcock *et al.* on manganese, iron and cobalt complexes using carbonyl and cyclopentadienyl as ligands, the authors assigned the Inner Shell Electron Energy Loss Spectroscopy (ISEELS) spectra with molecular orbital arguments.[6-8]

Chapter 6 presents our investigation on ferrocene (Fe^{II}, $3d^6$) and ferrocenium (Fe^{III}, $3d^5$) and confirms that the covalent bonding model is quite efficient for assignment of the closed shell ferrocene spectra. Our findings are supported by Extended Hückel Molecular Orbital (EHMO) and Density Functional Theory (DFT) calculations. On the other hand several transitions were observed in the C 1s and Fe 2p spectra of ferrocenium which were not predicated by either computational studies (i.e. EHMO and DFT), suggesting greater contribution from the atomic multiplet model in the NEXAFS spectra of the open shell compound.

Wen *et al.* recorded the ISEELS spectra of alkane or alkene substitued ferrocene complexes (e.g.: CpFeCp-R with Cp= cyclopentadiene and R = C_4H_9, C_2H_3) and found that they were similar to that of ferrocene. They concluded that the Fe 2p edge had limited sensitivity to chemical substitution at remote locations on the cyclopentadiene ligand.[8] In their investigation of ferrocene-labelled peptides and carboxylic acid substituted ferrocene complexes, Wilks *et al.* also found that Fe 2p spectra were unaffected by the substituent type.[46]

In contrast, investigation of substituted ferrocene (closed shell) compounds presented in **Chapter 7** shows that electron donating / withdrawing properties of the ligands and substituents, as well as π*-conjugation between the cyclopentadienyl ligand and substituent, significantly affect the energy and intensity of Fe 2p NEXAFS transitions.

These findings were used to help interpret the NEXAFS spectra of metal arene complexes and functionalized polymers reported in **Chapter 8** and **9**.

1.4.2 Metal Arenes and Polymers

(η^6-benzene)(η^5-cyclopentadienyl)iron(II), or (Bz)(Cp)Fe, was first synthesized in 1957 by Coffield *et al.* from reaction of $CpFe(CO)_2Cl$ with arene compounds in the presence of aluminum chloride ($AlCl_3$). Several years after Nesmeyanov *et al.* proposed a different route which has been since applied extensively to the synthesis of substituted metal arenes, fused arenes like pyrene as well as very large fused arene assemblies such as graphite sheets or carbon fibers.[47-49] The general mechanism of the ligand exchange reaction involves the formation of a complex between $AlCl_3$ and Cp ring that weaken the metal Cp bonds, followed by a nucleophilic attack by the arene, forming CpFeArene cation.[50] Aluminum powder is added to reduce ferrocenium formed into ferrocene. Numerous alternative routes have been proposed since, expending considerably the diversity of arene ligands, including polymers and dendrimers containing aromatic groups.[51,52]

The structure of a series of substituted metal arene complexes have been examined by X-ray crystallography. The distance between the iron and the center of gravity of a benzene ring was found in the range 1.52 Å – 1.60 Å and between iron and the center of gravity of a Cp ring in the range 1.62 Å – 1.79 Å.[53] The two rings were found to be nearly coplanar with a dihedral angle between benzene and Cp ring below 3°.[53]

The electronic structure of $(Cp)Fe^{II}(Bz)$ was found to be similar to that of ferrocene with the following molecular orbital sequence: occupied metal orbital Fe $3d_{x^2-y^2}$ and Fe $3d_{xy}$ (degenerate) mixed with unoccupied ligand $\pi^*_{(Cp)}$ and $\pi^*_{(Bz)}$ MOs < occupied Fe $3d_{z^2}$ << unoccupied Fe $3d_{xz}$ and Fe $3d_{yz}$ (degenerate) mixed with occupied $\pi_{(Cp)}$ and $\pi_{(Bz)}$; note that the highest occupied molecular orbital (HOMO) is mostly localised onto the metal (see **Figure 1.9**).[54,55].

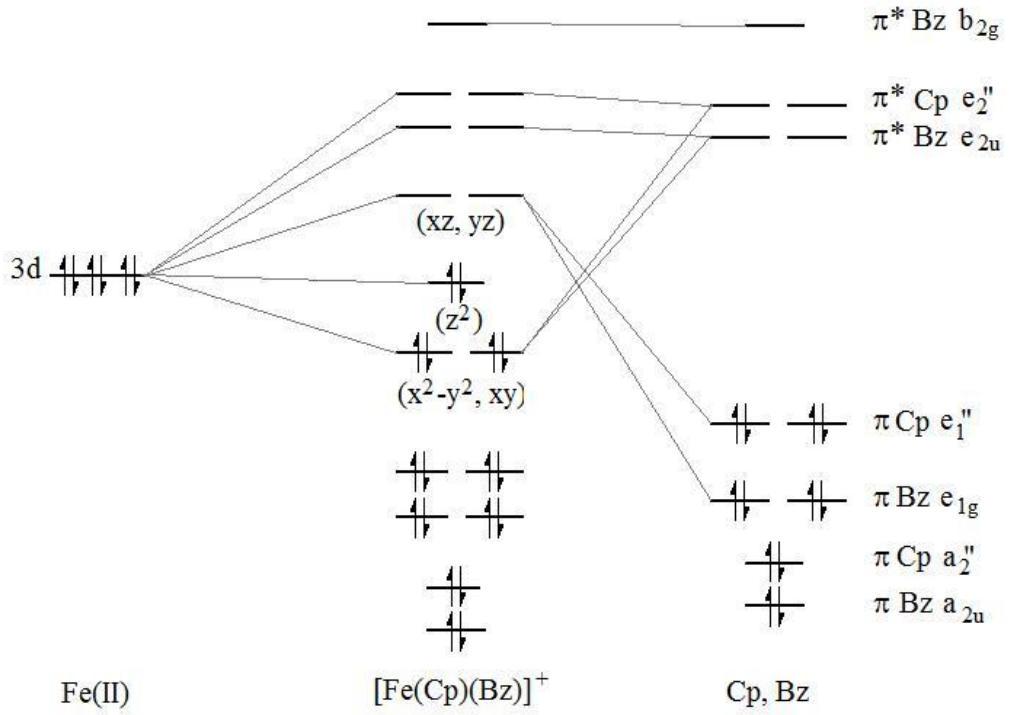

Figure 1.9 Qualitative molecular orbital diagram of $[(Cp)Fe(Bz)]^{+}$.

Electrochemical studies, including polarography and cyclic voltammetry, on $(Cp)Fe^{II}$(monosubstituted-Bz) indicated that electron donating/withdrawing properties of substituents significantly affect the half-wave potential ($E_{1/2}$) values.[50,56,57] These studies suggest that electron donating/withdrawing properties of the substituents are transmitted through the benzene ring to the iron center affecting the electron density around the metal.

A series of $(Cp)Fe^{II}$(substituted-benzene) and (substituted-Cp)Fe^{II}(Bz) complexes have been examined using ^{57}Fe Mössbauer spectroscopy, ^{13}C and ^{57}Fe nuclear magnetic resonance (NMR) spectroscopy. These studies indicated that substituent inductive components also affects the electron distribution in the ligand opposite to the substituted ring.[58,59]

An X-ray photoelectron spectroscopy study performed by P.G. Gassman *et al.* on 20 $(Cp)Fe^{II}$(substituted-benzene) complexes showed variations in binding energies consistent with the electrochemical studies mentioned above.[60] In addition the decrease in Fe $2p_{3/2}$ BE for $[(Cp)Fe^{II}$(methylbenzene)$][PF_6]$ and $[(Cp)Fe^{II}$(di-, tri-, tetra-, penta-, hexa-methylbenzene)$][PF_6]$ complexes was found to follow the increase in electron donor methyl groups.[60]

C**hapter 8** presents a series of [(Cp)Fe^{II}(monosubstituted-benzene)][PF_6] complexes examined by NEXAFS spectroscopy at Fe 2p and C 1s edges. The inductive effect of the substituents was found to have a minor but significant effect on the transition energies and intensities. As seen for substituted ferrocene compounds (**Chapter 6**) the presence of π*-conjugation between the benzene ring and the substituent leads to additional spectral features at Fe 2p.

Amongst the many substituted metal arene complexes available one was found very useful in the preparation of polymeric materials. The reaction of (Cp)Fe(1,n-dichlorobenzene) where n=2, 3 or 4, with various oxygen and sulphur dinucleophies led to the synthesis of soluble cyclopentadienyliron functionalized polymers containing aromatic ether, thioether and amine bridges with relatively high molecular weight.[35,61-63] The iron moiety is then removed by pyrolysis, electrolysis or photolysis leading to the corresponding organic polymers; **Figure 1.10** presents the details of the synthesis of polyphenylene sulphides used by Abd-El-Aziz *et al*.[35] The preparation of organic materials such as polyphenylene sulphide, a thermoplastic widely used in the polymer industry, requires traditionally extreme conditions, suffers from relatively poor yield and the low solubility of the polymer limits the length of the polymer chains achieved. On the other hand, the photolytic demetallation of cyclopentadienyliron functionalized polymers, at room temperature, was found very efficient in preparing polyethers and polythioethers with high molecular weight and yields greater than 70%.[35]

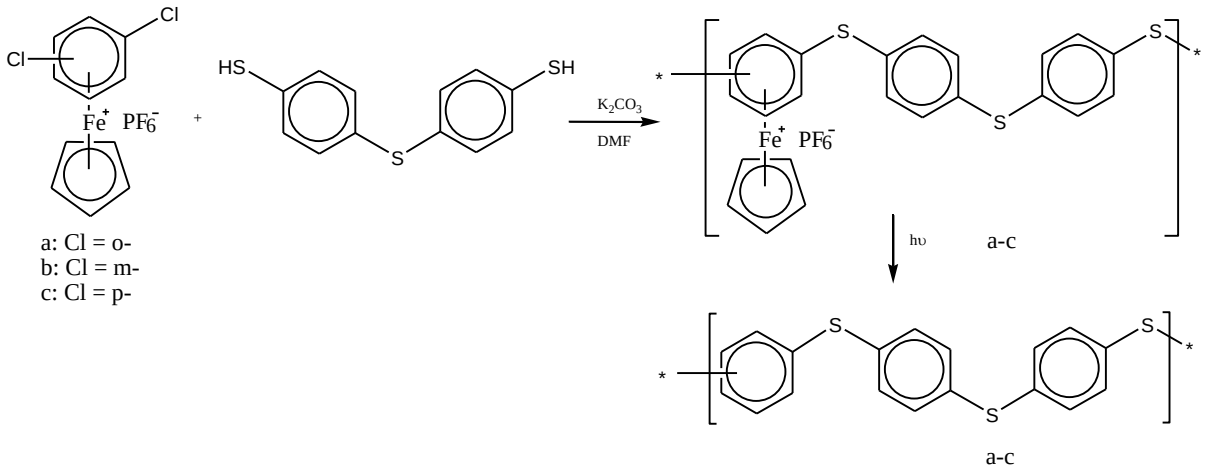

Figure 1.10 Details of the synthesis of polyphenylene sulfides proposed by Abd-El-Aziz *et al.*[35]

The photolysis of $[(Cp)Fe(Bz)^+][X^-]$ (where X^- = counterion) and substituted derivatives has been extensively investigated due to the use of the cation as polymerization photoinitiator.[64] The mechanism and the intermediates and products formed during the photo-dearylation of $[(Cp)Fe(Bz)^+][X^-]$ (with $X^- = PF_6^-, BF_4^-, AsF_6^-, SbF_6^-, BPh_4^-$) in solution have been examined using nuclear magnetic resonance,[65,66] infrared spectroscopy,[65-67] UV -visible spectroscopy,[65,68-72] fluorescence spectroscopy,[67,73] conductivity measurements,[69,70] electrochemistry,[74] time resolved laser spectroscopy,[75] high pressure liquid chromatography and gas chromatography – mass spectroscopy[67] and electron spray ionization mass spectroscopy.[76,77] The reaction was found to be affected by the nature of the substituents on either ligand (benzene or cyclopentadiene rings), the polarity of the solvent, the identity of the counterion, the excitation wavelength and the temperature. From these studies a general mechanism was suggested: excitation of either $[(Cp)Fe(Bz)^+][X^-]$ or the freely solvated cation $(Cp)Fe(Bz)^+$ causes arene ring slippage from η^6-Bz to η^4-Bz followed by replacement of the arene by three ligands (L) to form $[(Cp)Fe(L)_3^+][X^-]$.[78] The unstable trisubstituted intermediate eventually decomposes into ferrocene, metal iron and other species containing iron, counter ion and solvent molecules.

Chapter 9 presents the characterization of polythioethers and polyethers with and without pendant iron moieties. Metallated polyether and metallated and demetallated polythioether were synthesized by members of the research group of Dr. Abd-El-Aziz according to published procedures.[35] The formation of ferrocene and iron metal was observed following the removal of iron moieties from metallated polythioether and were isolated from the organic polymer. Conversely, the presence of unidentified impurities containing iron in trace amounts was suspected within the organic polymer. With the help of NEXAFS spectroscopy these impurities have been identified as high spin $3d^5$ iron species, likely iron oxides and counter ion PF_6^-. Investigation of the photolysis process in solid phase in air indicated the formation of the same iron species as during photolysis in solution. However solid state photolysis in vacuum led to the formation of different iron species, likely to contain Fe(II) species.

NEXAFS study of metallated polyether indicated the presence of spectral features characteristics of π^*-conjugation, similar to that observed on Fe 2p NEXAFS spectra of monomer $[(Cp)Fe(substituted\text{-}Bz)][PF_6]$ examined in **Chapter 8**. The relevance of these results in the scope of potential application of these doped organic materials is discussed in **Chapter 9**.

1.5 Summary

NEXAFS spectroscopy is a very efficient technique for the characterization of organic and inorganic material.

Recent investigations of chiral inorganic compounds indicated the sensitivity of NEXAFS spectroscopy for molecule handedness. Few studies have confirmed the presence of CD in the NEXAFS spectrum of organic compounds. The objective of the work described in **Chapter 4** was to measure XNCD effect for a series of small chiral organic molecules. Several compounds, including amino acids, have been identified as model compounds for this measurement according to experimental and theoretical requirements and restrictions. Both sample preparation and data acquisition method have been greatly optimized so the measurement of the XNCD effect could be performed. The outcomes of these measurements are then discussed.

In **Chapter 5** a combined experimental and theoretical study of an amino acid is presented. Computational methods optimized for XAS simulation were used to refine the assignment of discreet features observed on the NEXAFS spectra of amino acids.

In **Chapters 8 and 9** NEXAFS spectroscopy's high sensitivity for electronic structure was used to characterize organometallic polymeric material. This study required improvement of our understanding of NEXAFS spectroscopy of metallocene and metal arene complexes, which is presented in C**hapters 6, 7** and **8**. Finally NEXAFS sensitivity of elemental and chemical composition was used effectively for the identification of impurities contained in organic polymeric material derived from demetallation of organometallic polymer (see **Chapter 9**).

1.6 References

(1) Paquet, C.; Cyr, P. W.; Kumacheva, E.; Manners, I. *Chemical Communications* **2004**, 234.

(2) Manners, I. *Journal of Optics A: Pure and Applied Optics* **2002**, *4*, S221.

(3) Kulbaba, K.; Manners, I. *Macromolecular Rapid Communications* **2001**, *22*, 711.

(4) De Groot, F. *Coordination Chemistry Reviews* **2005**, *249*, 31.

(5) Ruhl, E.; Hitchcock, A. P. *Journal of the American Chemical Society* **1989**, *111*, 5069.

(6) Hitchcock, A. P.; Wen, A. T.; Ruhl, E. *Chemical Physics* **1990**, *147*, 51.

(7) Ruhl, E.; Wen, A. T.; Hitchcock, A. P. *Journal of Electron Spectroscopy and Related Phenomena* **1991**, *57*, 137.

(8) Wen, A. T.; Ruhl, E.; Hitchcock, A. P. *Organometallics* **1992**, *11*, 2559.

(9) Haines, B.; Lanke, U. D.; Urquhart, S. G.; Hall, B.; Chioveli, S.; Anderson, M.; Kenny, K. "X-ray Photoelectron Emission Microscopy of Grain Boundary Phases in Stainless Steel Alloys"; 90th Canadian Chemistry Conference and Exhibition, **2007**, Winnipeg, Manitoba, Canada.

(10) Stohr, J. *NEXAFS Spectroscopy*; Springer-Verlag: Berlin, **1996**.

(11) Schellman, J. A. *Chemical Reviews* **1974**, *75*, 323.

(12) Collett, E. *Polarized Light; Fundamentals and Applications*; Marcel Dekker, Inc.: New York, **1993**.

(13) Stöhr, J.; Siegmann, H. C. *Magnetism; From Fundamentals to Nanoscale Dynamics*; Springer-Verlag: Berlin, **2006**.

(14) Levine, I. N. *Quantum Chemistry*, Fourth ed.; Prentice-Hall: Englewood Cliffs, **1991**.

(15) Hasselstrom, J.; Karis, O.; Weinelt, M.; Wassdahl, N.; Nilsson, A.; Nyberg, M.; Pettersson, L. G. M.; Samant, M. G.; Stohr, J. *Surface Science* **1998**, *407*, 221.

(16) Nyberg, M.; Hasselstrom, J.; Karis, O.; Wassdahl, N.; Weinelt, M.; Nilsson, A.; Pettersson, L. G. M. *Journal of Chemical Physics* **2000**, *112*, 5420.

(17) Peacock, R. D.; Stewart, B. *Journal of Physical Chemistry B* **2001**, *105*, 351.

(18) Barron, L. D. *Molecular Phsysics* **1971**, *21*, 241.

(19) Buckingham, A. D.; Dunn, M. B. *Journal of Chemical Society (A)* **1971**, *12*, 1988.

(20) Goulon, J.; Goulon-Ginet, C.; Rogalev, A.; Gotte, V.; Malgrange, C.; Brouder, C.; Natoli, C. R. *Journal of Chemical Physics* **1998**, *108*, 6394.

(21) Alagna, L.; Prosperi, T.; Turchini, S.; Goulon, J.; Rogalev, A.; Goulon-Ginet, C.; Natoli, C. R.; Peacock, R. D.; Stewart, B. *Physical Review Letters* **1998**, *80*, 4799.

(22) Stewart, B.; Peacock, R. D.; Alagna, L.; Prosperi, T.; Turchini, S.; Goulon, J.; Rogalev, A.; Goulon-Ginet, C. *Journal of the American Chemical Society* **1999**, *121*, 10233.

(23) Goulon, J.; Rogalev, A.; Wilhelm, F.; Goulon-Ginet, C.; Carra, P.; Marri, I.; Brouder, C. *Journal of Experimental and Theoretical Physics* **2003**, *97*, 402.

(24) Van Staveren, D. R.; Metzler-Nolte, N. *Chemical Reviews* **2004**, *104*, 5931.

(25) Kraatz, H. B. *Journal of Inorganic and Organometallic Polymers and Materials* **2005**, *15*, 83.

(26) Chen, D.; Li, J. *Surface Science Reports* **2006**, *61*, 445.

(27) Horie, M.; Sakano, T.; Osakada, K. *Journal of Organometallic Chemistry* **2006**, *691*, 5935.

(28) Lambert, C.; Kriegisch, V.; Terfort, A.; Zeysing, B. *Journal of Electroanalytical Chemsitry* **2006**, *590*, 32.

(29) Zheng, F.; Perez-Dieste, V.; McChesney, J. L.; Luk, Y.-Y.; Abbott, N. L.; Himpsel, F. J. *Surface Science* **2005**, *587*, L191.

(30) Manners, I. *Science* **2001**, *294*, 1664.

(31) Abd-El-Aziz, A. S.; Manners, I. *Journal of Inorganic and Organometallic Polymers and Materials* **2005**, *15*, 157.

(32) Hudson, R. D. A. *Journal of Organometallic Chemistry* **2001**, *637-639*, 47.

(33) Manners, I. *Synthetic Metal-Containing Polymers*; WILEY-VCH: Weinheim, **2004**.

(34) Abd-El-Aziz, A. S.; Todd, E. K. *Coordination Chemistry Reviews* **2003**, *246*, 3.

(35) Abd-El-Aziz, A. S.; Todd, E. K.; Ma, G. Z. *Journal of polymer Science: Part A: Polymer Chemistry* **2001**, *39*, 1216.
(36) Abd-El-Aziz, A. S.; Todd, E. K.; Okasha, R. M.; Shipman, P. O.; Wood, T. E. *Macromolecules* **2005**, *38*, 9411.
(37) De Groot, F. M. F.; Fuggle, J. C.; Thole, B. T.; Sawatzky, G. A. *Physical Review B* **1990**, *41*, 928.
(38) Hatsui, T.; Takata, Y.; Kosugi, N. *Chemical Physics Letters* **1998**, *284*, 320.
(39) Petterson, L. G. M.; Hatsui, T.; Kosugi, N. *Chemical Physics Letters* **1999**, *311*, 299.
(40) Takata, Y.; Hatsui, T.; Kosugi, N.; Agui, A.; Magnuson, M.; Sathe, C.; Rubensson, J.-E.; Nordgren, J. *Journal of Electron Spectroscopy and Related Phenomena* **2001**, *114-116*, 909.
(41) Hatsui, T.; Kosugi, N. *Journal of Electron Spectroscopy and Related Phenomena* **2004**, *136*, 67.
(42) Wasinger, E. C.; De Groot, F. M. F.; Hedman, B.; Hodgson, K. O.; Solomon, E. I. *Journal of the American Chemical Society* **2003**, *125*, 12894.
(43) Hocking, R. K.; Wasinger, E. C.; De Groot, F. M. F.; Hodgson, K. O.; Hedman, B.; Solomon, E. I. *Journal of the American Chemical Society* **2006**, *128*, 10442.
(44) Hocking, R. K.; Wasinger, E. C.; Yan, Y.-L.; De Groot, F. M. F.; Walker, F. A.; Hodgson, K. O.; Hedman, B.; Solomon, E. I. *Journal of the American Chemical Society* **2007**, *129*, 113.
(45) Otero, E.; Urquhart, S. G. *in manuscript* **2008**.
(46) Wilks, R. G.; MacNaughton, J. B.; Kraatz, H. B.; Regier, T.; Moewes, A. *Journal of Physical Chemistry B* **2006**, *110*, 5955.
(47) Nesmeyanov, A. N.; Volkenay, N. A.; Bolesova, I. N. *Doklady Akademii Nauk SSSR* **1963**, *149*, 615.
(48) Miyake, M.; Yasuda, K.; Kashihara, T.; Teranishi, T. *Chemistry Letters* **1999**, 1037.
(49) Wei, G.; Saitoh, S.; Saitoh, H.; Fujiki, K.; Yamauchi, T.; Tsubokawa, N. *Polymer* **2004**, *45*, 8723.
(50) Sutherland, R. G. *Journal of Organometallic Chemistry Library* **1977**, *3*, 311.
(51) Abd-El-Aziz, A. S.; Bernardin, S. *Coordination Chemistry Reviews* **2000**, *203*, 219.
(52) Abd-El-Aziz, A. S. *Macromolecular rapid Communications* **2002**, *23*, 995.
(53) Sutherland, R. G.; Iqbal, M.; Piórko, A. *Journal of Organometallic Chemistry* **1986**, *302*, 307.
(54) Clack, D. W.; Warren, K. D. Metal-Ligand Bonding in 3d Sandwich Complexes. In *Structure and Bonding*; Springer: Berlin, **1980**; Vol. 39; pp 1.
(55) Le Beuze, A.; Lissillour, R.; Weber, J. *Organometallics* **1993**, *12*, 47.
(56) Abd-El-Aziz, A. S.; Baranski, A. S.; Piorko, A.; R.G., S. *Inorganica Chimica Acta* **1988**, *147*, 77.
(57) Ruiz, J.; Ogliaro, F.; Saillard, J.-Y.; Halet, J.-F.; Varret, F.; Astruc, D. *Journal of the American Chemical Society* **1998**, *120*, 11693.
(58) Houlton, A.; Miller, J. R.; Roberts, R. M. G.; Silver, J. *Journal of the Chemical Society, Dalton Transactions* **1990**, 2181.
(59) Houlton, A.; Miller, J. R.; Roberts, R. M. G.; Silver, J. *Journal of the Chemical Society, Dalton Transactions* **1991**, 467.
(60) Gassman, P. G.; Deck, P. A. *Organometallics* **1994**, *13*, 2890.

(61) Abd-El-Aziz, A. S.; De Denus, C. R.; Zaworotko, M. J.; MacGillivray, L. R. *Journal of Chemical Society, Dalton Transaction* **1995**, 3375.
(62) Abd-El-Aziz, A. S.; Todd, E. K.; Epp, K. M. *Journal of Inorganic and Organometallic Polymers* **1998**, *8*, 127.
(63) Abd-El-Aziz, A. S.; De Denus, C. R.; Todd, E. K.; Bernardin, S. A. *Macromolecules* **2000**, *33*, 5000.
(64) Roloff, A.; Meier, K.; Riediker, M. *Pure and Applied Chemistry* **1986**, *58*, 1267.
(65) Gill, T. P.; Mann, K. R. *Inorganic Chemistry* **1980**, *19*, 3007.
(66) Gill, T. P.; Mann, K. R. *Inorganic Chemistry* **1983**, *22*, 1986.
(67) Karatsu, T.; Shibuki, Y.; Miyagawa, N.; Takahara, S.; Kitamura, A.; Yamaoka, T. *Journal of Photochemistry and Photobiology A: Chemistry* **1997**, *107*, 83.
(68) Nesmeyanov, A. N.; Vol'kenau, N. A.; Shilovtseva, L. S. *Doklady Akademii Nauk SSSR* **1970**, *190*, 857.
(69) Schrenk, J. L.; Palazzotto, M. C.; Mann, K. R. *Inorganic Chemistry* **1983**, *22*, 4047.
(70) McNair, A. M.; Schrenk, J. L.; Mann, K. R. *Inorganic Chemistry* **1984**, *23*, 2633.
(71) Mann, K. R.; Blough, A. M.; Schrenk, J. L.; Koefod, S. R.; Freedman, D. A.; Matachek, J. R. *Pure and Applied Chemistry* **1995**, *67*, 95.
(72) Jakúbek, V.; Lees, A. J. *Chemical Communications* **1999**, 1631.
(73) Román, E.; Barrera, M.; Hernández, S. *Journal of the Chemical Society, Perkin Transactions II* **1988**, 939.
(74) Boyd, D. C.; Bohling, D. A.; Mann, K. R. *Journal of the American Chemical Society* **1985**, *107*, 1641.
(75) Chrisope, D. R.; Park, K. M.; Schuster, G. B. *Journal of the American Chemical Society* **1989**, *111*, 6195.
(76) Turner, C. A.; Ding, W.; Amster, I. J.; Kutal, C. *Coordination Chemistry Reviews* **2002**, *229*, 9.
(77) Ding, W.; Johnson, K. A.; Kutal, C.; Amster, I. J. *Analytical Chemistry* **2003**, *75*, 4624.
(78) Jakúbek, V.; Lees, A. J. *Inorganic Chemistry* **2000**, *39*, 5779.

CHAPTER 2 INSTRUMENTATION AND MEASUREMENTS

The electromagnetic spectrum of X-rays extends from ~250 eV to ~50 keV, with a separation at 10 keV that segregate soft X-rays (lower energy) from hard X-rays.[1] X-rays were observed for the first time in 1895 by W.C. Röntgen who was awarded the Physics Nobel prize in 1901 for his discovery. X-rays can be generated in an X-ray tube, where accelerated electrons collide with a metal surface (anode), ejecting core electrons from the surface of the metal target; relaxation of electrons from higher energy levels refill the core hole causing the emission of characteristic X-ray photons. The energy of the emitted photons depends on the material the anode is made of; e.g. tungsten, molybdenum, copper, cobalt. Such X-ray tubes are used extensively today, with some modifications, to produce X-rays for medical application as well as for research, e.g. laboratory crystallography.

However, for NEXAFS spectroscopy a tuneable, collimated and coherent source of radiation with high photon flux and very good polarization characteristics is required, thus justifying the use of synchrotrons. In a synchrotron, X-rays are produced from bending magnets (BM) and insertion devices (ID), an introduction to both devices is presented in §**2.1**. The process by which NEXAFS spectra are recorded will be described in §**2.2** followed by an overview of each beam line used to record the spectra presented in this thesis, §**2.3**.

2.1 Synchrotron Radiation

Synchrotron radiation is produced when electrons or positrons moving at relativistic velocities are accelerated in a curved path.[2] In a synchrotron, electrons with the energy of several tens of MeV are produced by an electron gun and are then accelerated by a linear accelerator up to several hundreds of MeV. The electrons are then injected into the booster ring where their energy is increased to several GeV. Periodically, the electrons are further injected into a storage ring where, due to centripedal acceleration of the bending magnet, the electrons emit electromagnetic radiation. The storage ring consists of straight portions where electrons travel in a collimated beam of ≈10μm diameter. The electron beam is deviated from its linear trajectory by magnets (bending magnets and insertion devices) which accelerate the electrons producing electromagnetic radiation. The energy lost by the electrons during this process is restored to them as they travel through the radio frequency cavities. As bending

magnets and insertion devices determine the properties of synchrotron light, they will be described in the next section.

2.1.1 Bending Magnet Sources

An electron moving at relativistic speed in a linear and uniform motion does not radiate. However, if an electron travels through a perpendicular magnetic field it undergoes a centripetal acceleration (i.e.: change in direction) which is associated with emission of electromagnetic radiation and bending of the electron trajectory. The electromagnetic radiation is emitted in a cone that is often described as a searchlight with a propagation direction tangent to the trajectory of the electron. The energy of the photons emitted covers the electromagnetic spectrum from near infrared to hard X-rays with a flux variable over the energy range as represented schematically in **Figure 2.1**.

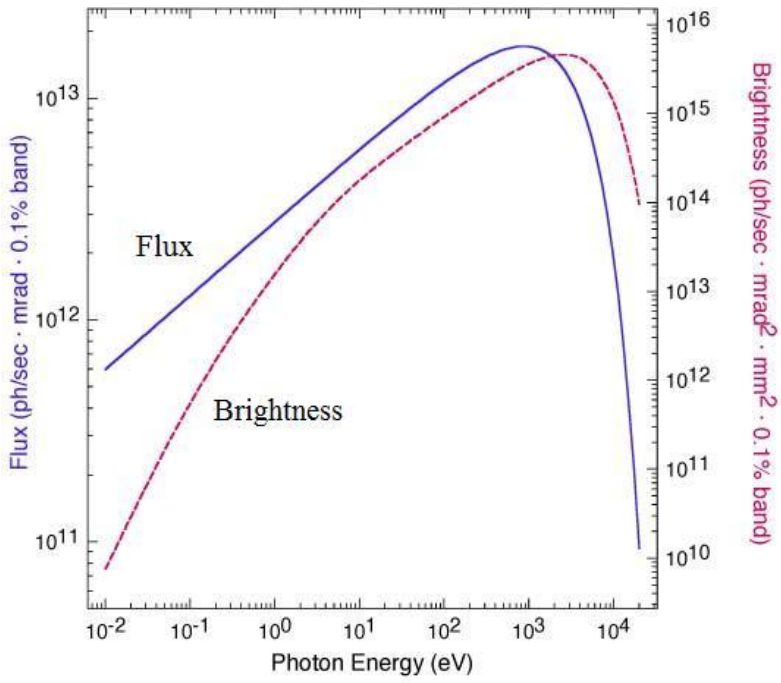

Figure 2.1 Flux and brightness curve for bending magnet located at the Advanced Light Source-Lawrence Berkeley National Laboratory, (ALS-LBNL).

X-ray radiation sources are often characterised by their brightness:

$$\text{Brightness} = \frac{\text{Photons/second}}{(\text{beam collimation})\ (\text{source area})\ (\text{spectral distribution})} \qquad \textbf{Equation 2.1}$$

Where the beam collimation in units of $mrad^2$ relates to how much the photon beam diverges as it propagates while the source area corresponds to the electron beam size in units of mm^2.

The spectral distribution refers to the photon energy range accepted for the measurements. By convention a bandwidth of 0.1% is used; i.e. for a measurement at a given energy (ω), photons with energy $\omega \pm \Delta\omega$ so that $\Delta\omega/\omega = \pm 0.1\%$, are recorded.

The electric component of electromagnetic radiation is parallel to the acceleration vector and therefore the light emitted by a bending magnet is linearly polarized in the plane of the storage ring. This is not true for the radiation emitted above or below the plane of the storage ring, which are elliptically polarized. These polarization properties will be discussed below.

2.1.2 Insertion Device Sources

The characteristics of radiation produced by BM, mostly brightness and critical energy, can be increased by increasing the bending magnetic field or using a higher energy ring. However serious practical complications and cost issues are associated with this. In order to generate brighter light with greater coherence over a wider energy range, so called insertion devices (ID) were designed.

ID consist in periodic arrays of magnets (N_m) located above and below the electron pathway of a straight section of the storage ring. As the electrons travel through an ID they are forced to wiggle, emitting photons at each change of trajectory ($2N_m$). There are two types of ID, wigglers and undulators, which produce linear polarized radiation. Elliptically polarized undulators are undulator type ID that also produce elliptically and circular polarized light; all ID will be described below.

2.1.2.1 Wigglers

In wigglers, the magnetic field can be very large leading to large oscillation amplitudes and high energy radiation; i.e. between 10 keV to 20 keV. Due to large oscillation amplitudes, the cone of radiation remains large, comparable to that obtained from BM, but with a total brightness $2N_m$ greater than at a BM ($N_m = 1$). **Figure 2.2** presents schematics of the radiation profiles and brightness curves summarizing the characteristics of BM and wigglers.

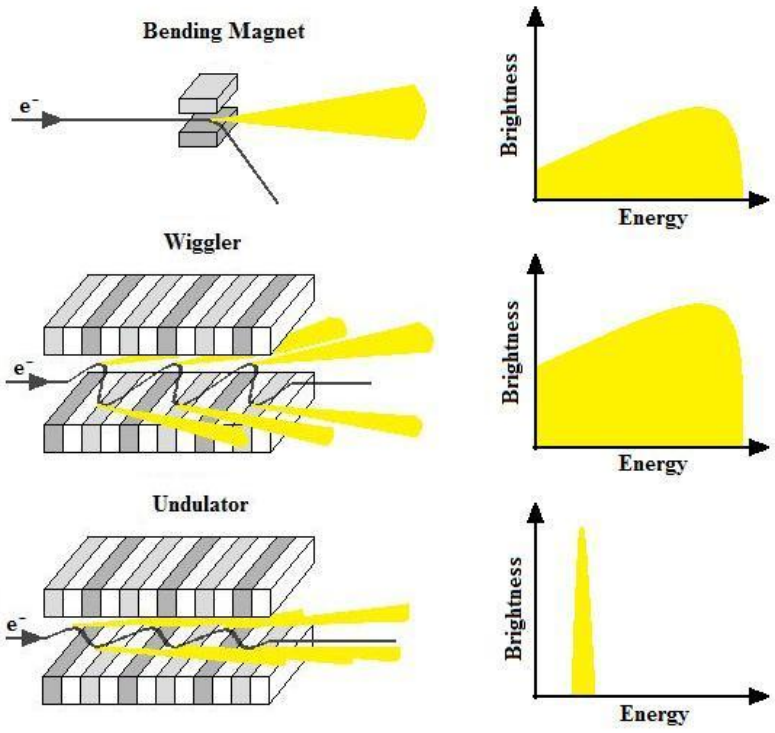

Figure 2.2 Schematic representation of bending magnet, wiggler and undulator and diagram of typical brightness profile produced by these radiation sources.

2.1.2.2 Undulator

The magnetic field in undulators are less than in wigglers leading to smaller oscillation amplitudes and therefore a narrower radiation cone and a smaller spectral width, as illustrated in **Figure 2.2**. The tunability of the narrow radiation energy band is achieved by changing the gap between the two rows of magnets, thus changing the magnetic field experienced by the electrons.

2.1.2.3 Elliptically polarized undulator

Wigglers and undulators produce linearly polarized radiation in the plane of the rows of magnets, which typically coincide with the plane of the storage ring; i.e. horizontal polarized light. Elliptically polarized undulators (EPU) consists of four quadrants of periodic magnets with a row of two quadrants above the electron pathway and a row below.[3,4] In each row, one quadrant is fixed and one is movable longitudinally along the electron's axis (z), as illustrated in **Figure 2.3**. Translation of the four quadrants changes the phase between the vertical and horizontal components of the magnetic field (B_x and B_y). When B_x and B_y are 90º out of phase circularly polarized X-rays are generated and for 180º phase shift, vertical polarized X-ray.

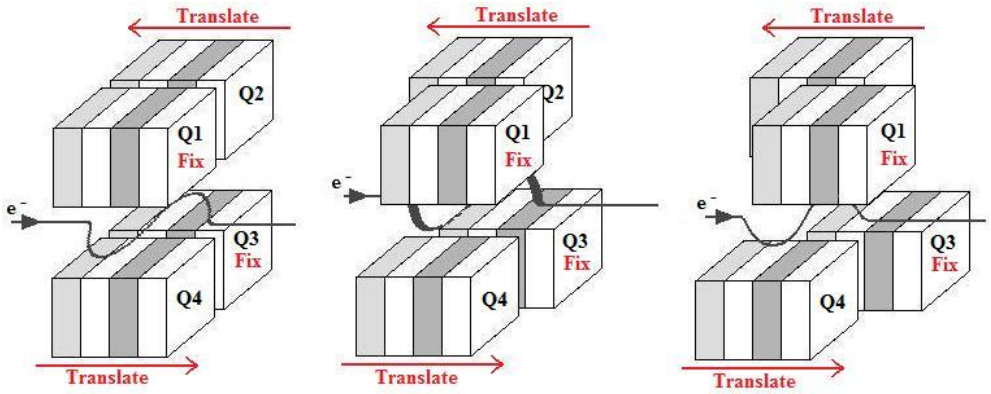

Figure 2.3 Schematic representation of elliptically polarized undulator with a) 0º phase shift, b) 90º phase sift and c) 180º phase shift leading to horizontal linear, circular and vertical linear magnetic field respectively.

2.2 Measuring NEXAFS Spectra

There are various ways of measuring X-ray absorption. The most common methods, represented schematically in **Figure 2.4**, involve measurement of transmitted photons, photons in - electrons out, or photons out caused by secondary phenomena (photoelectron emission, Auger electron emission, secondary electron emission, fluorescence emission and drain currents). All NEXAFS spectra presented in this dissertation were collected using transmission mode or total electron yield (TEY) mode, both of which will be described below.

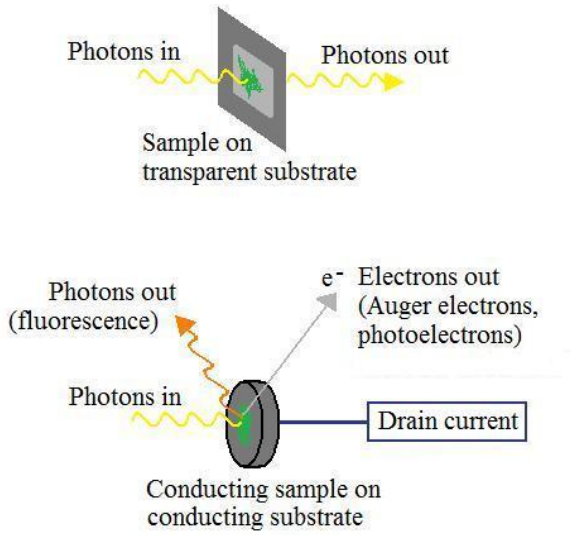

Figure 2.4 Schematic representation of the various methods used to measure X-ray absorption in a) transmission and b) Fluorescence yield by measuring emitted fluorescence photons, Auger electron yield and partial electron yield (PEY) by measuring emitted electrons and total electron yield (TEY) by measuring drain current.

2.2.1 Detection Techniques

2.2.1.1 Transmission

The measurement of X-ray absorption in transmission mode follows a typical layout where the sample is placed between a source of X-rays and a detector, which measures the transmitted photon flux. The signal recorded is referred to as sample transmission spectrum (I) and its measurement as a function of energy leads to an absorption spectrum. Another spectrum recorded in absence of the sample allows monitoring the incident photon flux (I_0). The X-ray transmission spectrum is then obtained by calculating the optical density (OD) according to:

$$\text{OD} = -\ln\frac{I}{I_0} \qquad \textbf{Equation 2.2}$$

The optical density is distinctive for all elements contained in a sample of thickness *t* (cm) through:

$$\text{OD} = \mu(E)\times\rho\times t \qquad \textbf{Equation 2.3}$$

Where at a particular energy (E) μ, the mass absorption coefficient ($cm^2.g^{-1}$) and ρ, the sample density ($g.cm^{-3}$) are element specific with μ being related to the atomic absorption cross section σ_x by:

$$\mu = \frac{N_A}{MW}\sum_i n_i\sigma_{xi} \qquad \textbf{Equation 2.4}$$

Where N_A is the Avogadro's number, σ_{xi} the absorption cross section for the n_i atoms of each element "i" and the molecular weight $MW = \sum_i n_i A_i$ where A_i is the atomic weight.[5]

NEXAFS spectra recorded in transmission mode, i.e. OD versus energy, provide information on the variations in transition probability as a function of energy.

2.2.1.2 Total Electron Yield

The formation of a core-hole due to photo-excitation of a core electron upon X-ray absorption creates short lived core excited states and leads to a series of relaxation processes. These relaxation processes are lead to the emission of fluorescence photons and Auger electrons, as represented in **Figure 2.4**. NEXAFS spectrum can be generated by measuring the quantity of emitted photons or electrons as a function of incident photon energy. The relative probability of each process is related to the atomic number (Z) of the elements

present in the sample. For absorption edges below ~2000 eV, as in C 1s, N 1s, O 1s and Fe 2p edges, Auger electron emission dominates the relaxation processes. As represented in **Figure 2.5** Auger electrons are created when a valence electron decays in order to refill the core-hole vacancy. During the decay process the excess of energy released by the valence electron is transferred to another valance electron, the Auger electron, which is then emitted.

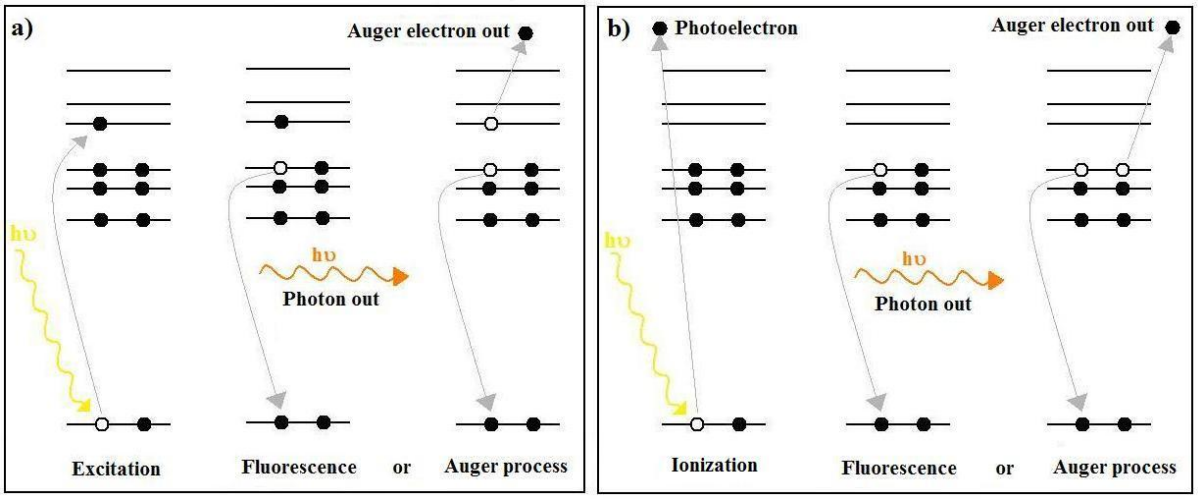

Figure 2.5 Schematic representation of relaxation processes following X-ray absorption leading to a) excitation and b) ionization and followed by emission of fluorescence photons and auger electrons.

An energy analyser located near the surface of the sample can detect the emitted electrons and discriminate them based on their kinetic energy. By setting the energy window of the energy analyser to a narrow range centred on the energy of the Auger peak, one can measure the Auger electron yield (AEY) as a function of excitation energy. If a larger energy window is selected, all emitted electrons, apart from greatly scattered electrons with low kinetic energy, are recorded; this method is referred to as partial electron yield (PEY). An alternative technique that involves recording the drain current from the sample allows measuring the quantity of all emitted electrons (i.e.: all photoelectrons and Auger electrons); this method is referred to as total electron yield (TEY).

The incident photon flux (I_0) is monitored by measuring the drain current from a mesh located upstream from the sample and is used to normalize the sample current according to:

$$\mathrm{TEY} = \frac{I}{I_0} \qquad \textbf{Equation 2.5}$$

Details on the edge-specific TEY normalization methods used in this thesis will be described in **Chapter 7**.

2.2.2 Soft X-ray Spectromicroscopy Using Transition Detection Technique

Spectromicroscopy is a technique that combines both high resolution X-ray spectroscopy and high spatial resolution (<15 nm) X-ray imaging.

In an X-ray microscope monochromatic light enters the measurement chamber through a silicon nitride (Si_3N_4) window that isolates the microscope from the high vacuum in the beam-line. The light then reaches a Fresnel zone plate (ZP) that blocks in its centre unwanted zero order light and focuses first order light into a very small spot on the sample (40 nm). Zone plates are circular variable-line-spacing diffractive focusing devices made of alternated opaque and transparent concentric rings whose thickness decreases as the radius of the ZP increases.

An Order Sorting Aperture (OSA) located between the ZP and the sample prevents light diffracted with a higher diffraction order as well as higher order light, i.e. light with n times (with n an integer) the wavelength of first order light, from reaching the sample, see **Figure 2.6**.[6]

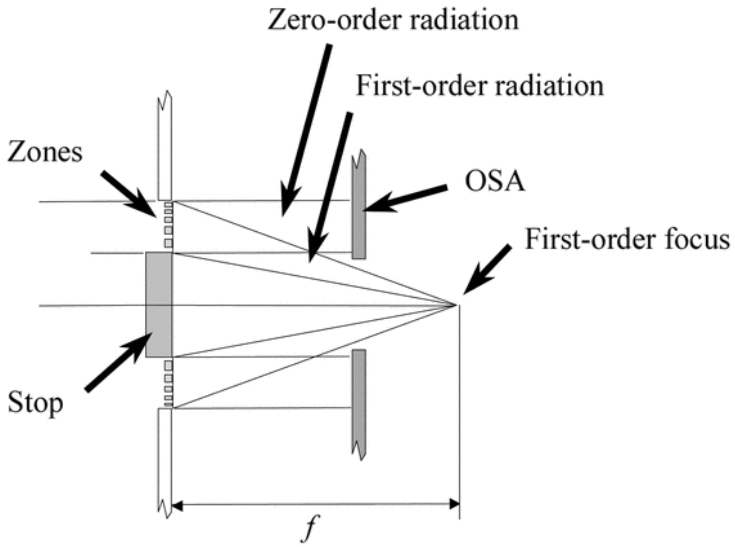

Figure 2.6 Focusing scheme of a STXM.[6] [Reprinted with permission from Journal of Synchrotron Radiation, 10, A. L. D. Kilcoyne, T. Tyliszczak, W. F. Steele, S. Fakra, P. Hitchcock, K. Franck, E. Anderson, B. Harteneck, E. G. Rightor, G. E. Mitchell, A. P. Hitchcock, L. Yang, T. Warwick and H. Ade, Interferometer-controlled scanning transmission X-ray microscopes at the Advanced Light Source, 125-136, Copyright 2003, with permission from International Union of Crystallography.]

The focal length (*f*) of a ZP is energy dependent and tuning of X-ray energies during a measurement requires the ZP position to be continuously adjusted with the OSA kept properly aligned so the focus point remains on the sample. Precise translations of the ZP

along the light pathway (z direction) and of the OSA in the x,y plane is achieved with the help of very precise stages whose displacements are monitored by laser interferometers.[6]

The samples are mounted on a piezoelectric controlled stage that allows scanning of the sample in x and y directions while monitoring the photon flux transmitted through the sample.

A detector placed after the sample and made of phosphor particles converts the transmitted X-ray photons into visible light, which is then recorded by a Photomultiplier Tube (PMT).

NEXAFS spectra are generated using the image sequencing technique described in **Figure 2.7**.[7] For each image recorded at a different energy an area of interest is selected (dark pentagon in **Figure 2.7**) and the amount of photon transmitted for each pixel over this area is averaged to lead to the sample signal (I).

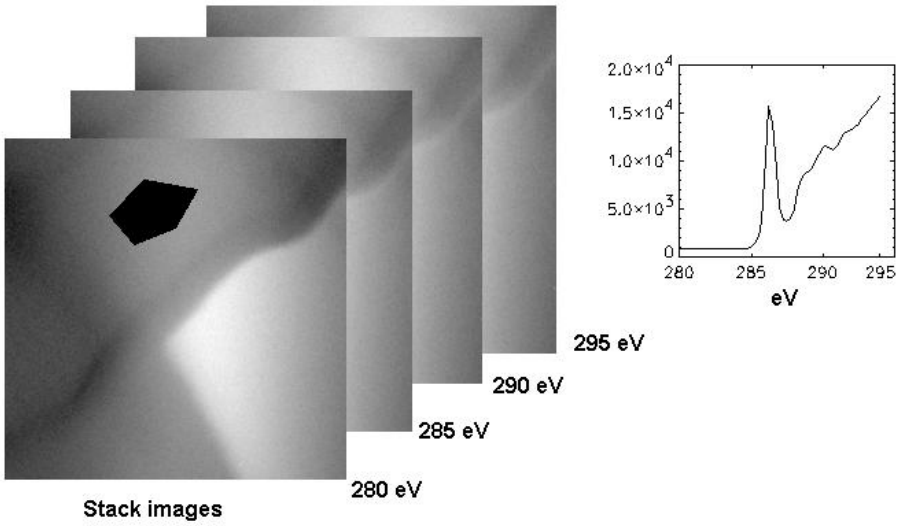

Figure 2.7 Schematic representation of NEXAFS spectrum (OD versus energy) generated from an image stack. The number of count are averaged per pixel over the area marked off in black for this figure.

As mentioned above the microscope chamber is separated from high vacuum by a silicon nitride window, and only medium vacuum (10^{-3} to 1 Torr) is required during the measurements. Lowering the pressure in the measurement chamber to 100mTorr prevents unwanted absorption of the photon beam by carbon, nitrogen and oxygen species contained in air, which would lower the photon flux and could interfere with the measurements. Such conditions of pressure allow for measurements of compounds which cannot sustain vacuum conditions, such as biological samples.

Transmission measurements require the sample to be partially transparent to X-rays over the energy range scanned. The optimum sample thickness for a given material over a specific energy range can be estimated from **Equations 2.2** and **2.3** and was determined to be on the order of 100 nm for measurements at C 1s edge, 300 nm at N 1s and 400 nm at O 1s edge. In order to achieve reliable sample thickness, thin sample films can be prepared by chemical vapour deposition (CVD) where the film thickness is monitored by a quartz crystal microbalance during the deposition (see § **4.3.1.1**). Alternative methods such as spin casting or solution casting were also found efficient in preparing thin sample films (see § **4.3.1.1.3** and § **4.3.1.2**).

The most common substrates used for solid sample are 75-150nm thick Si_3N_4, SiO or Carbon membrane windows or coated grids.

Liquid samples may also be examined by X-ray spectromicroscopy using wet cells where a small drop of sample is trapped between two Si_3N_4 membrane windows glued to each other. The pressure inside the microscope is then maintained at atmospheric pressure by flushing the chamber continuously with helium, this is done to prevent pressure discrepancy between inside and outside the wet cell (see § **4.3.1.4**).

2.2.3 Soft X-ray Spectroscopy Using TEY Detection Technique

NEXAFS spectra recorded from soft X-ray spectroscopy in TEY mode are generated by monitoring the drain current from the sample while the energy of the incident photons is scanned over the desired energy range.

The main advantage to X-ray spectroscopy is its very low sample preparation requirement. Typically milligram amounts of compound are pressed onto the surface of a conducting substrate. The most commonly used substrates include indium foil, copper tape, carbon tape and doped silicon wafers. For hard surface substrates, such as doped silicon wafers, the samples may need to be solution cast (see **Chapter 9**). The choice of substrate depends on the absorption edge the sample will be examined at (to avoid contribution from the substrate), the conductivity of the sample and the reactivity of the sample toward the substrate.

The pressure inside the measurement chambers is typically 10^{-7} to 10^{-8} Torr. This requires that all samples investigated must have very low vapour pressure to prevent desorption of the chemical during measurement which could then contaminate the surface of

the various element of the beam-line. Additionally, the measurement of the drain current from the sample implies that both the sample and the substrate must be conducting.

2.3 Beam-Line Used for NEXAFS Spectroscopy

NEXAFS spectra collected for this dissertation were recorded from six different beam-lines equipped with two types of end-stations dedicated to either soft X-ray spectromicroscopy, using transmission mode, or soft X-ray spectroscopy, using TEY detection mode. Specifics of the beam-lines are reviewed below.

2.3.1 Spectromicroscopy Beam-Lines

All the spectra presented in **Chapter 4,** dedicated to XNCD study of small chiral organic molecules, were recorded using the Scanning Transmission X-ray Microscopes (STXM) located at the Advanced Light Source (ALS, Lawrence Berkeley National Laboratory, University of California, US) on beam-lines 5.3.2. and 11.0.2. Also the spectrum of ferrocenium, which required the use of inert substrate, (see **Chapter 6)**, was recorded on the STXM located on beam-line 10ID1at the CLS.

Beamline 5.3.2. at ALS is dedicated to polymer science and covers an energy range from 250 eV to 700 eV. The light produced by a bending magnet is reflected by a toroidal mirror onto a spherical grating monochromator (SGM) and then enters the microscope chamber through a silicon nitride window, isolating the measurement chamber from the high vacuum of the beam-line. (see **Figure 2.8**).[8]

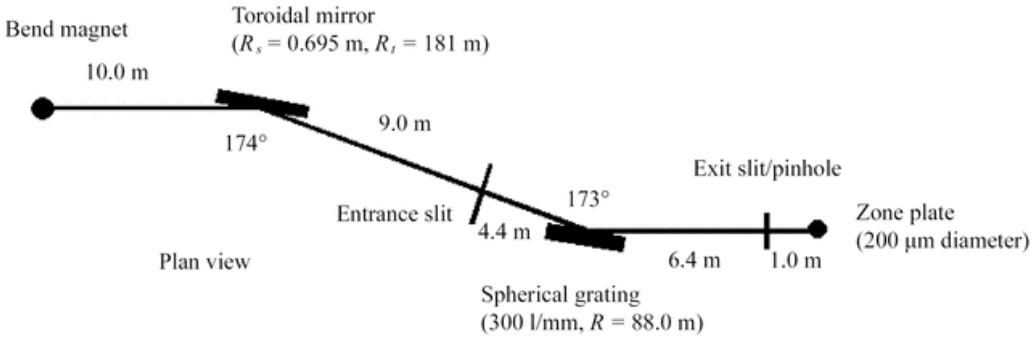

Figure 2.8 Layout of beam-line 5.3.2. located at the ALS.[8] [Reprinted with permission from Journal of Synchrotron Radiation, 9, T. Warwick, H. Ade, D. Kilcoyne, M. Kritscher, T. Tylisczcak, S. Fakra, A. Hitchcock, P. Hitchcock and H. Padmore, A new bend-magnet beamline for scanning transmission X-ray microscopy at the Advanced Light Source, 254-257, Copyright 2002, with permission from International Union of Crystallography.]

The STXM located at beam-line 11.0.2 at the ALS is dedicated to molecular environmental science. The light produced by an EPU is focused by a cylinder mirror onto the pre-mirror of a monochromator chamber that contains two gratings covering an energy range from 75 eV to 2150 eV.[9] The monochromatized light then travels to two toroidal mirrors which direct the beam through the exit slits and into the STXM chamber (labelled 1 in **Figure 2.9**).

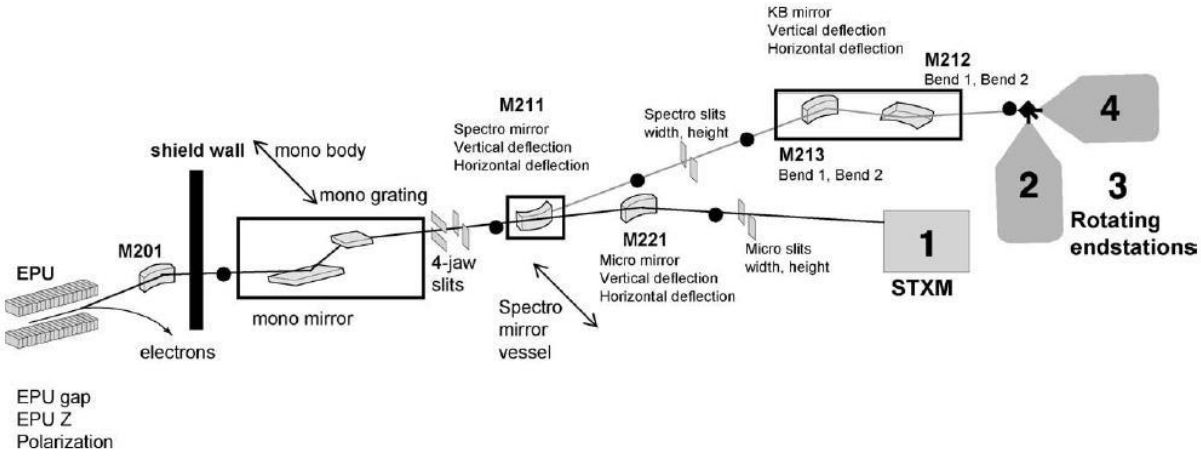

Figure 2.9 Layout of beam-line 11.0.2. located at the Advanced Light Source, Berkeley-California.[9] [Reprinted with permission from Journal of Electron Spectroscopy and Related Phenomena, 150, H. Bluhm, K. Andersson, T. Araki, K. Benzerara, G.E. Brown, J.J. Dynes, S. Ghosal, M.K. Gilles, H.-Ch. Hansen, J.C. Hemminger, A.P. Hitchcock, G. Ketteler, A.L.D. Kilcoyne, E. Kneedler, J.R. Lawrence, G.G. Leppard, J. Majzlam, B.S. Mun, S.C.B. Myneni, A. Nilsson, H. Ogasawara, D.F. Ogletree, K. Pecher, M. Salmeron, D.K. Shuh, B. Tonner, T. Tyliszczak, T. Warwick and T.H. Yoon, Soft X-ray microscopy and spectroscopy at the molecular environmental science beamline at the Advanced Light Source, 86-104, Copyright 2005, with permission from Elsevier.]

The Spectromicroscopy (SM) beamline located at the CLS (10ID-1) and dedicated to polymer science and biological applications is equipped with an EPU that shines light onto a cylindrical mirror, which then directs the photons onto a plane grating monochromator (see **Figure 2.10**).[10] The photons are then reflected by a toroidal mirror through the exit slit into the STXM chamber. The energy range covered by the SM beam-line extends from 100 eV to 2000 eV.

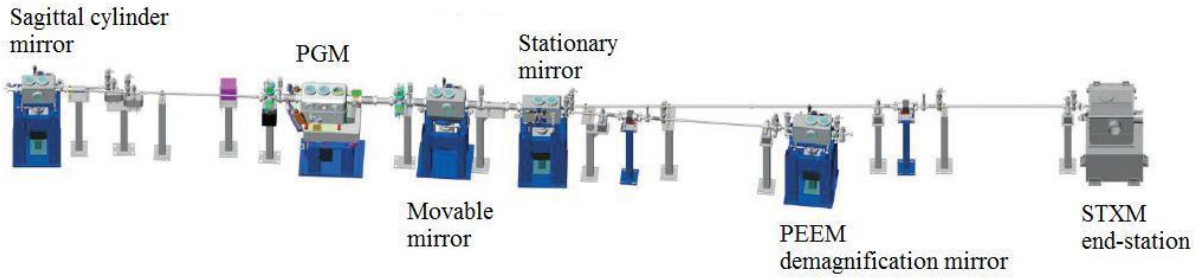

Figure 2.10 Layout of SM beam-line 10ID-1 located at the CLS, Saskatoon-Saskatchewan.[10] [Reprinted with permission from Canadian Light Source Activity Report, 2001-2004, K. Kaznacheyev, Soft X-ray Spectromicroscopy (SM), 67-73, Copyright 2005, with permission from Canadian Light Source.]

2.3.2 Spectroscopy Beam-Lines

The study of organometallic complexes and polymers required the acquisition of NEXAFS spectra at six different absorption edges corresponding to an energy range from 135 eV (P 2p) up to 2472 eV (S 1s) and the use of three different beam-lines and end-stations.

P 2p and S 2p NEXAFS spectra were recorded using the Canadian Synchrotron Radiation Facility (CSRF) Mark IV Grasshopper beam-line (port 091) located at the Synchrotron Radiation Centre (SRC, University of Wisconsin-Madison, USA), located in Madison, Wisconsin.[11] The light produced by a BM is reflected by a first mirror that focuses the beam in a vertical plane on a mirror/slit. The X-rays then travel to a "grasshopper-type" monochromator, which covers an energy range from 21 eV to 1000 eV, and through an exit slit before reaching the end-station where NEXAFS spectra are recorded in TEY mode.

C 1s and Fe 2p NEXAFS spectra have been recorded on the Spherical Grating Monochromator Soft X-ray Spectroscopy beam-line (11ID-1) located at the Canadian Light Source (CLS, University of Saskatchewan, Canada). The monochromator chamber and exit slits mechanism were transferred from former SGM beamline located at SRC.[12] Electromagnetic radiation from an undulator is reflected by two plane mirrors and one cylindrical mirror through liquid cooled entrance slits into a Dragon – type monochromator containing three spherical gratings (see **Figure 2.11**).[13] Monochromatized light then travels through movable exit slits down to a toroidal refocusing mirror before reaching the end-station.[14] The use of three gratings allows coverage of an energy range from 250 eV up to 2000 eV.

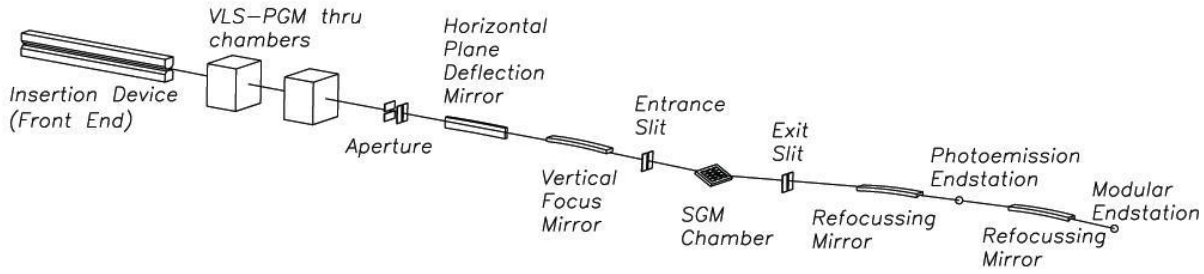

Figure 2.11 Layout of SGM beam-line 11ID-1 located at the CLS, Saskaton-Saskatchewan.[13] [Reprinted with permission from Canadian Light Source Activity Report, 2001-2004, I. Coulthard, Spherical Grating Monochromator (SGM), 65-66, Copyright 2005, with permission from Canadian Light Source.]

P 1s and S 1s NEXAFS spectra were acquired on the CSRF Double Crystal Monochromator (DCM) beam-line located on port 093 at the SRC. Light produced by a bending magnet penetrates the double crystal monochromator chamber equipped with a boomerang-Golovchenko type mechanism used to coordinate the rotation and translation motions of the two monochromators.[15] The monochromatized beam is then focused by a cylindrical mirror onto the sample target, as schematically represented **Figure 2.9**. The DCM beam-line covers an energy range from 1500 eV to 4000 eV.

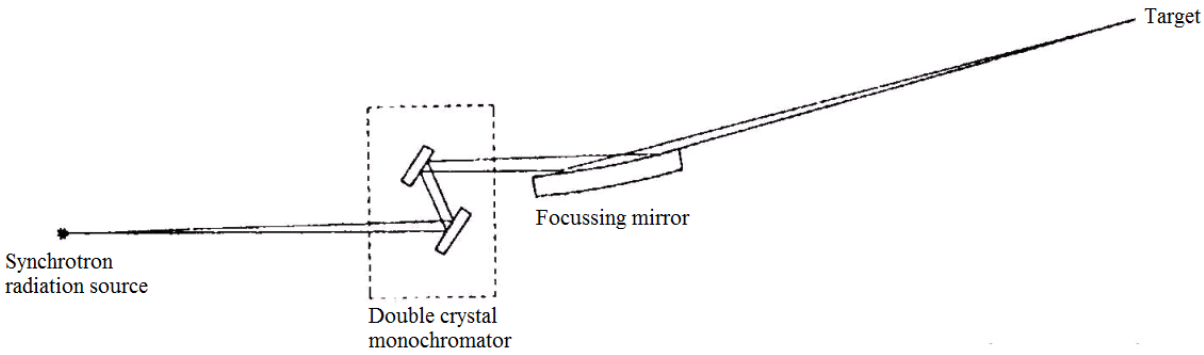

Figure 2.12 Layout of the double crystal monochromator beam-line located port 093 at the SRC.[16] [Reprinted with permission from Nuclear Instruments and Methods in Physics Research Section A: Accelerators, Spectrometers, Detectors and Associated Equipment, 316, B. X. Yang, F. H. Middleton, B. G. Olsson, G. M. Bancroft, J. M. Chen, T. K. Sham, K. Tan and D. J. Wallace, The design and performance of a soft X-ray double crystal monochromator beamline at Aladdin, 422-436, Copyright 1992, with permission from Elsevier.]

2.4 References

(1) Attwood, D. *Soft X-rays and Extreme Ultraviolet Radiation; Principles and Applications*; Cambridge University Press: New York, **2007**.

(2) Margaritondo, G. *Introduction to Synchrotron Radiation*; Oxford University Press, Inc.: New York, **1988**.

(3) Marks, S.; Cortopassi, C.; DeVries, J.; Hoyer, E.; Leinbach, R.; Minamihara, Y.; Padmore, H.; Pipersky, P.; Plate, D.; Schlueter, R.; Young, A. "The Advanced Light Source elliptically polarizing undulator"; Proceeding of the Particle Accelerator Conference, 17th, **1997**, Vancouver, B.C.

(4) Young, A. T.; Arenholz, E.; Mark, S.; Schlueter, R.; Steier, C.; Padmore, H. A.; Hitchcock, A. P.; Castner, D. G. *Journal of Synchrotron Radiations* **2002**, *9*, 270.

(5) Thompson, A.; Attwood, D.; Gullikson, E.; Howells, M.; Kim, K.-J.; Kirz, J.; Kortright, J.; Lindau, I.; Pianetta, P.; Robinson, A.; Scofield, J.; Underwood, J.; Vaughan, D.; Williams, G. *X-ray Data Booklet*, second ed.; Center for X-ray Optics; Advanced Light Source: Berkeley, **2001**.

(6) Kilcoyne, A. L. D.; Tyliszczak, T.; Steele, W. F.; Fakra, S.; Hitchcock, P.; Franck, K.; Anderson, E.; Harteneck, B.; Rightor, E. G.; Mitchell, G. E.; Hitchcock, A. P.; Yang, L.; Warwick, T.; Ade, H. *Journal of Synchrotron Radiation* **2003**, *10*, 125.

(7) Jacobsen, C.; Wirick, S.; Flynn, G.; Zimba, C. *Journal of Microscopy* **2000**, *197*, 173.

(8) Warwick, T.; Ade, H.; Kilcoyne, D.; Kritscher, M.; Tylisczcak, T.; Fakra, S.; Hitchcock, A.; Hitchcock, P.; Padmore, H. *Journal of Synchrotron Radiations* **2002**, *9*, 254.

(9) Bluhm, H.; Andersson, K.; Araki, T.; Benzerara, K.; Brown, G. E.; Dynes, J. J.; Ghosal, S.; Gilles, M. K.; Hansen, H.-C.; Hemminger, J. C.; Hitchcock, A. P.; Ketteler, G.; Kilcoyne, A. L. D.; Kneedler, E.; Lawrence, J. R.; Leppard, G. G.; Majzlam, J.; Mun, B. S.; Myneni, S. C. B.; Nilsson, A.; Ogasawara, H.; Ogletree, D. F.; Pecher, K.; Salmeron, M.; Shuh, D. K.; Tonner, B.; Tyliszczak, T.; Warwick, T.; Yoon, T. H. *Journal of Electron Spectroscopy and Related Phenomena* **2006**, *150*, 86.

(10) Kaznacheev, K. "Soft X-ray Spectromicroscopy (SM)," University of Saskatchewan, **2005**.

(11) Tan, K. H.; Bancroft, G. M.; Coatsworth, L. L.; Yates, B. W. *Canadian Journal of Physics* **1982**, *60*, 131.

(12) Yates, B. W.; Hu, Y. F.; Tan, K. H.; Retzlaff, G.; Cavell, R. G.; Sham, T. K.; Bancroft, G. M. *Journal of Synchrotron Radiation* **2000**, *7*, 296.

(13) Coulthard, I. "Spherical Grating Monochromator (SGM)," University of Saskatchewan, **2005**.

(14) Regier, T.; Paulsen, J.; Wright, G.; Coulthard, I.; Tan, K.; Sham, T. K.; Blyth, R. I. R. "Commissioning of the Spherical Grating Monochromator Soft X-ray Spectroscopy Beamline at the Canadian Light Source"; Synchrotron Radiation Instrumentation: Ninth International Conference on Synchrotron Radiation Instrumentation, **2006**, Daegu, Korea.

(15) Yang, B. X.; Middleton, F. H.; Olsson, B. G.; Bancroft, G. M.; Chen, J. M.; Sham, T. K.; Tan, K.; Wallace, D. J. *Review of Scientific Instruments* **1992**, *63*, 1355.

(16) Yang, B. X.; Middleton, F. H.; Olsson, B. G.; Bancroft, G. M.; Chen, J. M.; Sham, T. K.; Tan, K.; Wallace, D. J. *Nuclear Instruments and Methods in Physics Research A* **1992**, *316*, 422.

CHAPTER 3 CALCULATIONS

During the early decades of NEXAFS spectroscopy, use of the "building block approach" to assign spectral features was a common practice. The building block principle uses the spectra of simple molecules (i.e.: pseudodiatomic and functional group units) to assign more complex assemblies.[1-4] This method relies on the assumption that the excited state is highly localized on the core excited atom, and was found to be satisfying for molecules without conjugation, but failed when applied to molecules with a higher level of electron delocalization. The alternative method to building block approach makes use of computational methods to simulate XAS spectra. The NEXAFS spectra presented in this dissertation were assigned with the help of three different computational methods, each implementing a different quantum chemistry model. This chapter gives an overview of the computational methods. The purpose of section **3.1** is to provide a quantum chemistry background to introduce sections **3.2**, **3.3** and **3.4** dedicated to the description of each method; Extended Hückel Molecular Orbital theory, *ab initio* theory and Density Functional Theory respectively. Further information on quantum mechanics and computational chemistry may be found in books dedicated to this field such as the one by C.J. Cramer from which the following section has been greatly inspired.[5-7]

3.1 Quantum Chemistry

Quantum mechanics describes atoms and molecules in terms of their wave character, via a wavefunction (Ψ) and observable, i.e. physical variable that can be measured such as position, momentum or energy, which is obtained by the action of mathematical operators (Ω) on a wavefunction (*f*) to transform it, in most cases, into another function. When the output function is the same as the input function multiplied by a constant (ω), or in mathematical form:

$$\Omega f = \omega f \qquad \textbf{Equation 3.1}$$

the function is termed an eigenfunction, the constant an eigenvalue and the equation an eigenvalue equation.

The celebrated time-independent Schrödinger equation is an eigenvalue equation where the Hamiltonian operator (H), which describes the total energy of the system (the sum

of the kinetic and potential energies), acts upon an eigenfunction Ψ, corresponding for example to the energy wavefunction of the system, and returns to the eigenvalues (E), in this case the allowed energy values of the system:

$$H\,\Psi = E\,\Psi \qquad \textbf{Equation 3.2}$$

The key to all quantum molecular calculations is to solve **Equation 3.2** (the time-independent Schrödinger equation), in other words, to find the energies and energy wavefunctions of the Hamiltonian operator describing the system.

The Hamiltonian operator can be separated into the kinetic energy (T) for the electrons and the nuclei, and the potential energy (V) that corresponds to the attraction between the electrons and the nuclei, and the repulsion between electrons and inter-nuclear repulsion.

$$H = -\sum_i \frac{(h/2\pi)^2}{2m_e}\nabla_i^2 - \sum_k \frac{(h/2\pi)^2}{2m_k}\nabla_k^2 - \sum_i\sum_k \frac{e^2 Z_k}{r_{ik}} + \sum_{i<j}\frac{e^2}{r_{ij}} + \sum_{k<l}\frac{e^2 Z_k Z_l}{r_{kl}} \qquad \textbf{Equation 3.3}$$

$$\text{Or} \qquad H = T_{ele} + T_{Nuc} + V_{Nuc\text{-}ele} + V_{ele\text{-}ele} + V_{Nuc\text{-}Nuc} \qquad \textbf{Equation 3.4}$$

where h is the Planck's constant, m_e is the mass of an electron (from i through j), m_k (m_l) the mass of nucleus k (l) and Z_k (Z_l) the atomic number of atom k (l), e the charge of the electron, r_{ij} (r_{lk}) the distance between electrons i and j (between nuclei l and k) and ∇ denotes the Laplacian operator.[5] The complexity of this equation is such that series of approximations have been made to simplify **Equation 3.2**.

M. Born and J.R. Oppenheimer suggested the following approximation: as the mass of nuclei are much greater than the mass of electrons, nuclei can be considered as immobile (nearly zero kinetic energy and constant inter-nuclear repulsion energy) and only the motion of electrons is considered. Application of the Born-Oppenheimer approximation causes **Equation 3.4** to be rewritten as:

$$H_{ele} = T_{ele} + V_{Nuc\text{-}ele} + V_{ele\text{-}ele} \qquad \textbf{Equation 3.5}$$

and the electronic Schrödinger equation as:

$$H_{ele}\,\Psi = E_{ele}\,\Psi \qquad \textbf{Equation 3.6}$$

Lets now consider the simplest case of a single electron in an atom for which the electronic Schrödinger equation can be solved exactly, e.g. hydrogenic wavefunctions. These wavefunctions may then be interpreted for multielectron atoms as atomic orbitals (AOs) $1s^2$, $2s^2$, $2p^6$, etc… Lets assume that such AOs can be used to build more complicated wavefunctions in order to approximate the molecular orbitals (MO) of a multielectron

molecule. In other words, lets find a set of trial wavefunctions ϕ_j constructed by a linear combination of atomic-like wavefunctions φ_i (or basis functions), or in a mathematical form:

$$\phi_j = \sum_{i=1}^{N} a_{ij}\varphi_i \qquad \textbf{Equation 3.7}$$

In such a Linear Combination of Atomic Orbital – Molecular Orbital (LCAO-MO) the set of N basis functions, or "basis set", are provided and only the a_{ij} coefficients need to be calculated.

The way out is to make use of the variational principle that states that when solving the Schrödinger equation there must be one observable lower than all others, corresponding to the ground state energy (E_0). The wavefunctions ψ_0 associated with E_0 can then be interpreted as the ground state wavefunction.

Lets now introduce the equation for the operator expectation value (right hand side of **Equation 3.8**) defined as the mean value of the observable $\langle E \rangle$, i.e. the mean energy value:

$$\langle E \rangle = \frac{\int \phi_i H \phi_j dr}{\int \phi_i \phi_j dr} \qquad \textbf{Equation 3.8}$$

From **Equation 3.7** and **3.8** we have:

$$\langle E \rangle = \frac{\int \left(\sum_i a_i \varphi_i \right) H \left(\sum_j a_j \varphi_j \right) dr}{\int \left(\sum_i a_i \varphi_i \right)\left(\sum_j a_j \varphi_j \right) dr} \qquad \textbf{Equation 3.9}$$

According to the variational principle to approach the ground state wavefunctions, one must solve for all coefficients a_{ij} that lead to the minimal energy E_0, the ground state energy. Since E is a function its minimal value corresponds to its derivative over all variable, i.e. a_{ij} (all $a_{ij} = a_k$), equal to zero, or

$$\frac{\partial E}{\partial a_k} = 0 \qquad \textbf{Equation 3.10}$$

A more convenient way to write **Equation 3.9** is:

$$E = \frac{\sum_{ij} a_i a_j \int \varphi_i H \varphi_j dr}{\sum_{ij} a_i a_j \int \varphi_i \varphi_j dr} = \frac{\sum_{ij} a_i a_j H_{ij}}{\sum_{ij} a_i a_j S_{ij}} \qquad \textbf{Equation 3.11}$$

where the integrals H_{ij} and S_{ij} in the right hand side of the equation respectively correspond to the resonance integral and the overlap integral of two basis functions (φ).

Partial differentiation of **Equation 3.11** leads to *N* equations of the form:

$$\sum_{i=1}^{N} a_i \left(H_{ki} - ES_{ki} \right) = 0 \qquad \textbf{Equation 3.12}$$

Since $a_i \neq 0$ solving **Equation 3.12** consists of finding the *N* unknowns ($H_{ki} - ES_{ki}$) for the *N* equations, leading to the secular equation:

$$\begin{vmatrix} H_{11} - ES_{11} & H_{12} - ES_{12} & \cdots & H_{1N} - ES_{1N} \\ H_{21} - ES_{21} & H_{22} - ES_{22} & \cdots & H_{2N} - ES_{2N} \\ \vdots & \vdots & \ddots & \vdots \\ H_{N1} - ES_{N1} & H_{N2} - ES_{N2} & \cdots & H_{NN} - ES_{NN} \end{vmatrix} = 0 \qquad \textbf{Equation 3.13}$$

To determine all coefficients a_i for all ϕ_j in the ground state one must:

- determine all H_{ij} and S_{ij}, using semi-empirical approximation or explicit calculation
- calculate all the roots of **Equation 3.13** which correspond to *N* different values of E_j (i.e. a different value for each MO)
- solve **Equation 3.12** for each MO to determine all a_{ij}

Finally ϕ_j can be obtained using **Equation 3.7**.

This method, used in Hückel Molecular Orbital theory (HMO), is very successful in predicating properties of unsaturated molecules such as aromatic compounds. In HMO theory H_{ij} is taken as the negative of the average ionization potential of the electron in the corresponding valence orbital, the basis functions used for S_{ij} are that of 2p orbitals and *N* = number of carbon atoms. This is a semi-empirical method where all core electrons are ignored and where the orbital overlap between adjacent atoms is taken equal to zero. The π electron repulsions are somewhat included in an average way by the use of experimental quantities such as ionization potential. Yet crude, HMO was found quite effective in qualitative studies of planar unsaturated compounds.[8,9]

In an effort to extend Hückel MO theory to molecules other than planar hydrocarbons, Hoffmann proposed his Extended Hückel Molecular Orbital theory.[10] EHMO differs from HMO by:

- larger basis set: four AOs (one 2s and three 2p) per carbon atom, instead of one AO (2p) in HMO, and one AO (1s) per hydrogen atom
- AOs are Slater Type Orbital (STO) wavefunctions
- overlap integrals, S_{ij}, between AOs are explicitly calculated
- resonance integrals, H_{ij}, are adjustable parameters accounting for partial atomic charge

Nevertheless, the approximation that core electrons are not affected by the atom environment still holds in EHMO theory and core electrons remain excluded from the calculations. Also, semi-empirical parameterization of H_{ij} and the lack of consideration for electron spin do limit EHMO in its applications.

EHMO is used today for its ability to provide a fast qualitatively correct MOs description of unsaturated and saturated organic and inorganic molecules. The speed allows for the calculation of large assemblies such as organic polymers. However, as pointed out by Gimarc, "the real value of EHMO is not in its quantitative results (…) but rather in the qualitative nature of the results and in the interpretations those results can provide".[11]. With the generalization of high performance computers, the time consumption argument does not hold against the use of more rigorous methods such as *ab initio* and DFT, described below. Yet, it was observed, for the systems investigated in this thesis (i.e. metallocenes and metal arenes, see **Chapters 6-8**), that EHMO was able to generate fast and reliable results while the use of *ab initio* and DFT presented limitations.

In order to account for many-electron effects, Hartree proposed to separate the Hamiltonian operator H (note that subscript "ele" is neglected from now on for clarity) into *N* one-electron operator h_i:

$$\mathrm{H} = \sum_{i=1}^{N} h_i \qquad \textbf{Equation 3.14}$$

where *N* is the number of electrons and one-electron operator h_i is defined by (in atomic units):

$$h_i = -\frac{1}{2}\nabla_i^2 - \sum_{k=1}^{M}\frac{Z_k}{r_{ik}} + V_i\{j\} \qquad \textbf{Equation 3.15}$$

with r_{ik} the distance between electron "*i*" and nucleus "*k*" and M the total number of nuclei. The many-electron wavefunction is then constructed from the product of all one-electron wavefunctions:

$$\Psi_{\mathrm{HP}} = \Psi_1 \Psi_2 \Psi_3 ... \Psi_{\mathrm{N}} \qquad \textbf{Equation 3.16}$$

where HP subscript means Hartree product. The last term in the right hand side of **Equation 3.15** accounts for the interaction potential between electron "*i*" and all other electrons "*j*" and is defined by:

$$V_i\{j\} = \sum_{i \neq j}\int \frac{\rho_j}{r_{ij}} d\mathrm{r} \qquad \textbf{Equation 3.17}$$

with ρ_j, the charge density of electron j, is defined by: $\rho_j = |\psi_j|^2$ **Equation 3.18**

Since the primary objective is to calculate the one-electron wavefunctions (ψ_i) one must start by guessing a set of ψ in order to build h_i and then solve the Schrödinger equation from which a new set of ψ is obtained. This new set, which is supposedly more accurate than the guessed one, is used to determine a new h_i, and so forth until a satisfying convergence is achieved for the ψ_i. This approach termed Self-Consistent Field (SCF) method was proposed by D.R. Hartree.[12] The level of convergence is chosen arbitrarily in an attempt to conciliate accuracy and computational time. An important shortcoming of the Hartree SCF method is that it violates the Pauli principle as the electrons are not indistinguishable. To account for that, D.R. Hartree and V. Fock proposed to replace the Ψ_{HP} by Ψ_{SD}, where the product of wavefunctions is expressed as a determinant (SD subscript meaning Slater Determinant):

$$\Psi_{SD} = \frac{1}{\sqrt{N!}} \begin{vmatrix} \chi_1(1) & \chi_2(1) & \cdots & \chi_N(1) \\ \chi_1(2) & \chi_2(2) & \cdots & \chi_N(2) \\ \vdots & \vdots & \ddots & \vdots \\ \chi_1(N) & \chi_2(N) & \cdots & \chi_N(N) \end{vmatrix} \qquad \textbf{Equation 3.19}$$

where χ corresponds to the product of a spatial orbital with an electron spin eigen function; i.e. a spin-orbital. In the Hartree-Fock (HF) SCF method, all electrons are indistinguishable but also exchange effects associated with electron spin are now accounted for. Yet HF-SCF still suffers from an important shortcoming in its inability to account for electron correlation. The assumption that each electron sees the other electrons as an average field is not sufficient in describing all electron interactions as it neglects the correlated motion of electrons with each other. However, in the ideal case of infinite basis sets, HF-SCF energy may differs from "true" energy by only the correlation energy, defined as:

$$E_{true} = E_{HF\text{-}SCF} + E_{corr} \qquad \textbf{Equation 3.20}$$

and E_{corr} can be estimated using dedicated methods.

The implementation of HF-SCF in *ab initio* theory was found quite successful in improving the calculation of MO energies.

Unlike HMO and EHMO methods that are semiempirical, i.e.: combine theoretical parameters and experimental data, *ab initio* is a more rigorous approach where all parameters are explicitly calculated. However, for obvious reasons, an infinite basis set is not manageable and only a limited number of basis sets can be computed at the detriment of accuracy.

For *ab initio* calculations the following method is commonly used:

1) select a minimal set of STO (1s, 2s, 2p)
2) account for orbital contraction by adding appropriate STOs (3d)
3) account for orbital polarization by adding STOs with l+1 angular momentum quantum number; i.e.: polarize a "s" orbital (l = 0) by adding a "p" orbital (l = 1)

The final number of STOs may easily become very large and might dramatically increase computational time. Alternatively STO functions can be replaced by linear combinations of Gaussian Type Orbitals (GTO), more easily handled by computers:

$$\varphi_{(STO)} = \sum_{i=1}^{M} a_i \, \varphi_{(GTO)i} \qquad \textbf{Equation 3.21}$$

where M is the number of primitive GTOs used.

Ab initio approach to solve the Schrödinger equation for many-electron systems requires calculating the energy and wavefunction for every one-electron orbital which appears to be a very tedious task. A simpler approach has been suggested where the many-electron wavefunctions have been replaced by a single density function in order to construct the Hamiltonian operator H. The three operators in **Equation 3.4** (i.e.: T_{ele}, $V_{Nuc\text{-}ele}$ and $V_{ele\text{-}ele}$) can be described in a classical approach as a function of the density of electrons at a particular point in space r (ρ(r)), defined by:

$$\rho(\mathrm{r}) = N \int d\mathrm{r}_2 \int d\mathrm{r}_3 ... \int d\mathrm{r}_N \left|\psi(\mathrm{r}, \mathrm{r}_2, \mathrm{r}_3, ...\mathrm{r}_N)\right|^2 \qquad \textbf{Equation 3.22}$$

with N the total number of electrons. As ρ(r) is a function of spatial coordinates, the operators $T\rho(r)_{ele}$, $V\rho(r)_{Nuc\text{-}ele}$ and $V\rho(r)_{ele\text{-}ele}$ are named *density functionals* leading to the Density Functional Theory.

Through two successive theorems Hohenberg and Kohn were able to demonstrate that as ρ(r) determines H, which according to the Schrödinger equation determines ψ and eventually the energy (E), in other words:

$$E[\rho(r)] = T_{ele}[\rho(r)] + V_{Nuc\text{-}ele}[\rho(r)] + V_{ele\text{-}ele}[\rho(r)] + \Delta T[\rho(r)] + \Delta V_{ele\text{-}ele}[\rho(r)] \qquad \textbf{Equation 3.23}$$

The two terms at the end of **Equation 3.23** were added by Kohn and Sham and correspond to electron kinetic energy correction due to electron-electron interactions and correction for non-classical exchange and correlation energies. The one-electron Schrödinger equation can now be written:

$$h_i^{KS}\psi_i = \varepsilon_i\psi_i \qquad \textbf{Equation 3.24}$$

Where, as for HF, in order to calculate each ψ_i one must first construct h_i, then guess a starting set of ψ followed by successive iterations until the desired convergence is obtained. The immediate advantage of DFT over HMO, EHMO and *ab initio* is its ability to perform calculations with a high level of accuracy and a relatively low computational time cost. A great deal of DFT methods aims at enhancing the theory's performances and liability for various systems including organometallics.[13,14]

NEXAFS spectra presented in this dissertation have been assigned with the help of EHMO, *ab initio* or DFT computational methods, each implemented in a different program. The purpose of the following sections is to describe how simulated X-ray absorption spectra; i.e. calculations of the transition energies and intensities, are generated from these methods. The difficulty in simulating XAS spectra resides in how well the core hole relaxation effects are accounted for. As mentioned in **§1.2** the formation of a core hole upon X-ray absorption modifies the atomic core Coulomb potential and the MOs calculated for the ground state do not accurately describe the MOs in the core excited state. All three programs presented in the following sections were purposely selected as they are all optimized, using different approaches, to account for the core orbital half occupancy. The approaches used for each computational method are described.

The core excitation intensities are approximated by calculating the oscillator strength f_{os} , defined as:[1]

$$f_{os} = \frac{2}{m\hbar\omega}\left|\langle f|\varepsilon \cdot p|i\rangle\right|^2 \qquad \textbf{Equation 3.25}$$

where ω is the radiation frequency. Note that f_{os} is directly related to the absorption cross section, (Cf **§1.2**) according to:

$$\sigma_x = C\frac{df}{dE} \qquad \textbf{Equation 3.26}$$

where $C = 2\pi^2 e^2 \hbar / mc = 1.1\times10^2$ MbeV(Mb = megabarn). The oscillator strength is thus a calculated value of the probability of the transition from the initial $|i\rangle$ to the final $|f\rangle$ state.

3.2 Extended Hückel Molecular Orbital Theory Calculations

EHMO calculations have been performed to help interpret the Fe 2p NEXAFS spectra of organometallic compounds. Calculations were performed using the Computer Aided Composition of Atomic Orbitals (CACAO) program.[15]

EHMO calculations are used to explore the effects of covalent bonding in these species as they are well parameterized for organoiron species and have already been applied effectively to the calculation of metallocenes.[16-19] DFT calculations are also appropriate for organoiron compounds; however, our particular version of the DFT program could not perform these Fe 2p calculations at the time of this investigation.

As mentioned in Section 1.2, the formation of a core hole following the absorption of X-ray affects the energy of all orbitals, occupied and unoccupied. The equivalent ionic core virtual orbital model (EICVOM)[20] is used to account for electronic relaxation due to the presence of the core hole. In the EICVOM, the core excited atom is replaced by the atom with one greater nuclear charge (e.g. Z+1 approximation), and the molecule is given a +1 charge to correct the valence electron count.

The atomic propensity approximation is used to determine the intensity of the spectroscopic features.[21] According to Laporte electric-dipole selection rules, the most intense transitions (i.e.: allowed transitions) are those that satisfy a change in orbital angular momentum of $\Delta l = \pm 1$; i.e. for 2p core excitation only the transitions 2p → 3d and 2p → 4s are considered, where 3d and 4s orbitals are highly localized on the core excited atom (localized core hole approach). The atomic matrix elements in **Equation 3.25** are then $\langle 3d|\varepsilon \cdot p|2p\rangle$ and $\langle 4s|\varepsilon \cdot p|2p\rangle$, however since $\langle 3d|\varepsilon \cdot p|2p\rangle >> \langle 4s|\varepsilon \cdot p|2p\rangle$ transitions to 4s orbital are neglected. As mentioned in **§3.1** EHMO is a valence only method and the intensity of the highly localized core excited transitions are estimated by calculating the sum of the square of the LCAO coefficients of the 3d AOs that contribute to the unoccupied MO of interest; i.e. Σa_{ij}^2(3d, 4s). Simulated spectra were obtained by calculating a Gaussian line shape for each transition using the program SIMILE2.[22]

EHMO calculations were used to help interpret the Fe 2p NEXAFS spectra of ferrocene and metal arene complexes. These calculations demonstrated the importance of covalent bonding in the assignment of the NEXAFS spectra of such compounds. Significant substituent effects were observed in the spectra, which with the help of EHMO calculations were assigned to electron donating / withdrawing properties of the substituents on the ligands and π^* conjugation between unsaturated substituents and ligands. The experimental and theoretical results for this study are presented in **Chapters 6, 7** and **8**.

3.3 *Ab Initio*-IVO Calculations

Ab initio calculations have been performed to help interpret the C 1s, N1s, and O 1s NEXAFS spectra of amino acids and related species recorded for XNCD study as well as in the examination of the zwitterionic effect in the N 1s NEXAFS spectra of amino acids and related compounds. Calculations were performed using Kosugi's GSCF3 package, as it is highly optimized for the calculation of core-excited states.[23] This program is based on the Improved Virtual Orbital method (IVO) of Hunt and Goddard reviewed below,[24], where the presence of the core hole is explicitly accounted for in the Hartree Fock Hamiltonian. The calculations were performed using the high quality GTO extended basis set of Huzinaga *et al.*[25] A complete list of all basis sets and polarization functions used for these *ab initio* calculations is presented **Chapter 5**.

3.3.1 Improved Virtual Orbital

The *ab initio*-IVO calculations consist of 3 steps, where the MO wavefunctions are calculated for the molecule 1) in the ground state, 2) in ionized state and 3) in the core excited state.[24]

A core excited molecule (with N electrons) can be divided into an "active part" (i.e. the core hole and the excited optical electron) and a "passive part" (the other N-1 electrons). After ground state calculations (step 1) an electron is explicitly removed from a desired core orbital and the N-1 electrons are then allowed to relax in the potential of the core excited cation (step 2) where the core hole is prevented from being refilled. Afterwards the passive electron part is frozen and excited states are calculated (step 3) for all possible optical orbital occupancies, i.e. unoccupied Rydberg and valence orbitals.

The transition intensities are explicitly calculated according to **Equation 3.25**. Simulated spectra are generated from these calculations by using a Gaussian line shape for each calculated excitation, using the program SIMILE2.[22]

During the examination of the XNCD effects in amino acid solid films it appeared that a feature on the low energy side of the main resonance observed at the nitrogen K edge had been misinterpreted throughout the literature where the transition had been assigned to Nitrogen 1s $\rightarrow$ Rydberg transitions, mixed with states of $\sigma^*_{(N-H)}$ character. The dominant Rydberg character is reasonable for gas phase spectra; however we expect that Rydberg character will be quenched in condensed species.[26,27] Knowing the degree of Rydberg /

valence mixing may be very important in the assignment of NEXAFS spectra used for the highly sensitive measurement of XNCD. Therefore, to explore the Rydberg character of this resonance, advanced calculations were performed on model molecules using the Shielding-Refined Improved Virtual Orbital (SR-IVO) method described below.

3.3.2 Shielding-Refined Improved Virtual Orbital

The Rydberg or valence character can be inferred by examining the calculated orbital size and the energy difference between singlet and triplet core excited states (ΔE_{S-T}) for a particular transition. Rydberg orbitals generally have a larger radius than valence orbitals, e.g. greater than 3 Å in small molecules. The energy difference between the singlet and triplet core excited states, ΔE_{S-T}, is a reflection of the differences in electron-electron repulsion for electrons in Rydberg or valence optical orbitals. Generally, core excited states with $\Delta E_{S-T} >$ 0.05 eV are considered to have some valence character. This method has been used effectively to characterize the degree of Rydberg – valence mixing in the NEXAFS spectra of gaseous[28] and condensed alkanes.[27]

The IVO approximation has the potential for spurious Rydberg valence mixing[29,30] as the energy of Rydberg transitions are generally more accurately calculated than valence transitions. The (N-1) passive part provides a good description of the electronic environment for core $\rightarrow$ Rydberg transitions, as these transitions converge to the core-ionization threshold corresponding to the core-ionized (N-1)-electron cation. However, for core-to-valence transitions, the calculation of the passive (N-1) electron part does not account for the significant shielding by the excited electron in its valence optical orbital. As a result, the nucleus is overshielded and the calculated energy of valence transitions is shifted to higher energy. Therefore, Rydberg and valence core excited states will have a different systematic error and Rydberg-valence mixing will be anomalous.[30,31] We can correct for this shielding effect by recalculating the passive electron part with the core hole vacancy and the optical orbital occupancy. The more-accurately shielded passive electron part is used in subsequent IVO calculations. This process is repeated for each core excited state, with the shallower optical orbitals frozen. This SR-IVO method was used by Kosugi *et al*. to remove spurious Rydberg / valence mixing in the C 1s $\rightarrow \sigma^*_{C-F}$ transition.[29]

Ab initio SR-IVO calculations were used to help assign the N 1s NEXAFS spectra of amino acids and other model compounds. Systematic differences observed between the

zwitterionic and un-ionized form of amino acids were assigned to the difference in protonation of the amine groups (i.e.: $-NH_2$ vs. $-NH_3^+$), which leads to a change in the degree of Rydberg – valence mixing. The experimental and theoretical results for this study are presented in **Chapter 5**.

3.4 Density Functional Theory Calculations

DFT calculations have been performed to help interpret the C 1s NEXAFS spectra of metallocene and metal arene complexes. DFT has been used effectively and extensively to examine the geometric and electronic structure as well as bonding in organometallic and sandwich complexes.[32] The calculations were performed using the Stockholm-Berlin version 2.1 of deMon (StoBe2005, dated 12/9/2005).[33] This program is based on self-consistent solutions of the Kohn-Sham DFT. The NEXAFS calculations presented here were performed following the procedures of Wilks *et al.*[34] and relevant details on basis set and polarization functions used for these calculations may be found in Wilks thesis dissertation.[35]

The NEXAFS spectra are simulated by calculating the transition probabilities between half-occupied core hole and optical orbital optimized in the potential of this half-occupied core hole excited molecule. NEXAFS curves were obtained by Gaussian convolution of the stick spectra generated by StoBe.

DFT calculations were found to be very helpful in the interpretation of the C1s NEXAFS spectra of ferrocene and metal arene complexes and confirmed the importance of covalent bonding in these compounds. The experimental and theoretical results for this study are presented in **Chapters 6, 7** and **8**.

3.5 References

(1) Stohr, J. *NEXAFS Spectroscopy*; Springer-Verlag: Berlin, **1996**.

(2) Urquhart, S. G.; Hitchcock, A. P.; Leapman, R. D.; Priester, R. D.; Rightor, E. G. *Journal of Polymer Science: Part B: Polymer Physics* **1995**, *33*, 1593.

(3) Hitchcock, A. P.; Urquhart, S. G.; Rightor, E. G. *Journal of Physical Chemistry* **1992**, *96*, 8736.

(4) Pettersson, L. G. M.; Agren, H.; Schurmann, B. L.; Lippitz, A.; Unger, W. E. S. *International Journal of Quantum Chemistry* **1997**, *63*, 749.

(5) Cramer, C. J. *Essentials of Computational Chemistry. Theories and Models*, Second ed.; John Wiley & Sons: Chichester, **2004**.

(6) Levine, I. N. *Quantum Chemistry*, Fourth ed.; Prentice-Hall: Englewood Cliffs, **1991**.

(7) Lowe, J. P.; Peterson, K. A. *Quantum Chemistry*, Third ed.; Elsevier Academic Press: San Diego, **2005**.

(8) Coulson, C. A.; Streitwieser, A. *Dictionary of π-Electron Calculations*; Freeman: San Francisco, **1965**.

(9) Streitwieser, A.; Brauman, J. I. *Supplemental Tables of Molecular Orbital Calculations*; Pergamon Press: New York, **1965**.

(10) Hoffmann, R. *The Journal of Chemical Physics* **1963**, *39*, 1397.

(11) Gimarc, B. M. *Molecular Structure and Bonding: the qualitative molecular orbital approach*; Academic Press: New York, **1979**.

(12) Hartree, D. R. *Proceedings of the Cambridge Philosophical Society* **1928**, *24*, 89.

(13) Koch, W.; Holthausen, M. C. *A Chemist's Guide to density Functional Theory*, second ed.; WILEY-VCH: Weinheim, **2001**.

(14) Diedenhofen, M.; Wagener, T.; Frencking, G. The accuracy of Quantum Chemical Methods for the Calculation of Transition Metal Compounds. In *Computational Organometallic Chemistry*; Cundari, T. R., Ed.; Marcel Dekker, Inc.: New York, **2001**; pp 69.

(15) Mealli, C.; Proserpio, D. M. *Journal of Chemical Education* **1990**, *67*, 399.

(16) Ruhl, E.; Hitchcock, A. P. *Journal of the American Chemical Society* **1989**, *111*, 5069.

(17) Hitchcock, A. P.; Wen, A. T.; Ruhl, E. *Chemical Physics* **1990**, *147*, 51.

(18) Ruhl, E.; Wen, A. T.; Hitchcock, A. P. *Journal of Electron Spectroscopy and Related Phenomena* **1991**, *57*, 137.

(19) Wen, A. T.; Ruhl, E.; Hitchcock, A. P. *Organometallics* **1992**, *11*, 2559.

(20) Schwarz, W. H. E. *Chemical Physics* **1975**, *11*, 217.

(21) Ishii, I.; Hitchcock, A. P. *Journal of Chemical Physics* **1987**, *87*, 830.

(22) Huo, B.; Hitchcock, A. P. Simile2 Software, **1996**.

(23) Kosugi, N.; Kuroda, H. *Chemical Physics Letters* **1980**, *74*, 490.

(24) Hunt, W. J.; Goddard III, W. A. *Chemical Physics Letters* **1969**, *3*, 414.

(25) Huzinaga, S.; Andzelm, J.; Klobukowski, M.; Radzio-Andzelm, E.; Sakai, Y.; Tatewaki, H. *Gaussian Basis Sets for Molecular Calculations*; Elsevier, **1984**; Vol. 16.

(26) Robin, M. B. *Higher Excited States of Polyatomic Molecules*; Academic Press: Orlando, FL, **1985**; Vol. III.

(27) Urquhart, S. G.; Gillies, R. *Journal of Chemical Physics* **2006**, *124*, 234704.

(28) Urquhart, S. G.; Gillies, R. *Journal of Physical Chemistry A* **2005**, *109*, 2151.

(29) Kosugi, N.; Ueda, K.; Shimizu, Y.; Chiba, H.; Okunishi, M.; Ohmori, K.; Sato, K.; Shigemasa, E. *Chem. Phys. Lett.* **1995**, *246*, 475.

(30) Kosugi, N. *"Advanced Course in Application of GSCF3 to Inner Shell Excitation"* **2000**.

(31) Kosugi, N. *"Manual of GSCF3"* **1986**.

(32) Cundari, T. R. *Computational Organometallic Chemistry*; Marcel Dekker, Inc: New York, **2001**.

(33) Hermann, K.; Petterson, L. G. M.; Casida, M. E.; Daul, C.; Goursot, A.; Koester, A.; Proynov, E.; St-Amant, A.; Salahub, D. R.; Contributing authors: Carravetta, V.; Duarte, H.; Friedrich, C.; Godbout, N.; Guan, J.; Jamorski, C.; Leboeuf, M.; Leetmaa, M.; Nyberg, M.; Pedocchi, L.; Sim, F.; Triguero, L.; Vela, A. StoBe Software, StoBe-DeMon Version 2.1**, 2005**.

(34) Wilks, R. G.; MacNaughton, J. B.; Kraatz, H. B.; Regier, T.; Moewes, A. *Journal of Physical Chemistry B* **2006**, *110*, 5955.

(35) Wilks, R. G. Experimental and theoretical investigation of the electronic structures of ferrocene-peptide conjugates, University of Saskatchewan, **2005**.

CHAPTER 4 X-RAY NATURAL CIRCULAR DICHROISM

Circular dichroism is the difference in absorption of circular polarized light by chiral molecules and assemblies. This effect is measured almost exclusively using infrared (IR), visible and UV wavelengths but can be expected at any wavelength. IR and UV absorption are respectively related to vibrational and valence electronic excitation while X-ray absorption corresponds to core electron excitation. A discussion on the importance of chirality in chemistry is presented in §**4.1**. The objective of this study was to observe CD at X-ray wavelength for small organic chiral molecules; these motivations are further explained in §**4.1.1**.

This controversial experiment has been greatly anticipated by theory. The difficulties associated with the theoretical description of the effect and the constrains associated with the experimental technique have been assessed and are described in §**4.1.2.1** and §**4.1.2.2**. The various approaches established to address these challenges are then presented §**4.1.2.3**.

The samples investigated are listed §**4.2** along with the reasons why these compounds have been selected. The experiments are described in §**4.3** and their outcomes are presented and discussed in §**4.4**. While great progress has been made in the selection of samples, the preparation methods and in optimizing spectroscopic techniques, XNCD was not observed. The last section (§**4.5**) is a reflection onto why none of the attempts to measure XNCD were fruitful and suggestions for further investigation are presented.

4.1 Introduction

4.1.1 Chirality and Circular Dichroism

Chirality is defined by the International Union of Pure and Applied Chemistry as the "geometric property of a rigid object of being non-superimposable on its mirror image" or for an atom "to hold a set of ligands in a spatial arrangement which is not superimposable on its mirror image" (Both from IUPAC Compendium of Chemical terminology, 2nd edition 1997). Our hands are a familiar example of chiral objects and amino acids are examples of chiral molecules (see **Figures 4.1)**. Chirality in chemistry is not limited to the second definition, which implies the presence of a chiral atom in the molecule, or stereogenic center, such as the tertiary carbon atom in the amino acid example. Molecules as a whole can be chiral objects as

can molecular assemblies such as monolayers, carbon nanotubes and polymer films with suprastructural chirality. The relevance of these examples from the fields of chemistry, biology, surface chemistry and material chemistry shows the extent of chirality in science.

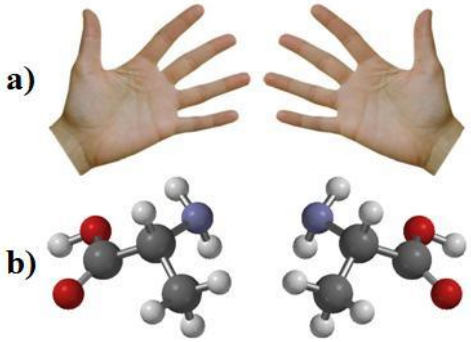

Figure 4.1 a) Chiral objects: left and right hands are mirror images but not superimposable. b) Chiral moleclues: alanine.

The most prevalent optical methods used in laboratories to assess chirality are optical rotatory dispersion (ORD) and circular dichroism. ORD is related to the ability of a chiral substance to rotate the plane of polarization of linear polarized light. In **Chapter 1** linear polarized light was presented as the resultant of two linear polarized waves propagating in the same direction and oscillating in phase in two orthogonal planes. Yet plane polarized radiation may also be described as the resultant of left and right circularly polarized radiation of equal intensity and propagating in phase in the same direction. The rotation of the plane of polarization by a chiral substance is then due to a difference in refractive indexes for LCP and RCP radiations. The consequence is a shift in the phases of the two radiations that causes the plane of polarization of the resulting plane-polarized wave to tilt by an angle θ (**Figure 4.2**).

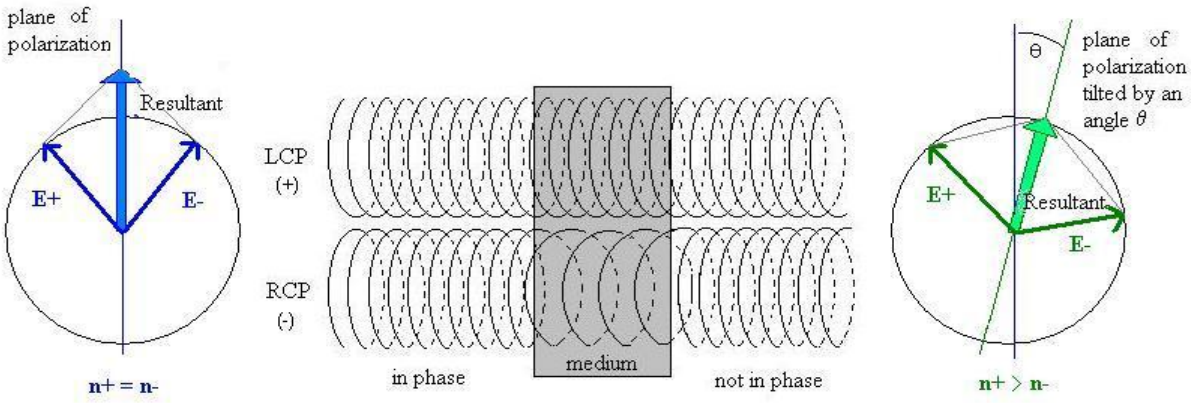

Figure 4.2 Schematic representation of the plane polarized light rotation by chiral substance.

Two non-superimposable mirror images of a molecule are termed enantiomers and are referred to as dextrorotatory (+) for the enantiomer responsible for rotating plane-polarized light clockwise and levorotatory (-) for the enantiomer responsible for rotating plane-polarized light counterclockwise. This asset of ORD is extensively used to help determine enantiomeric ratio in mixtures. Enantiomeric purity is a critical concept in many disciplines such as organic chemistry, biology and pharmacology as enantiomers are involved in drastically different mechanisms. Specific rotation, an intrinsic property of the pure enantiomer, is then determined by measuring the angle θ of rotation of the plane of polarization of the radiation at a specific wavelength, concentration and temperature.

CD is related to the ability of a chiral substance to change linearly polarized light into elliptically polarized light. Selective absorption of LCP or RCP radiation by a chiral substance affects the intensity ratio between the two radiations. This causes the resulting electric vector to rotate around the propagation axis instead of oscillating in the plane of polarization, as described in **Figure 4.3** (where no change in refractive index is assumed). CD spectroscopy is used routinely in laboratories to characterize secondary and tertiary structures of large molecules such as polymers, proteins and nucleic acids.

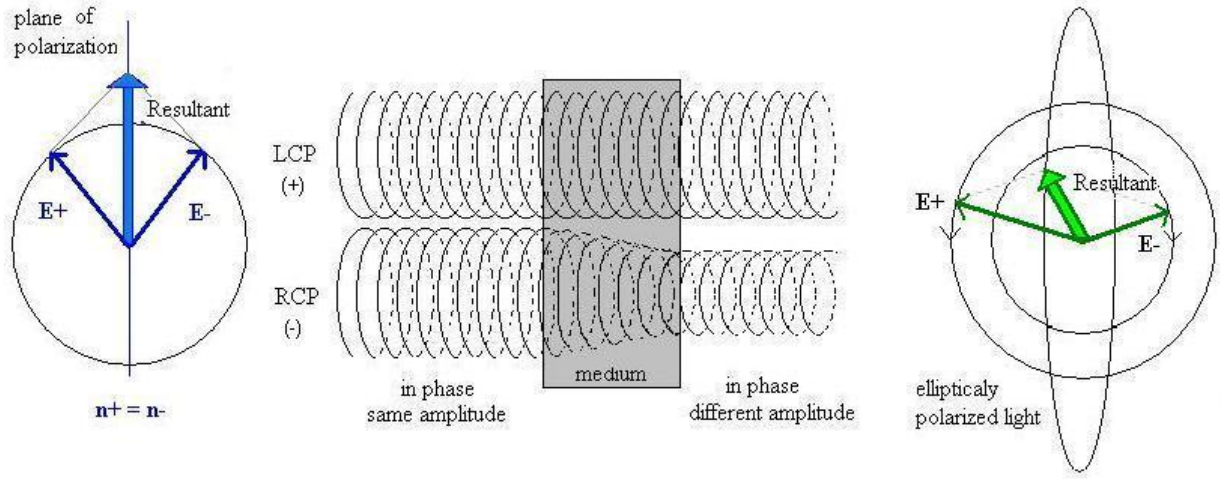

Figure 4.3 Schematic representation of the elliptical polarization of linear polarized light by a chiral substance.

Note that ORD and CD do not lead directly to absolute configuration of the molecules investigated and are most often used in an empirical way. The measurement of enantiomeric excess by ORD requires knowing specific rotations of the pure enantiomers while CD spectroscopy is habitually used as a fingerprint method. Additionally both ORD and CD performed in solution are strongly dependent on the solvent or the buffer systems used, the

temperature are often limited by competitive absorption processes from the medium and surrounding (i.e. oxygen).

NEXAFS spectroscopy is an element specific tool highly sensitive to the chemical and structural environment as well as magnetic properties of the atoms being investigated. Dichroism associated with the absorption of circularly polarized X-rays has been observed for a series of inorganic compounds, and for very few organic materials. The objective of the research presented below is to measure CD at X-ray wavelengths from small organic chiral molecules in solid and liquid phases.

The exact nature of the interaction of circular polarized light with matter is still a very fascinating topic as the long lasting question of homochirality in terrestrial life remains unresolved. It has been suggested that uneven distribution of the circular polarized radiation in daylight may have influenced the enantiomeric selectivity of biomolecules.[1] Investigation of the interaction of circular polarized X-rays with molecules such as α-amino acids might contribute to a better understanding of this phenomenon.

For chemists the primary interest in the difficult measurement of XNCD is in its potential application in resolving enantiomers. Unlike traditional methods, i.e. ORD, UV-CD, IR-CD and chiral-sensitive atomic force microscopy, NEXAFS spectroscopy is suitable for samples in gas, liquid and solid state allowing CD measurement for a broader range of samples including thin films and monolayers.

Also theoretical studies have indicated that large XNCD effects are expected in chiral molecules for atoms other than the stereogenic center.[2] If this excited state chirality effect was observed experimentally it would provide additional confirmation that chirality is a molecular property and that the description of stereogenic centers is not limited to a "chiral atom". This could perhaps leads to examination of XNCD for chiral molecules containing no chiral atom, such as polycyclic aromatic compounds like heptahelicene.

Additionally, an important number of theoretical studies have been dedicated to XNCD in organic chiral molecules. Yet very limited experiments have been successful so far in recording the timid effect and their agreements with the computed simulations are rather poor. A greater collection of experimental results would then contribute improving the computational tools used to simulate polarization and non-dipole effects in NEXAFS spectroscopy.

4.1.2 XNCD of Small Chiral Organic Molecules

4.1.2.1 Theoretical constrains

The anisotropic absorption of circular polarized light by a chiral substance is due to coupling of the electric transition dipole (E_1) of the EM radiation to the magnetic transition dipole (M_1) or the electric transition quadrupole (E_2) in the expression of the X-ray absorption cross section (see **equation 1.5**). At UV wavelengths, processes arising from the $E_1 \cdot M_1$ cross term governs the measured circular dichroism for unoriented samples, as the $E_1 \cdot E_2$ cross term vanishes.[3] At X-ray wavelengths, CD measurements and calculations indicate that the $E_1 \cdot E_2$ cross term is responsible for the anisotropic absorption by core level electrons of circular polarized X-rays while the contribution of $E_1.M_1$ cross term is controversial and considered by some as insignificant. However the number of crystal classes which are expected to exhibit significant $XNCD_{E1E2}$ is quite limited[4] prohibiting examination of all compounds relevant to our field of interest, i.e.: small organic chiral molecules. Therefore to measure CD from such compounds one has to look for the notorious $XNCD_{E1M1}$ effect.

The atomic selection rules for allowed electric quadruple transitions (E_2) are:

- change in orbital angular momentum $\Delta\ell = 0, \pm 2$ with $\Delta\ell \neq 0$ if $\ell_0 = 0$

The atomic selection rules for allowed magnetic dipole transitions (M_1) are:

- $\Delta\ell = 0$ and $\ell_0 \neq 0$
- no change in principal quantum number, $\Delta n = 0$

The much more restrictive selection rules that apply to M_1 partly explain why the $E_1 \cdot M_1$ cross terms show limited to no contribution to XNCD, especially for transitions originating from K electron shells ($\ell_0 = 0$).[5] No magnetic dipole transition is allowed from perfectly spherical orbitals ($\ell_0 \neq 0$) and all transitions from deep core shells such as K, L_1 and M_1 are forbidden due to $\Delta n = 0$. Yet relaxation of these selections rules, i.e. 1s-2p orbital mixing, have been observed and, as discussed in **§4.1.2.3**, weak XNCD signal have been recorded and assigned with the help of theoretical calculations.

4.1.2.2 Experimental constrains

The g-factor defined in **Equation 1.9** for small organic molecules such as amino acids had been calculated and was predicated to range between 10^{-4} to 10^{-3}.[2,6,7] One of the main difficulties in measuring such a small signal reside in the magnitude of the uncertainties

associated with X-ray intensity and polarization variability, mainly due to the decay in beam intensity and the spatial instability of the beam during measurements.

Additionally when studying organic materials with X-rays, one must be concerned by the risk of sample damage induced by radiation. The sensitivity and mechanism of X-ray damage have been extensively investigated for systems similar to the one of interest in this thesis; i.e. amino acid, peptides, organic and organometallic polymers.[8-17]

Due to the weakness of the signal associated with XNCD any small variations in the spectra due to beam instability, normalization or X-ray sample damage would jeopardize the reliability of the measurement.

4.1.2.3 Our Approaches

As established in **§ 4.1.2.1**, the measurement of CD from small chiral organic molecules will be restricted to the $E_1 \cdot M_1$ mechanism. In order to rule out any possible contribution from $E_1 \cdot E_2$ interactions it was determined that only amorphous samples would be examined as $E_1 \cdot E_2$ cross terms are expected to cancel out for non-oriented samples (amorphous, powder, liquid, gas etc..).[3] This prerequisite has been our primordial concern through all the sample preparations and great efforts have been put toward achieving randomly oriented samples.

Regarding the selection rules, on account of their relaxation, several theoretical studies concerned with $E_1 \cdot M_1$ interferences have reported g-factor values in the range of 10^{-8} at sulfur K edge for unoriented molecules of H_2S_2[5] up to 10^{-3} for carbon, nitrogen and oxygen K edges of small organic molecules and amino acids where 1s-2p orbital mixing was accounted for using the CD effect[2,18]. Recent measurements at carbon K edge of gas phase methyloxirane led to g-factors on the order of 10^{-3}, in agreement with earlier calculations.[18,19] The authors ascribed the origin of this rather large XNCD signal to an effective hybridization of 1s-2p orbitals due to their relative proximity in carbon atoms. Based on these studies it was determined that measurement of very weak $XNCD_{E1M1}$ effect was indeed possible for organic compounds and that tremendous progress made in the field of synchrotron polarized soft X-rays would compensate for the weakness of the intended measurement.

Yet, as mentioned in **§ 4.1.2.2,** beam instability over the time it takes to acquire NEXAFS spectra is indeed of great concern. To address this issue, we proposed to simultaneously record the spectra of both enantiomers, the racemic mixture for control and

the substrate for normalization using one circular polarized radiation at a time (either LCP or RCP). The expression of the g-factor presented in **Equation 1.9** is equivalent to:

$$g = 2 \times \frac{\sigma_L - \sigma_D}{\sigma_L + \sigma_D} \qquad \textbf{Equation 4.1}$$

where σ_L and σ_D are the absorption cross sections measured with either LCP or RCP light for L- and D- amino acid. NEXAFS spectra from four different regions can be acquired simultaneously using soft X-ray spectromicroscopy (SM). The field of view of these microscopes ranges from several micrometers up to several hundred micrometers. The sample is then required to combine both enantiomers, a racemic area and a normalization area in micrometer domains size. Such small scale patterned samples can be prepared by chemical vapor deposition, details on this methods will be presented in **§ 4.3.1.1**.

X-ray SM is also a great tool to investigate X-ray sensitive materials, such as biological samples, as it is highly efficient in controlling the radiation dose the samples are exposed to.

In order to reduce the effects of X-ray damage, the amount of photons the sample is exposed to needs to be reduced. By reducing the photon flux the measurements become more prone to beam instability and background noise and to compensate for this one must increase the number of data points recorded. When using X-ray spectroscopy techniques this is done by averaging many low dose spectra, which can be time consuming. In X-ray SM the spectra are generated by averaging the number of transmitted photons over an image where every pixel is as many data points (see **§2.2.2**). Spectra with relatively low shot noise (i.e.: random fluctuation in measurement over a long period of time; enhanced at low photon flux) can then be obtained in reasonably short exposure time. Great efforts have been made to ensure that the effects of X-ray radiation were kept as low as feasible. X-ray damage studies were conducted for several samples following the method established by Coffey *et al*.[13]

Table 4.1 summarizes the various difficulties identified in this section and associated with the measurement of $XNCD_{E1M1}$ along with how these issues are intended to be addressed.

Constrains:	Our approaches:
Theoretical - $XNCD_{E1E2} > XNCD_{E1M1}$ - very weak $XNCD_{E1M1}$ effect	- randomly oriented sample - enantiomerically pure samples
Experimental - beam instability causing intensity and polarization inconsistencies - X-ray damage	- both enantiomers examined simultaneously using X-ray SM (requires patterned sample films) - determine radiation dose limits and diminish sample exposure using X-ray SM

Table 4.1 Constrains and approaches in the measurement of $XNCD_{E1M1}$ of small organic chiral

4.2 XNCD Samples

Beside the prerequisite to study randomly oriented structures, such as liquid and amorphous solids, further restrictions associated with either sample preparation methods or technique limitations were identified. These restrictions, which are listed in **Table 4.2**, were used to optimize the selection of compounds suitable for $XNCD_{E1M1}$ measurement.

In order to attempt $XNCD_{E1M1}$ measurements, three classes of compounds were selected according to the restrictions presented in **Table 4.1** and will be described in greater detail below.

Limitations associated with:	Sample requirements:
$XNCD_{E1M1}$	- randomly oriented - high purity - both enantiomers available enantiomerically pure (or very high enantiomeric excess)
NEXAFS spectroscopy	- with few non equivalent atoms to simplify spectrum - with low sensitivity to X-ray
NEXAFS measurements	- stable in air, non toxic - with low vapour pressure for measurements in ultra high vacuum conditions
Sample preparation vacuum deposition: liquid cell:	- stable in air, non toxic - low vapour pressure - suitable for sublimation - soluble in common solvent (or suitable for neat solution)

Table 4.2 List of requirements to satisfy to select samples for XNCD experiment.

4.2.1 Amino Acids and Amino Acid Derivatives

Amino acids are organic molecules that contain an amine group ($-NH_2$) and a carboxylic acid group (-COOH). Alpha-amino acids (general formula $H_2N\text{-}C^{\alpha}RR'\text{-}COOH$) have both amino and carboxylate groups bonded to the same tetravalent carbon atom (C^{α}) and are chiral for all side groups (-R) ≠ (-R'). The properties of α-amino acids vary widely with the identity of the side groups. More than 500 α-amino acids have been found in nature and 20 in the human body where they play a crucial role as the building blocks of proteins. Amino acid enantiomers are distinguished by the labels L and D (small capital letters). These labels refer to the optical activity of the L-Glyceraldehyde and D-Glyceraldehyde which contain an asymmetric carbon atom with the same S (sinister) and R (rectus) configuration as the amino acid. The labels R and S correspond to the absolute notation created by Cahn, Ingold and Prelog where the subsituents on the chiral atom are prioritized by decreasing

atomic number; OH > COH (aldehyde) > CH_2OH and NH_2 > COOH > $CH_2(CH_3)_2$ > CH_3 as in the examples presented **Figure 4.4**.[20] Two amino acids may then have the same S/R and L/D labels yet a different optical activity (+) or (-) (see **Figure 4.4**).

Amino acids were considered as very promising candidates for $XNCD_{E1M1}$ measurements as they fulfil all requirements presented in **Table 4.2**, and because they have been the subject of extensive experimental and theoretical studies, including NEXAFS spectroscopy and XNCD calculations.

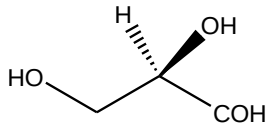

D-Glyceraldehyde
(+)-Glyceraldehyde
(R)-Glyceraldehyde

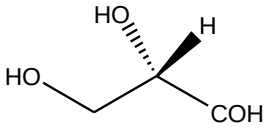

L-Glyceraldehyde
(-)-Glyceraldehyde
(S)-Glyceraldehyde

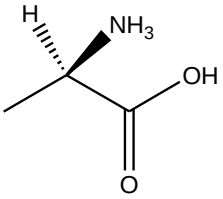

D-Alanine
(-)-Alanine
(R)-Alanine

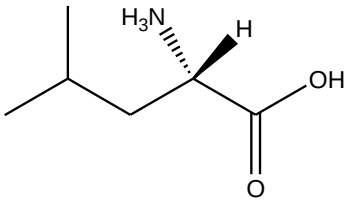

L-Leucine
(-)-Leucine
(S)-Leucine

Figure 4.4 Examples of configuration label assignment using L/D, (+)/(-), R/S and L/D notations.

Three chiral amino acids have been selected, alanine, phenylalanine and serine and one achiral amino acid, glycine. Glycine was used as a control since no XNCD effect is expected from achiral compounds. Amino acids in solid state exist as dipolar ions or zwitterions (H_3N^+-C^{α}RR'-COO^-) and show a high propensity to form oriented structures under standard conditions of pressure and temperature. In order to avoid presence of zwitterions and prevent formation of crystalline structures, methyl ester hydrochloride derivatives of alanine and serine have also been investigated. Amorphous films of poly[(N-propenoyl) L-alanine benzyl ester] and poly[(N-propenoyl) D-alanine benzyl ester], i.e. polymer with alkane chain and amino acid derivative pendent groups, have been prepared and examined. The molecular structures of all amino acids and derivatives are presented in **Figure 4.5.**

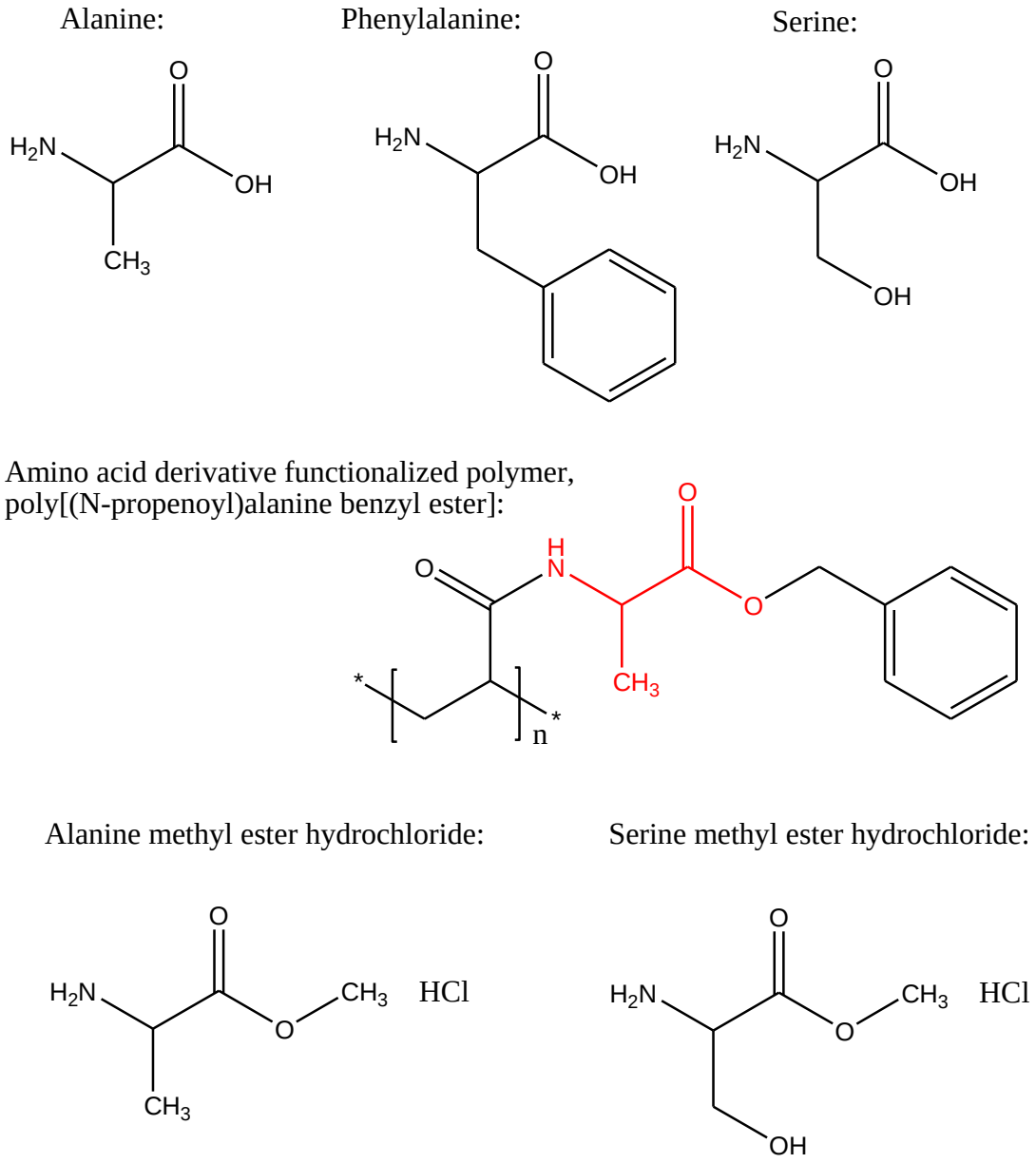

Figure 4.5 Chemical structure of amino acids and derivatives.

Specific details on preparation of thin films of α-amino acids, α-amino acid derivatives and poly[(N-propenoyl)alanine benzyl ester], referred to as amino acid derivatives functionalized polymer, are presented in the following section.

4.2.2 Small Chiral Organic Molecules

In additional to α-amino acids and derivatives, five small organic molecules have been selected: tartaric acid, α-hydroxy-γ-butyrolactone, 3-butyn-2-ol, 3-hydroxytetrahydrofuran and styrene oxide. (see **Figure 4.6** for molecular structures).

Unlike amino acids and tartaric acid, the last four compounds are in liquid state at normal conditions of temperature and pressure, thus intrinsically disordered. For liquid samples, liquid cells had to be prepared; further details on sample preparation are presented in a following section.

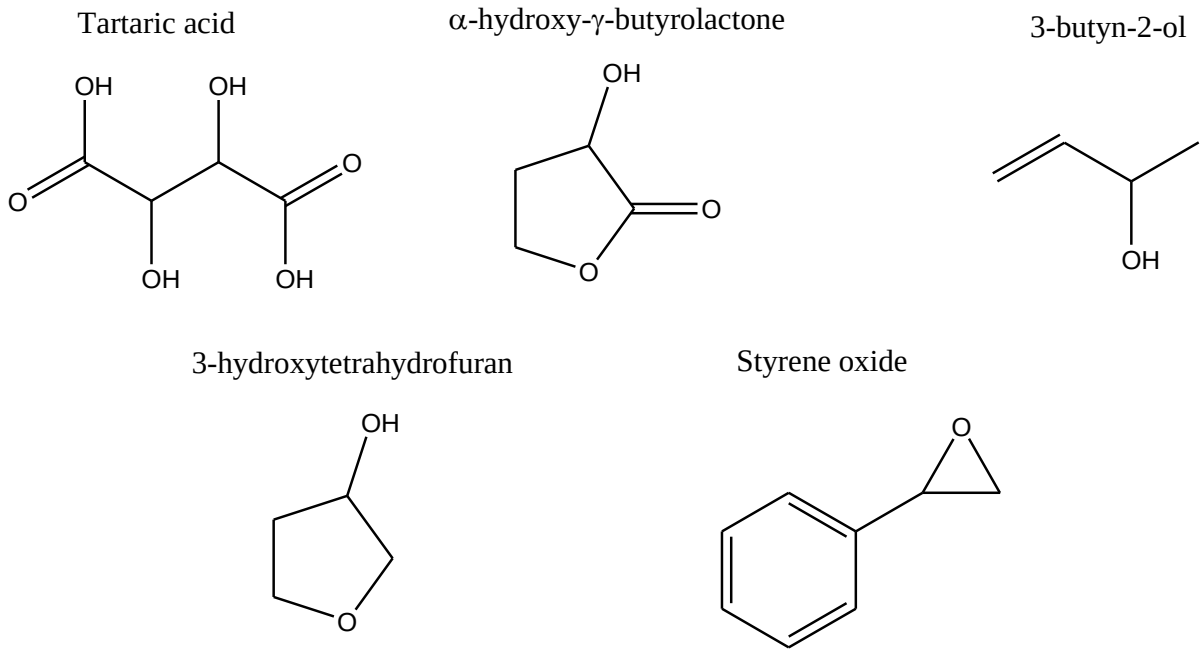

Figure 4.6 Chemical structure of small chiral organic molecules.

4.2.3 Heptahelicene

Carbohelicenes are polycyclic aromatic molecules containing only carbon atoms in their skeleton and with a unique helical structure, as shown in **Figure 4.7**.[21]

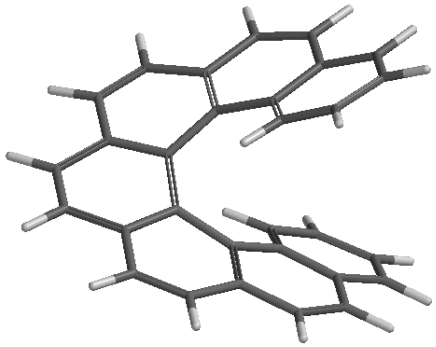

Figure 4.7 Representation of the structure of heptahelicene.[22]

Helicity, engendered by the repulsion between the facing benzene rings confers to the molecule its chirality. The two enantiomers are distinguishable by the sense of rotation of the helix; right-hand helix corresponding to (P)- (plus or (+)) configuration and left-hand helix to (M)- (minus or (-)) as illustrated in **Figure 4.8**.[23]

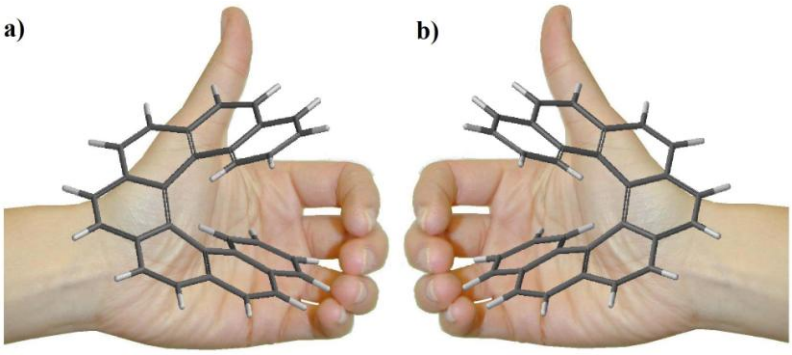

Figure 4.8 Heptahelicene a) left-hand helix (M) or (-) and b) right-hand helix (P) or (+).

The high chemical and configuration stability of helicenes account for their extensive applications in molecular recognition, enantioselective catalysis and molecular electronic and photonic devices.[24]

Heptahelicene ([7]H, $C_{30}H_{18}$) was selected for the XNCD study. The details on the sample preparation are presented in the following section.

4.3 Experiments

4.3.1 Sample Preparation

4.3.1.1 Thin film deposition of amino acids and amino acid derivatives

4.3.1.1.1 Chemical vapour deposition

Chemical vapor deposition was used to prepare patterned films of amino acids using the thermal deposition instrument (Datacomp Scientific) presented in **Figure 4.9-a**.

The following compounds were obtained commercially and used without further purification: L-alanine, D-alanine, L-phenylalanine, D-phenylalanine, L-serine, D-serine, L-alanine methyl ester hydrochloride, D-alanine methyl ester hydrochloride, L-serine methyl ester hydrochloride and D-serine methyl ester hydrochloride. Milligram amounts of compound is placed in a resistively heated tungsten receptacle located inside a high vacuum chamber represented schematically in **Figure 4.9-b**.

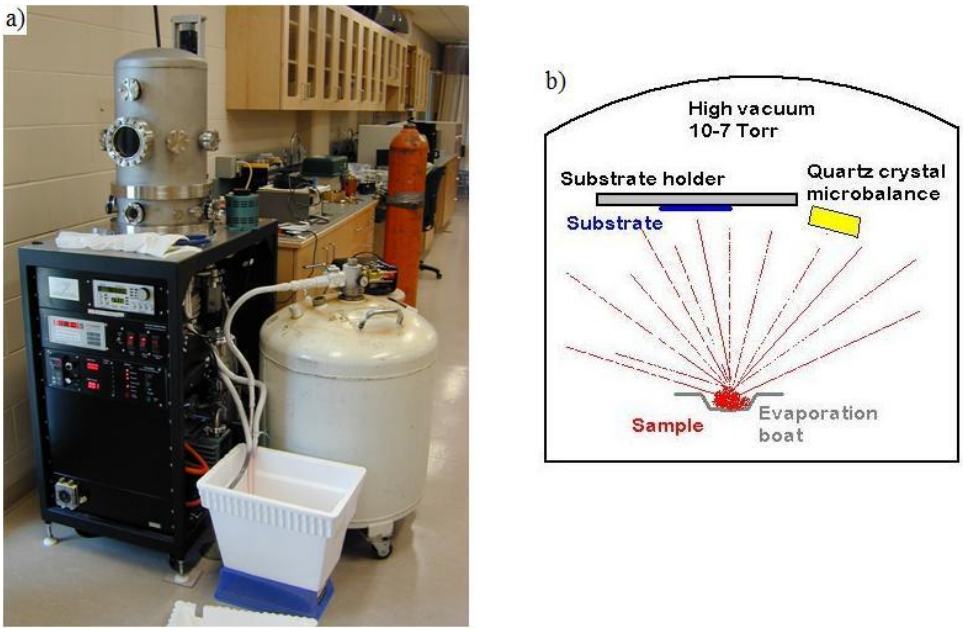

Figure 4.9 Thermal deposition instrument (Datacomp Scientific). a) Picture showing the setup used for deposition on cold substrate: liquid nitrogen tank connected by a feedthrough to substrate holder located inside the deposition chamber. b) schematic of the inside of the deposition chamber.

The temperature of the receptacle is increased by augmenting the amount of current travelling through the receptacle until the temperature of sublimation of the compound is achieved. The molecules then travel to the surface of the substrate, either silicon wafers (N-type, P doped, orientation (100), 1-10 Ω/cm resistivity) or silicon nitride membrane windows (Si_3N_4; 75 nm and 100 nm thickness), located 15cm above the receptacle. The thickness of the film accumulated on the surface of the substrate is monitored by a quartz crystal microbalance located in the vicinity of the substrate.

The two enantiomers were deposited consecutively using a mask in order to alternate areas covered with each enantiomer and areas uncovered (open area) used for normalization. **Figure 4.10-a,b,c** show the various mask shapes used: V-shape, fork-like shape and transmission electron microscope (TEM) copper grid (Structure Probe Inc.).

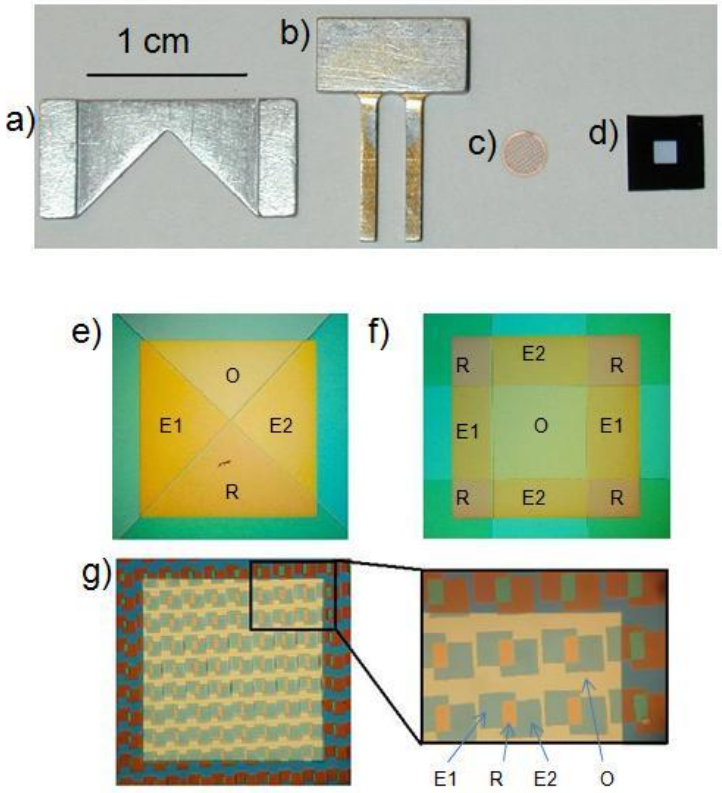

Figure 4.10 Masks used to prepare patterned samples, a) V-shape, b) fork shape and c) TEM copper grid and d) Si_3N_4 membrane window. Microscope images of patterned films prepared with e) V-shape mask, f) fork mask and g) TEM copper grid on Si_3N_4 membrane (1.5 mm by 1.5 mm). E1 = enantiomer 1; E2 = enantiomer 2; R = racemic; O = open area.

Both V-shape and fork-shape masks have been designed specifically for this application and were custom made by the University of Saskatchewan Physics Machine Shop. Optimum sample quality was achieved using TEM copper grid masks. The evenness of the grids enabled the mask to be positioned at approximately 2 μm from the Si_3N_4 membrane. Their thickness prevented shadowing effects responsible for the irregularities observed at the edge of the films deposited using thicker V-shape and fork-shape masks. Additionally, as illustrated in **Figure 4.10-f,** a larger number of domains could be deposited on one membrane using TEM copper grid masks, enhancing sample preparation time, domain steadiness and x-ray microscope experimental time.

Thin film of L- and D- alanine, L- and D- phenylalanine and L- and D-serine were prepared successfully by CVD. However, for L- and D- alanine and serine methyl ester hydrochloride, after deposition the films had rearranged into large structured domains and an alternative method, solution casting, was used (see § **4.3.1.2**).

4.3.1.1.2 Chemical vapour deposition: cold substrate

Almost any substance can exist in an amorphous state providing that the molten material can be cooled down rapidly enough to prevent the more thermodynamically stable crystalline phase from forming.[25] As will be discussed in § **4.4.1.1**, amino acid films prepared by CVD appeared to contain oriented structures which prevent $XNCD_{E1M1}$ measurements to be performed, as the $XNCD_{E1E2}$ will dominate. To further attempt to grow amorphous films, a series of serine samples were prepared by CVD on cold substrates. The substrate, a Si_3N_4 membrane window, was mounted onto a large copper holder maintained at a temperature of -170ºC throughout the deposition using a continuous flow of liquid nitrogen. Following the deposition, the serine films were brought back to room temperature while kept under vacuum (10^{-7} Torr). The first series of films were examined by optical microscopy immediately after the samples were removed from the vacuum chamber. No indication of crystalline phases was found until several minutes after the samples were exposed to air. Optical microscope images recorded consecutively during the crystallization process of a serine film are presented in **Figure 4.11**.This experiment was duplicated several times and all corroborated our initial observations that crystalline structures appear several minutes after the film is exposed to air.

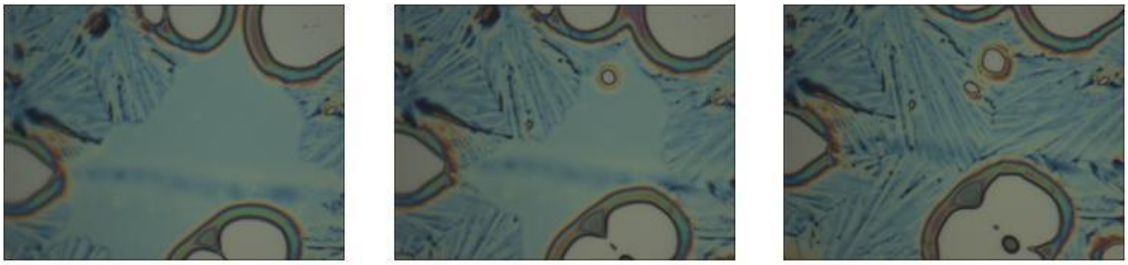

Figure 4.11 Progression of the crystallization process in serine film deposited by CVD on cold substrate (Si_3N_4) captured by optical microscope; image size 7 μm by 5 μm.

It is believed that at room temperature the moisture in air contributes to the nucleation process leading to formation of crystalline domains in the films. An additional series of samples were prepared and stored immediately after deposition in moisture free containers waiting for NEXAFS measurements. Results from these samples will be discussed below.

CVD is a highly efficient technique in terms of versatility and film reproducibility and purity. However, very few small organic molecules possess adequate melting point, vapor pressure and thermal stability required for CVD, thus less ideal preparation methods had to be utilized to prepare amorphous samples suitable for XNCD experiments.

4.3.1.1.3 Spin cast

Spin casting is an alternative method for thin film deposition which allows control over the film thickness. This method was successfully used to prepare amorphous thin films of polymers with amino acid derivative pendent groups synthesized by Travis Besanger, a former member of the research group of Dr. S.G. Urquhart (see **Figure 4.5**).

Milligram amounts of the polymers were dissolved in dichloromethane and transferred drop wise onto a spinning substrate. The best results in terms of film homogeneity and thickness reproducibility were obtained using potassium chloride (KCl) coated silicon wafers as substrates; with KCl coating performed by CVD. The thickness of the film depends on the solution concentration, the rate of evaporation of the solvent and the speed of rotation of the substrate. For the sample to be measured in transmission mode, the polymer films were transferred onto TEM copper grids by dissolving the KCl layer into deionized water (Millipore water purification system, resistivity 18MΩ.cm). A schematic summarizing the method used for film transfer is presented in **Figure 4.12**. Separated samples were prepared for each enantiomer.

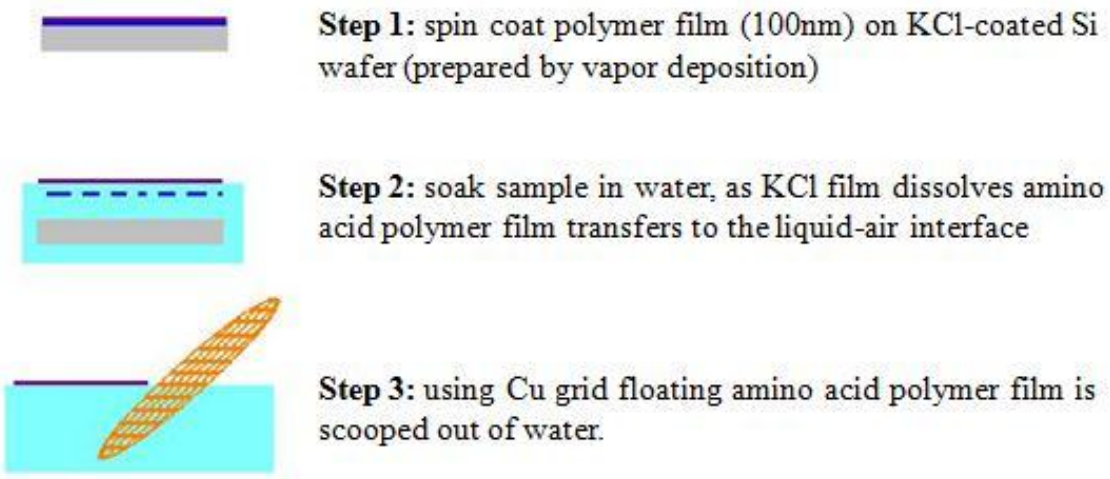

Figure 4.12 Schematic representation of polymer film transfer from KCl coated Si wafer to TEM copper grid.

4.3.1.2 Solution cast

Solution casting allows limited control over sample thickness and lacks reproducibility.However, it can be very effective for compounds that are suitable neither for CVD nor spin casting or that are only available in very small amounts as was the case for [7]H.

The following compounds were obtained commercially and used without further purification: L-alanine methyl ester hydrochloride, D-alanine methyl ester hydrochloride, L-serine methyl ester hydrochloride and D-serine methyl ester hydrochloride. Both (P)- and (M)-heptahelicene were synthesized by I. Stary according to published procedures.[26] Milligram amounts of the compounds were dissolved in appropriate solvent (water for the amino acid derivatives and dichloromethane for [7]H) and transferred drop wise onto Si_3N_4 membrane windows or SiO coated copper grids. The evaporation of the solvent can be increased by gently heating the substrate with a hot plate. As for the samples that were prepared by spin casting, the enantiomers were cast on separated substrates.

4.3.1.3 Solution cast – melt and quench

As mentioned above, an amorphous state may be reached upon rapid transition from liquid to solid state. As will be described in § **4.3.3**, solution cast films of [7]H appeared to contained oriented structures. Series of [7]H solution cast samples were placed into the cylinder of a melting tool designed specifically for this purpose (see **Figure 4.13)**. The cylinder was placed inside a Dewar flask at several centimetres above liquid nitrogen to maintain a low oxygen concentration throughout the experiment. The melting temperature of [7]H was estimated by differential scanning calorimetry measurements to be 281ºC. As the temperature inside the cylinder reached 281ºC, the sample was immerged into liquid nitrogen.

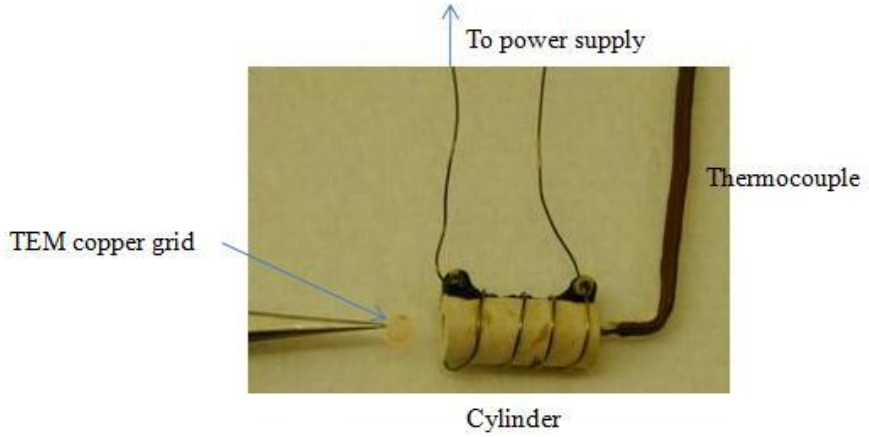

Figure 4.13 Picture of the melting tool used to prepare [7]H films by melt and quench method.

4.3.1.4 Wet cell

Wet cells are convenient when investigating biological samples in liquid medium. Yet preparation, handling and measurement is much less straightforward than for the previously described methods and can be very time consuming and wasteful of expensive Si_3N_4 windows. Also, the method offers poor control of sample thickness.

The following compounds were obtained commercially and used without further purification: L-serine, D-serine, L-(+)-tartaric acid, (R)-(+)-α-hydroxy-γ-butyrolactone, (S)-(-)-3-butyn-2-ol, (R)-(-)-3-hydroxytetrahydrofuran and (S)-(-)-styrene oxide.

For solid samples (serine and tartaric acid) milligram amounts of compound were dissolved in water. Then microliters of solution or neat solution were deposited onto a Si_3N_4 membrane window with the help of a micropipette. A second window was then placed on top in order to trap the liquid sample between the two transparent Si_3N_4 membranes. The cell was sealed using silicon rubber around the edges of the silicon frames.

4.3.2 Measurements

All samples were measured in transmission mode using STXMs located at beam-lines 5.3.2 and 11.0.2 at the ALS. Beam-line 5.3.2 is equipped with a bending magnet that provides horizontal linearly polarized radiation and was used for testing sample viability and presence of crystalline structure. Beam-line 11.0.2 is equipped with an elliptically polarized undulator, which provides linear and circular polarized light and was used mainly for XNCD measurements. Both beam-lines are described in detail in §**2.3.2**.

4.3.2.1 Normalization

At C 1s, N 1s and O 1s edges, the spectra were normalized using the following equation:

$$\text{Normalized spectrum} = \frac{[I]}{[I_0]} \qquad \textbf{Equation 4.2}$$

where [I] corresponds to the intensity of the beam after travelling through the sample and the substrate (Si_3N_4), while [I_0] correspond to the intensity of the beam after travelling through the substrate (Si_3N_4) only. For patterned films, the sample area and substrate area (open area) are present in the same field of view and allow for both [I] and [I_0] to be recorded simultaneously. For polymer films on TEM copper grids [I] and [I_0] were also recorded simultaneously using empty squares as open areas. For solution casted samples on Si_3N_4

membrane windows or SiO coated copper grids and liquid cells, [I_0] was recorded separately using a blank Si_3N_4 membrane window or SiO coated copper grid. This last method assumes that the source of X-ray radiation is stable over the time of the experiments and is referred to as stable beam method.[27] However, beam decay and beam instability over time will occur and uncertainties might be introduced to the normalized spectra, challenging the measurement of the very weak g-factor.

4.3.2.2 Energy Scale Calibration

The energy scale at C 1s edge was calibrated relative to the absorption spectrum of CO_2 gas, characterized at 292.74 eV and 294.96 eV by two strong absorptions assigned to transitions to 3s(ν=0) and 3p(ν=0) respectively.[27] At N 1s edge the energy scale was calibrated relative to the spectrum of N_2 gas, characterized at 406.15 eV and 407.12 eV by two absorption peaks assigned to transitions to 3s(ν=0) and 3p(ν=0) respectively.[28] And at O 1s edge the energy scale was calibrated relative to the spectrum of CO_2 gas, characterized by a strong absorption observed at 535.4 eV and assigned to transition to $2\pi_u$.[29]

4.4 Results and Discussion

4.4.1 Amino Acid and Derivatives

4.4.1.1 Patterned films of amino acids

Patterned films of alanine, phenylalanine and serine deposited on Si_3N_4 membrane windows by CVD were examined by optical microscopy and atomic force microscopy. The presence of topographic irregularities at the surface of the films was perceived, but no evidence of crystalline phase was found explicitly. On the other hand, STXM images indicated the presence of ordered structures. **Figure 4.14** shows two images recorded at 532.15 eV with linear horizontal (**a**) and vertical (**b**) polarized light.

The contrast observed between the two images is due to anisotropic absorption of the EM radiation by domains where the carboxylic groups (COOH) have different orientations. The O 1s NEXAFS spectra of serine presented in **Figure 4.15** were recorded over the same area using linear vertical (solid line) and horizontal (discontinuous line) polarized light.

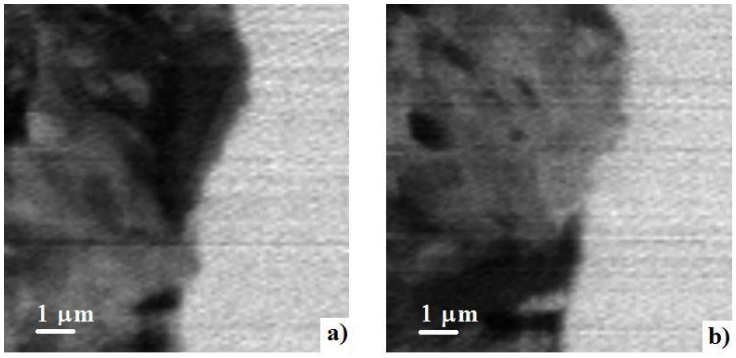

Figure 4.14 STXM images of serine film recorded at 532.15 eV with a) horizontal polarized light and b) vertical polarized light.

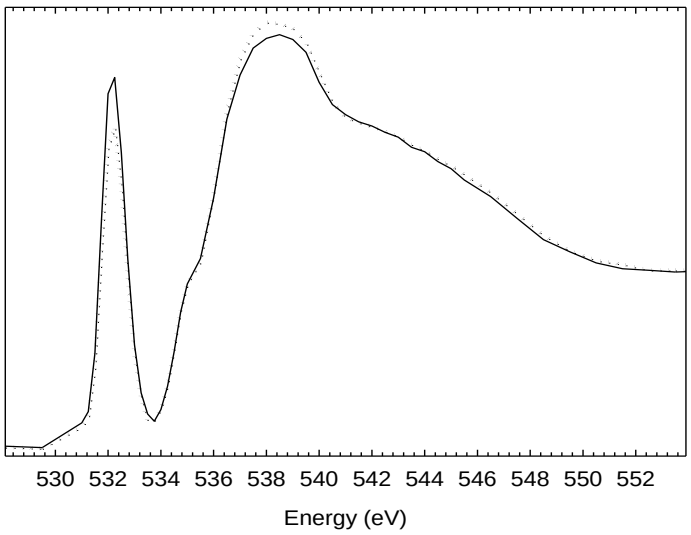

Figure 4.15 O 1s NEXAFS spectra of serine recorded with vertical polarized light (solid line) and horizontal polarized light (dotted line).

According to spectral assignments reported in literature, the features observed at 532.15 eV corresponds to the transition O 1s → $\pi^*_{(C=O)}$ while features observed above 536.00 eV are assigned to O 1s → σ*.[2,30,31] The variations in intensity observed between the two spectra are associated with linear dichroism and indicates the presence of crystalline structure in these films. The same conclusion was reached from similar studies with alanine and phenylalanine films at C 1s and O 1s edges.

In solid state, strong hydrogen bondings between ($-COO^-$) and ($-NH_3^+$) are responsible for the stabilization of the zwitterionic form of the amino acids, they are also involved in promoting the formation of the crystalline phase.. From the results presented above, it appears that at room temperature alanine, phenylalanine and serine in sublimed film on Si_3N_4

membranes can rearrange and form more favourable crystalline phases. In order to prepare un-oriented samples alternative approaches have been explored:

- CVD on cold substrate to reduce the energy available for the molecules to rearrange during the deposition.
- Amino acids in solution
- Amino acid derivatives which do not form zwitterions, specifically amino acid methyl ester hydrochlorides.

The outcomes of these approaches are presented in the following sections.

4.4.1.2 Patterned film of amino acid deposited on cold substrate

A series of serine patterned films were prepared by CVD on Si_3N_4 membrane maintained at -170ºC throughout the deposition. The samples were then stored for several days in moisture free containers under standard conditions of temperature and pressure. STXM images collected from these samples indicated the presence of large and very well structured domains as demonstrated in **Figure 4.16**. The contrast observed between the different domains is associated with linear dichroism and implies the presence of crystal structures in the film. These observations suggest that either the moisture level was not sufficiently low or that other factors took part in the formation of the crystal structures in the amino acid films. Additionally, it was found that upon film rearrangement, the stress imparted onto Si_3N_4 membranes was sufficient to break the membrane leading to high sample casualty rate. The preparation of amorphous thin films of amino acids by chemical vapour deposition on cold substrate was not pursued further.

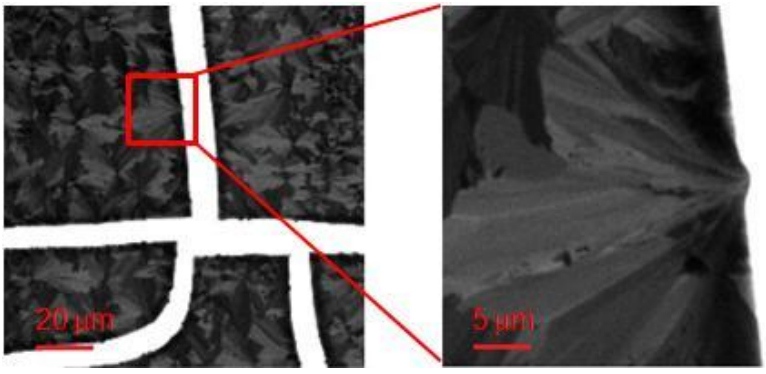

Figure 4.16 STXM images of serine film recorded at 289.00 eV with horizontal polarized light.

4.4.1.3 Amino acid wet cell

It was found that most cells containing initially aqueous solutions of serine were dry at the time of measurement. For the few successful samples, STXM images showed the presence in the cells of several micrometer sized areas of sample accumulation (see **Figure 4.17**). C 1s NEXAFS study indicated the presence of serine in these aggregates; however, low spectra reproducibility and high noise level obviated any search for crystallinity in these samples. NEXAFS study at the O 1s edge was found impractical due to the presence of uneven amounts of water over the cells.

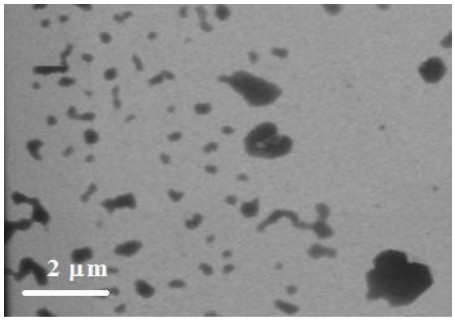

Figure 4.17 STXM images recorded at 289.00 eV of serine wet cell showing presence of aggregates.

4.4.1.4 Amino acid derivatives

Samples of L- and D-alanine and serine methyl ester hydrochloride prepared by solution casting were examined by STXM and appeared to contain crystalline structures.
In addition no sample-free area was available for normalization purposes and external normalization was required. This method of normalization is less desirable because, as mentioned in **§4.3.2.1**, it might introduce uncertainty in the XNCD measurement.

In all amino acids and amino acid derivatives, no evidence of sample orientation was observed at N 1s edge; however, significant differences were noticed between N 1s NEXAFS spectra recorded from our solid films and those reported in the literature.[15,32-40] Amino acids exist in various charge states depending if they are in solid phase (zwitterionic i.e.: H_3N^+-$C^{\alpha}RR'$-COO^-), in gas phase (neutral i.e.: H_2N-$C^{\alpha}RR'$-COOH) or in solution (pH dependent). We believed that the inconsistencies observed at the N 1s edge were associated with changes in the first coordination shell of the nitrogen atoms (-NH_2 versus –NH_3^+). To verify our presumption, the spectra of solution cast samples of glycine, glycine hydrochloride, glycine sodium salt, poly(allylamine) and poly(allylamine hydrochloride) were recorded at C 1s, N 1s and O 1s edges (see **Figure 4.18** for drawing of the chemical structures).

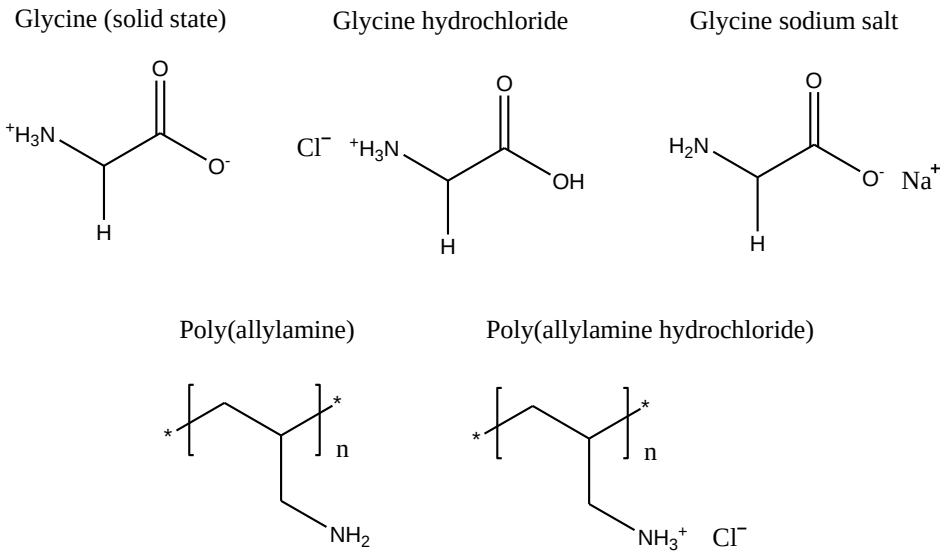

Figure 4.18 Chemical structure of glycine, glycine derivatives and poly(allylamine).

The presence of linear dichroism at C 1s and O 1s edges prevented any systematic spectral changes associated with protonation or deprotonation of the amine and carboxylic groups to be perceived. However, at the N 1s edge, a low energy shoulder was observed systematically for compounds containing unprotonated amine group ($-NH_2$) (**Figure 4.19**).

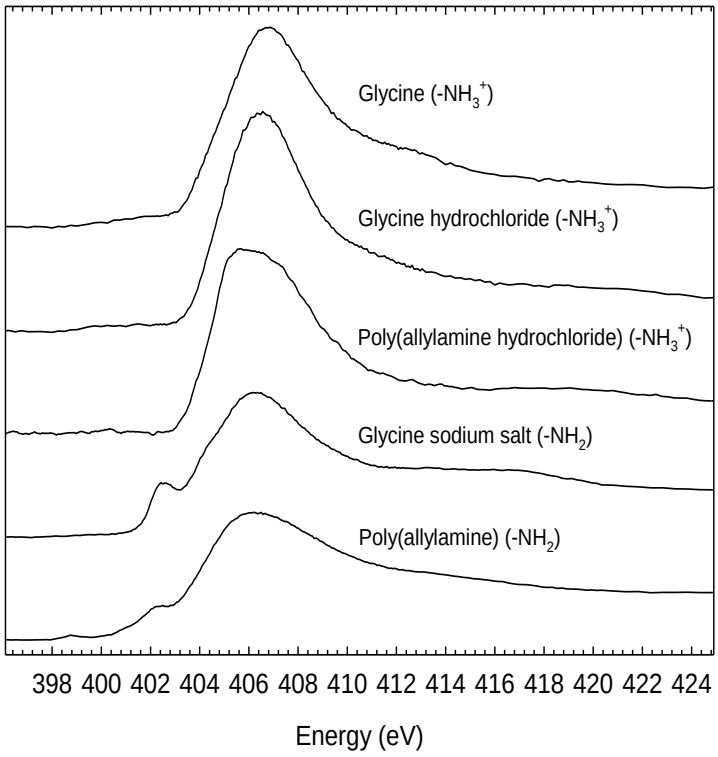

Figure 4.19 Nitrogen 1s NEXAFS spectra of glycine, glycine derivatives and poly(allylamine) polymers. The spectra have been offset by a constant for clarity.

With the help of *ab initio* calculations using Kosugi´s GSCF3 package described in §3.2 this shoulder was assigned to N 1s → $\sigma^*_{(N-H)}$ and N 1s → $3p_z$ out-of-plane Rydberg transitions, unique to unprotonated amines ($-NH_2$). This is reported as a separate manuscript in **chapter 5**. The ability to resolve such spectral changes is crucial for the use of amino acids as model compounds in highly sensitive $XNCD_{E1M1}$ experiments. Similar effects associated with amino acid charged states are expected at C 1s and O 1s edges but would require crystal-free samples to be unambiguously characterized.

4.4.1.5 Amino acid derivative functionalized polymer films

The preparation of amino acid derivative functionalized polymer films by spin casting a solution in dichloromethane resulted in a highly efficient method in terms of film homogeneity, thickness control and reproducibility. **Figure 4.20** presents optical microscope (**a**) and x-ray (**b**) images of the polymer films.

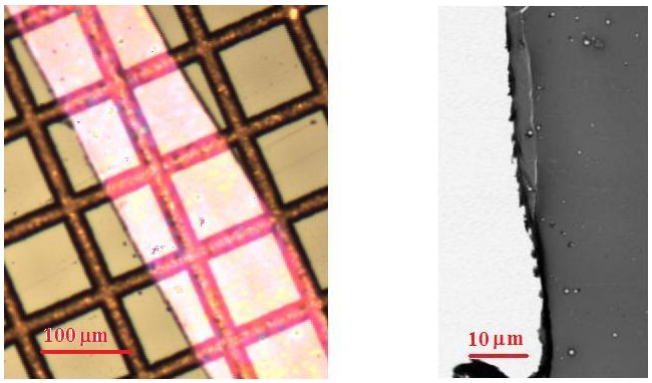

Figure 4.20 Optical microscope (a) and STXM (b) images of poly[(N-propenoyl)alanine benzyl ester]polymer films.

Uniformity of the color in image (**a**) indicates constant film thickness and the evenness of grey shade in image (**b**) indicates constant sample density over the area scanned. No evidence of linear dichroism at C 1s, N 1s and O 1s edges was detected from X-ray images or NEXAFS spectra. Absence of linear dichroism in these films indicates that amorphous samples of amino acid derivative functionalized polymers were successfully prepared. **Figure 4.21-a** shows O 1s NEXAFS spectra recorded with RCP light from two different films of poly[(N-propenoyl)D-alanine benzyl ester].

Low level of noise and high spectral reproducibility is imputed to the high quality of the samples. The difference between the two spectra is presented in **Figure 4.21-b**.

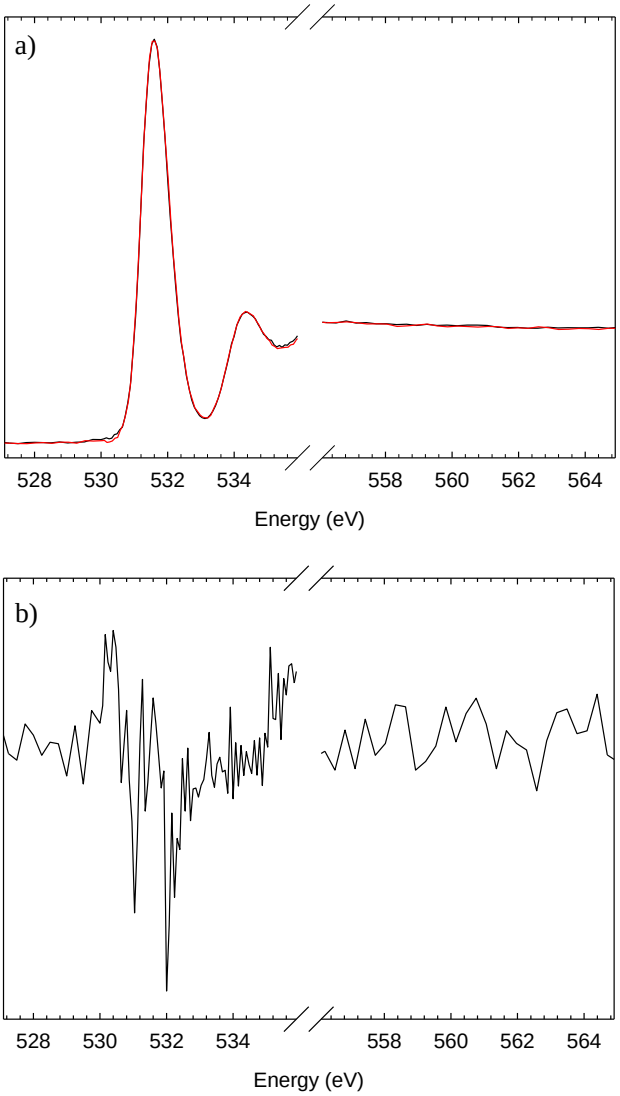

Figure 4.21 a) O 1s NEXAFS spectra of poly[(N-propenoyl)D-alanine benzyl ester] derivative functionalized polymer films recorded with RCP light from two different sample areas; b) difference between these two spectra.

Figure 4.22-a presents O 1s NEXAFS spectra of poly[(N-propenoyl)L-alanine benzyl ester] (black) and poly[(N-propenoyl)D-alanine benzyl ester] (red) polymers recorded using RCP light and the difference poly[(N-propenoyl)L-alanine benzyl ester] – poly[(N-propenoyl)D-alanine benzyl ester] is shown in **Figure 4.22-b**, the black curve. The magnitude of the discrepancies observed in **Figure 4.22-b** are up to 6 times larger than the discrepancies observed in **Figure 4.21-b**, which suggests that they might have different origins. The second curve presented in **Figure 4.22-b** corresponds to the difference between O 1s NEXAFS spectra of L- and D-amino acid polymers recorded using LCP light, the red curve. The curves show similar trends; however, according to XNCD theory they are

expected to be mirror images. This infers that the origins of the spectral discrepancies are not related to circular dichroism. Considering the quality of the samples, we impugn these results to erratic behaviour of the instrument affecting spectral reproducibility, normalization and higher order contamination.

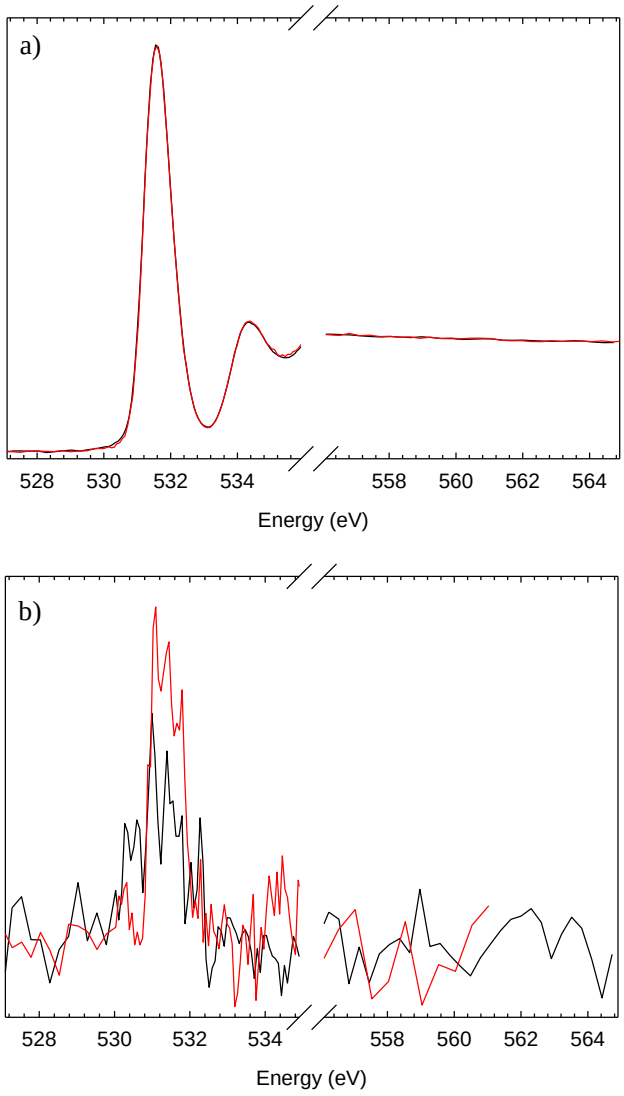

Figure 4.22 a) O 1s NEXAFS spectra of poly[(N-propenoyl)L-alanine benzyl ester] (black) and poly[(N-propenoyl)D-alanine benzyl ester] (red) derivative functionalized polymer films recorded with RCP light; b) difference between these two spectra (black) and between poly[(N-propenoyl)L-alanine benzyl ester] and poly[(N-propenoyl)D-alanine benzyl ester]acid derivative functionalized polymer films recorded with LCP (red).

4.4.2 Small Chiral Organic Molecules in Wet Cells

The examination of tartaric acid wet cell samples led to similar observations as serine wet cells. STXM images indicated the presence of aggregates containing tartaric acid. C 1s NEXAFS spectra collected from these aggregates were found to be highly irreproducible, yet

no evidence of orientation in the samples was found. The presence of water in the cell prevented collection of any reliable O 1s spectra.

NEXAFS spectra recorded from a series of wet cells prepared from liquid samples (R)-(+)-α-hydroxy-γ-butyrolactone, (S)-(-)-3-butyn-2-ol, (R)-(-)-3-hydroxytetrahydrofuran and (S)-(-)-styrene oxide were found to be unreliable. Inconsistent amounts of solution over the cells as well as the use of stable beam method (normalization with external Si_3N_4 spectra) led to minor but significant variations in peak intensity which would compromise XNCD measurements. The study of (R)-(+)-α-hydroxy-γ-butyrolactone at the O 1s edge showed strong spectral changes with sample thickness. **Figure 4.23** exhibits a series of O1s NEXAFS spectra recorded from different locations of the same (R)-(+)-α-hydroxy-γ-butyrolactone wet cell.

It has been suggested that the variations in intensity of the features observed below 533 eV were associated with linear dichroism indicating the presence of liquid crystals in the cell. While no definite explanation was found to account for these changes, minor effects observed for other wet cell systems were significant enough to justify not pursuing the use of wet cells for XNCD experiments.

In the view of these unfruitful results it was determined that wet cells were inappropriate for XNCD measurements and led to no further experiments.

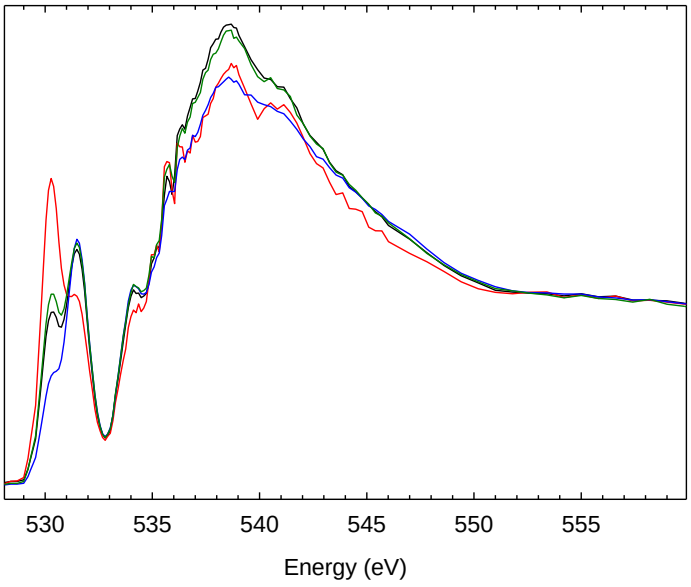

Figure 4.23 O 1s NEXAFS spectra of (R)-(+)-a-hydroxy-g-butyrolactone recorded from different locations of wet cell sample.

4.4.3 Hepathelicene

Heptahelicene samples prepared by solution casting were examined at the C 1s edge with linear polarized light and appeared to contain structured domains. **Figure 4.24** shows two spectra recorded over the same area with horizontal (black) and vertical (red) linear polarized light.

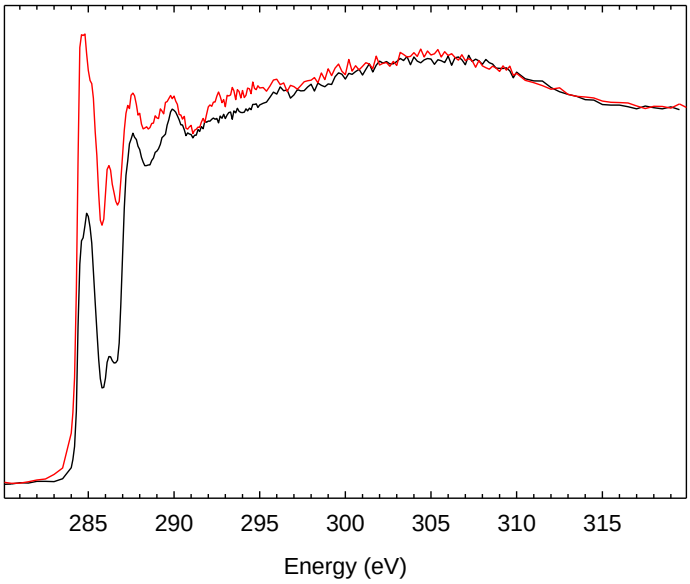

Figure 4.24 C 1s NEXAFS spectra of [7]H recorded with linear horizontal (black) and vertical (red) polarized light.

The variations in intensity of the features observed below 290.5 eV and assigned to C 1s → π* transitions are larger than the features observed above 290.5 eV and assigned to C 1s → σ* transitions.[41,42] Study of [7]H monolayer by NEXAFS at the C 1s edge indicated a similar trend for spectra recorded at normal and grazing incidences.[42] These results suggest the presence of crystalline domains in the sample prepared by solution casting and led to a second preparation method based on fast cooling of the melted sample. **Figure 4.25** presents C 1s NEXAFS spectra of [7]H recorded from samples prepared by solution casting (black) and solution casting followed by one melt/quench cycle (red).

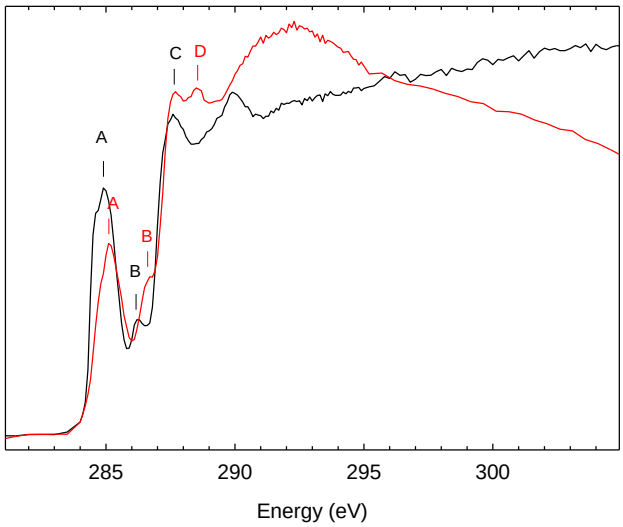

Figure 4.25 C 1s NEXAFS spectra of [7]H recorded from samples prepared by solution cast (black) and solution cast followed by one melt/quench cycle (red).

Significant inconsistencies are observed between the two spectra; specifically a decrease in intensity of feature **A**, a shift from higher energy of feature **B** and the presence of a new feature at 288.5 eV (**D**). These results indicate the presence of different species in the melt/quench sample than in the solution cast sample. The presence of a peak at 288.5 eV suggests the presence of organic compounds containing carbonyl functional groups,[43] which could originate from oxidation of [7]-H during the melting process. These concerns regarding the purity and the possible alteration of [7]-H molecule prevented us from performing any further measurements toward XNCD on the melt/quench samples.

4.5 Conclusion

The measurement of organic molecules XNCD associated with the electric dipole-magnetic dipole mechanism ($E_1 \cdot M_1$) requires randomly oriented samples and has been observed for methyloxirane molecules in gas phase.[19] In condensed phase, the preparation of amorphous samples adequate for XNCD measurement was found to be very challenging. The various approaches followed to prepare thin amorphous films of organic compounds led to the recurrent issue of molecules' propensity to form crystalline assemblies. Small organic molecules identified as good candidates for XNCD measurement must remain in solid phase at low vacuum, which requires a certain degree of coherence among the molecules which is believed to be correlated with sample crystallinity.

While investigating the sample preparation for $XNCD_{E1M1}$ measurement K. Kazumichi *et al.* published a study on XNCD of sublimated amino acid films in which they reported a difference in absorption between LCP and RCP light at the N 1s edge as large as $2x10^{-1}$ for alanine films.[44,45] The authors were able to simultaneously record NEXAFS spectra with left and right circular polarized light with a switching frequency between LCP and RCP of 2 Hertz and 0.1 Hertz. Such a procedure is expected to be very efficient in preventing X-ray polarization variability associated with beam decay and beam instability throughout the measurements. The authors addressed the issue of X-ray damage by scanning a different sample area at each energy and aimed to reduce statistical noise by averaging four to eight spectra for each sample. On the other hand, the authors did not address the critical question of sample crystallinity which as demonstrated in § **4.3.1.1,** is a concern in sublimated amino acid films. No information on a linear dichroism study of amino acid films has been reported. Additionally, the authors were able to observed XNCD for alanine and phenylamine films at the N 1s edge and serine films at the O 1s edge but did not mention any experiment on alanine or phenylalanine at C 1s or O 1s edges or on serine at C 1s or N 1s edges. Also, the authors mentioned that the theoretical calculation performed by Plashkevych *et al.* reproduced partially their experimental results.[2,46] The theoretical calculations predict strong XNCD signals for alanine and phenylalanine at 404.0 eV and 404.5 eV respectively and for serine at 533.44 eV. The experimental XNCD curves reported by K. Kazumichi *et al.* show maximum/minimum for alanine at 406.0 eV, 407.5 eV and 410.3 eV, for phenylalanine at 402.5 eV and 407.0 eV and for serine at 532.5 eV, 536.0 eV, 540.0 eV and 548 eV (see **Figure 4.26**). Finally, to our knowledge, these results have not yet been reproduced.

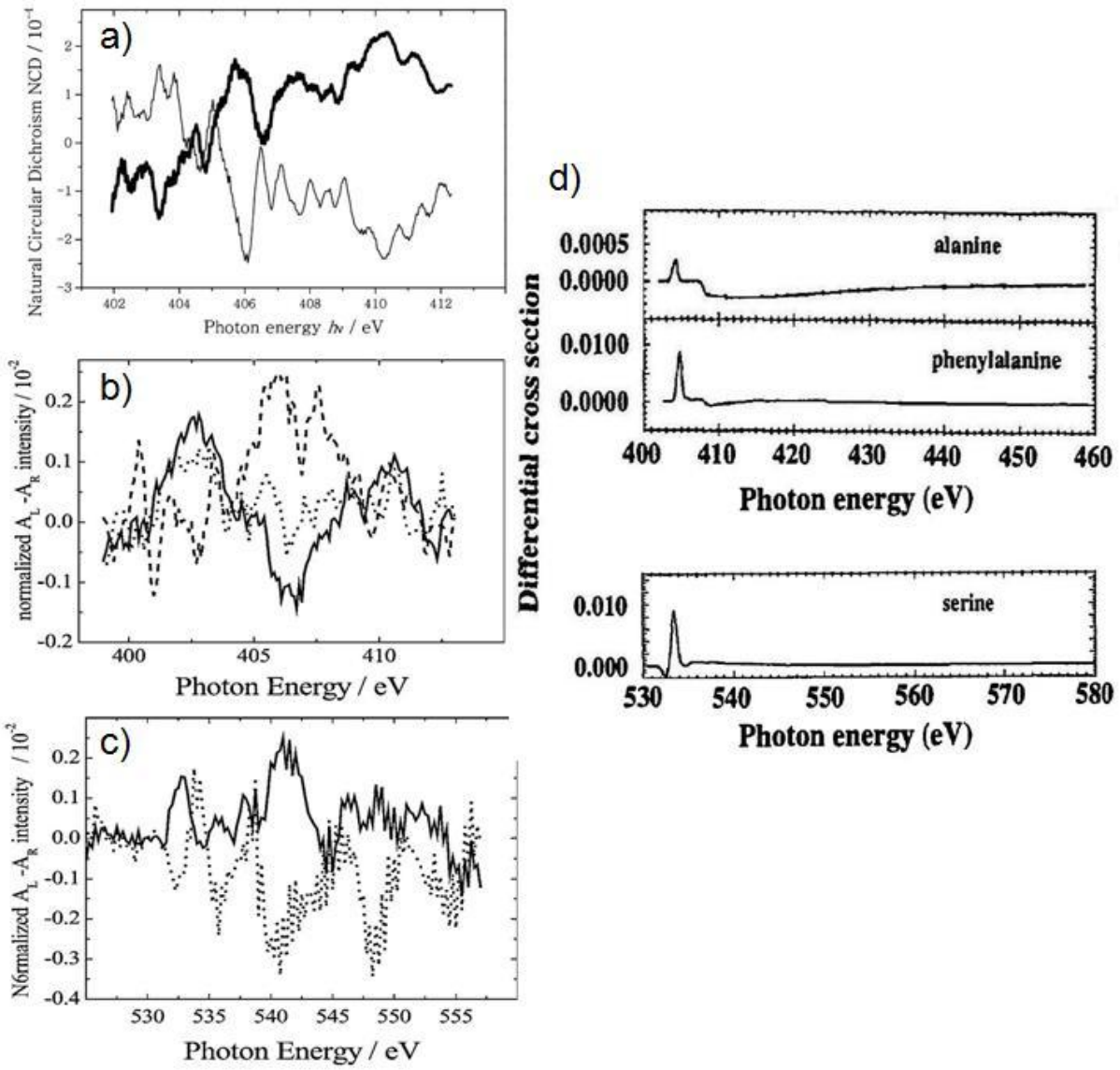

Figure 4.26 XNCD spectra of (a) alanine and (b) phenylalanine recorded at N 1s edge and (c) serine recorded at O 1s edge.[44,45] [Reprinted with permission from Journal of Electron Spectroscopy and Related Phenomena, 144-147, K. Nakagawa, F. Kaneko, Y. Ohta, M. Tanaka, T. Kitada, A. Agui, F. Fujii, A. Yokoya, K. Yagi-Watanabe and T. Yamada, Natural circular dichroism of amino acid films observed in soft X-ray and VUV region using polarizing undulator, 271-271, Copyright 2005, with permission from Elsevier.] [Reprinted with permission from Physica Scripta, T115, M. Tanaka, K. Nakagawa, A. Agui, K. Fujii, A. Yokoya, First Observation of Natural Circular Dichroism for Biomolecules in Soft X-ray Region Studied with a Polarizing Undulator, 873-876, Copyright 2005, with permission from Institute of Physics.] Calculated XNCD spectra of alanine and phenylalanine at N 1s edge and serine at O 1s edge.[46] [Reprinted with permission from Journal of Synchrotron Radiation, 6, L. Yang, O. Plashkevytch, O. Vahtras, V. Carravetta and H. Ågren, Near-edge X-ray absorption and dichroism in amino acids, 708-710, Copyright 1999, with permission from International Union of Crystallography.]

The preparation of amorphous sample by solution casting from amino acids and derivative compounds led to highly structured films unsuitable for XNCD measurement. Wet cells prepared from aqueous solution of solid compounds and from liquid compounds were unsuccessful as well due to poor spectral reproducibility. However, very satisfying results were obtained from amino acid derivatives functionalized polymer films in terms of amorphousness, sample reproducibility and X-ray radiation sensitivity as well as noise level and spectral reproducibility. Yet we were unsuccessful at recording XNCD signal from these samples and partially hold the instrumentation and experimental setup responsible; i.e.: beam instability, lack of reproducibility between LCP and RCP and unreliable normalization.
The STXM located on beam line 11.0.2. at the ALS is in high demand and beam time was not available to further pursue these experiments.

Considering the sample quality achieved by the amino acid derivatives functionalized polymers, it is suggested that the subsequent investigators consider making the following improvements to the measurements:

- Reducing time delay between spectral acquisition of the enantiomers
- Reducing time delay between spectral acquisition with RCP and LCP
- Reducing sample damage

Such improvements could be achieved by

- Simultaneously recording both enantiomers in a similar manner used for amino acid patterned films
- Recording with LCP and RCP light with fast switching, if permitted by the beam-line setup
- Defocusing the beam and shifting samples during the measurements to take advantage of the high polymer films homogeneity

It is also suggested to consider the synthesis of new polymer systems.

The Differential Scanning Calorimetry (DSC) study performed on [7]H indicated that the sample powder “as received” was in crystalline/amorphous state. However to perform NEXAFS measurements, [7]H had to be transferred onto a substrate by solution casting, which led to oriented samples. Due to its unique structure, [7]H is considered to be a very promising candidate for XNCD measurement. The choice of the STXM end-station to perform XNCD measurement was initially motivated by the sample’s high X-ray sensitivity. However, [7]H was found to have very low radiation sensitivity and may be suitable for TEY

measurement as a powdered sample. Such experiments could be performed on the EPU beam-line built recently at the Canadian Light Source (10-ID.1).

Finally, significant progress in *ab initio* theory has been made over the past fifteen years allowing calculations of XNCD for organic molecules.[2,6,7] As mentioned at the beginning of this chapter, computational approaches used to help assign NEXAFS spectra would certainly benefit from the development of XNCD measurement. Yet considering the noticeable advancement of the theory in this area, efforts should be put toward XNCD simulation for the purpose to better design future measurements.

4.6 References

(1) Bonner, W. A. *Origins of Life and Evolution of the Biosphere* **1991**, *21*, 59.

(2) Plashkevych, O.; Carravetta, V.; Vahtras, O.; Agren, H. *Chemical Physics* **1998**, *232*, 49.

(3) Barron, L. D. *Molecular Phsysics* **1971**, *21*, 241.

(4) Goulon, J.; Goulon-Ginet, C.; Rogalev, A.; Gotte, V.; Malgrange, C.; Brouder, C. *Journal of Synchrotron Radiations* **1999**, *6*, 673.

(5) Goulon, J.; Sette, F.; Moise, C.; Fontaine, A.; Perey, D.; Rudolf, P.; Baudelet, F. *Japanese Journal of Applied Physics* **1993**, *32*, 284.

(6) Alagna, L.; Fonzo, S. D.; Prosperi, T.; Turchini, S.; Lazzeretti, P.; Malagoli, M.; Zanasi, R.; Natoli, C. R.; Stephens, P. J. *Chemical Physics Letters* **1994**, *223*, 402.

(7) Kimberg, V.; Kosugi, N. *The Journal of Chemical Physics* **2007**, *126*, 245101.

(8) Rightor, E. G.; Hitchcock, A. P.; Ade, H.; Leapman, R. D.; Urquhart, S. G.; Smith, A. P.; Mitchell, G.; Fischer, D.; Shin, H. J.; Warwick, T. *Journal of Physical Chemistry B* **1997**, *101*, 1950.

(9) Cazaux, J. *Journal of Microscopy* **1997**, *188*, 106.

(10) Weik, M.; Ravelli, R. B. G.; Kryger, G.; McSweeney, S.; Raves, M. L.; Harel, M.; Gros, P.; Silman, I.; Kroon, J.; Sussman, J. L. *Proceedings of the National Academy of Sciences* **2000**, *97*, 623.

(11) Beetz, T.; Jacobsen, C. *Journal of Synchrotron Radiations* **2002**, *10*, 280.

(12) Cherezov, V.; Riedl, K. M.; Caffrey, M. *Journal of Synchrotron Radiation* **2002**, *9*, 333.

(13) Coffey, T.; Urquhart, S. G.; Ade, H. *Journal of Electron Spectroscopy and Related Phenomena* **2002**, *122*, 65.

(14) Sagstuen, E.; Sanderud, A.; Hole, E. O. *Radiation Research* **2004**, *162*, 112.

(15) Zubavichus, Y.; Fuchs, O.; Weinhardt, L.; Heske, C.; Umbach, E.; Denlinger, J. D.; Grunze, M. *Radiation Research* **2004**, *161*, 346.

(16) Zubavichus, Y.; Zharnikov, M.; Shaporenko, A.; Fuchs, O.; Weinhardt, L.; Heske, C.; Umbach, E.; Denlinger, J. D.; Grunze, M. *Journal of Physical Chemistry A* **2004**, *108*, 4557.

(17) Wang, J.; Stöver, H. D. H.; Hitchcock, A. P.; Tyliszczak, T. *Journal of Synchrotron Radiation* **2006**, *14*, 181.

(18) Carravetta, V.; Plashkevych, O.; Vahtras, O.; Agren, H. *Chemical Physics Letters* **1997**, *275*, 70.

(19) Turchini, S.; Zema, N.; Zennaro, S.; Alagna, L.; Stewart, B.; Peacock, R. D.; Prosperi, T. *Journal of the American Chemical Society* **2004**, *126*, 4532.

(20) Cahn, R. S.; Ingold, C.; Prelog, V. *Angewandte Chemie International Edition* **1966**, *5*, 385.

(21) Laarhoven, W. H.; Prinsen, W. J. C. Carbohelicenes and Heterohelicenes. In *Topics in Current Chemistry*; Vögtle, F., Weber, E., Eds.; Springer-Verlag: Berlin, **1984**; Vol. 125, Stereochemistry; pp 63.

(22) Spartan'04. Spartan; 04 ed.; Wavefunction, Inc.: Irvine, CA, **2003**.

(23) Meurer, K. P.; Vögtle, F. Helical Molecules in Organic Chemistry. In *Topic in Current Chemistry*; Springer-Verlag: Berlin, **1985**; Vol. 127, Organic Chemistry; pp 1.

(24) Grimme, S.; Harren, J.; Sobanski, A.; Vögtle, F. *European Journal of Organic Chemistry* **1998**, 1491.

(25) Zallen, R. *The Physics of Amorphous Solids*; John Wiley & Son, **1983**.

(26) Alexandrova, Z.; Sehnal, P.; Stara, I. G.; Stary, I.; Saman, D.; Urquhart, S. G.; Otero, E. *Collection of Czechoslovak Chemical Communications* **2006**, *71*, 1256.

(27) Ma, Y.; Chen, C. T.; Meigs, G.; Randall, K.; Sette, F. *Physical Review A* **1991**, *44*, 1848.

(28) Chen, C. T.; Ma, Y.; Sette, F. *Physical Review A* **1989**, *40*, 6737.

(29) Wight, G. R.; Brion, C. E. *Journal of Electron Spectroscopy and Related Phenomena* **1974**, *3*, 191.

(30) Tanaka, M.; Nakagawa, K.; Koketsu, T.; Agui, A.; Yokoya, A. *Journal of Synchrotron Radiation* **2001**, *8*, 1009.

(31) Kaznacheyev, K.; Osanna, A.; Jacobsen, C.; Plashkevych, O.; Vahtras, O.; Agren, H.; Carravetta, V.; Hitchcock, A. P. *Journal of Physical Chemistry A* **2002**, *106*, 3153.

(32) Hasselstrom, J.; Karis, O.; Weinelt, M.; Wassdahl, N.; Nilsson, A.; Nyberg, M.; Pettersson, L. G. M.; Samant, M. G.; Stohr, J. *Surface Science* **1998**, *407*, 221.

(33) Nyberg, M.; Hasselstrom, J.; Karis, O.; Wassdahl, N.; Weinelt, M.; Nilsson, A.; Pettersson, L. G. M. *Journal of Chemical Physics* **2000**, *112*, 5420.

(34) Gordon, M. L.; Cooper, G.; Morin, C.; Araki, T.; Turci, C. C.; Kaznacheev, K.; Hitchcock, A. P. *Journal of Physical Chemistry A* **2003**, *107*, 6144.

(35) Messer, B. M.; Cappa, C. D.; Smith, J. D.; Wilson, K. R.; Gilles, M. K.; Cohen, R. C.; Saykally, R. J. *Journal of Physical Chemistry B* **2005**, *109*, 5375.

(36) Zubavichus, Y.; Zharnikov, M.; Schaporenko, A.; Grunze, M. *Journal of Electron Spectroscopy and Related Phenomena* **2004**, *134*, 25.

(37) Cooper, G.; Gordon, M.; Tulumello, D.; Turci, C. C.; Kaznatcheev, K.; Hitchcock, A. P. *Journal of Electron Spectroscopy and Related Phenomena* **2004**, *137-140*, 795.

(38) Kaneko, F.; Tanaka, M.; Narita, S.; Kitada, T.; Matsui, T.; Nakagawa, K.; Agui, A.; Fujii, K.; Yokoya, A. *Journal of Electron Spectroscopy and Related Phenomena* **2005**, *144-147*, 291.

(39) Zubavichus, Y.; Shaporenko, A.; Grunze, M.; Zharnikov, M. *Journal of Physical Chemistry A Letters* **2005**, *109*, 6998.

(40) Zubavichus, Y.; Shaporenko, A.; Grunze, M.; Zharnikov, M. *Journal of Physical Chemistry B* **2006**, *110*, 3420.

(41) Oji, H.; Mitsumoto, R.; Ito, E.; Ishii, H.; Ouchi, Y.; Seki, K.; Yokoyama, T.; Ohta, T.; Kosugi, N. *Journal of Chemical Physics* **1998**, *109*, 10409.

(42) Ernst, K.-H.; Neuber, M.; Grunze, M.; Elleerbeck, U. *Journal of American Chemical Society* **2001**, *123*, 493.

(43) Urquhart, S. G.; Ade, H. *Journal of Physical Chemistry* **2002**, *106*, 8531.

(44) Nakagawa, K.; Kaneko, F.; Ohta, Y.; Tanaka, M.; Kitada, T.; Agui, A.; Fujii, F.; Yokoya, A.; Yagi-Watanabe, K.; Yamada, T. *Journal of Electron Spectroscopy and Related Phenomena* **2005**, *144-147*, 271.

(45) Tanaka, M.; Nakagawa, K.; Agui, A.; Fujii, K.; Yokoya, A. *Physica Scripta* **2005**, *T115*, 873.

(46) Yang, L.; Plashkevych, O.; Vahtras, O.; Carravetta, V.; Agren, H. *Journal of Synchrotron Radiation* **1999**, *6*, 708.

CHAPTER 5 NITROGEN 1S NEXAFS SPECTROSCOPY OF AMINO ACIDS: RESOLVING THE ZWITTERIONIC EFFECT

Amino acids have been extensively investigated by NEXAFS spectroscopy yet the assignment of a weak feature observed at low energy of nitrogen 1s edge remains controversial. In order for a highly susceptible measurement such as XNCD to be performed on amino acids a comprehensive understanding of the spectroscopy is vital. To improve the interpretation of amino acid NEXAFS spectroscopy I conducted a systematic study where the various protonated forms of glycine and model compounds were controlled. Theoretical calculations were used to support the assignment. The experimental and theoretical work done for this study is described and discuss in the following section presented under the form of the manuscript published in the Journal of Physical Chemistry A. [Reproduced with permission from Journal of Physical Chemistry A, 110, E. Otero and S.G. Urquhart, Nitrogen 1s Near-Edge X-ray Absorption Fine Structure Spectroscopy of Amino Acids: Resolving Zwitterionic Effects, 12121-12128, Copyright 2006, American Chemical Society]

For this research paper I was the primary investigator in the conception of the study, the preparation of the samples, the acquisition of the experimental data, the execution of the computed simulations, the interpretation of the results and the writing of the document. S.G. Urquhart provided guidance throughout the experiments and data analysis process and was greatly involved in editing this document.

The following chapter has been published in the Journal of Physical Chemistry A, 2006, volume 110, pages 12121-12128
DOI: 10.1021/jp064082a

CHAPTER 6 RESOLVING THE ROLE OF MULTIPLET AND COVALENT EFFECTS IN THE NEAR-EDGE X-RAY ABSORPTION FINE STRUCTURE (NEXAFS) SPECTROSCOPY OF FERROCENE AND FERROCENIUM COMPOUNDS.

The following **Chapters** (**6** to **9**) are dedicated to the investigation of organoiron compounds and polymers using NEXAFS spectroscopy. The characterisation of complex assemblies such as organometallic polymers by NEXAFS requires a basic understanding of the spectroscopy. In order to gain confidence in the interpretation of metal-arene NEXAFS spectroscopy, simple ferrocene complexes were investigated.

In **Chapter 6**, ferrocene and ferrocenium hexafluorophosphate, the oxidised salt of ferrocene, are investigated. The two complexes have similar bonding and only differ by their oxidation state, yet their Fe 2p and C 1s NEXAFS spectra show major dissimilarities. The experimental spectra are assigned with the help of Extended Hückel Molecular Orbital theory (EHMO) and Density Functional Theory (DFT) based computational programs, which both rely on covalent bonding theory and do not address potential atomic multiplet effects. A remarkably good agreement is obtained between experimental and simulated spectra for closed shell $3d^6$ low spin ferrocene while the spectra of open shell $3d^5$ low spin ferrocenium hexafluorophosphate show additional features assigned to atomic multiplet effects. The presence of both covalent bonding and atomic multiplet effects had been suggested previously in few studies and it is the first time that it is reported for metallocene complexes. The experimental and theoretical work done for this study is described and discussed in the following section presented in the form of the manuscript to be submitted to the Journal of Chemical Physics. The submission of this manuscript is waiting for IVO-configuration interaction calculations performed by Professor N. Kosugi to be made available to us.

For this research paper I was the primary investigator in the conception of the study, the preparation of the samples, the acquisition of the experimental data, the execution of the computed simulations, the interpretation of the results and the writing of the document. S.G. Urquhart provided guidance throughout the experiments and data analysis process and was greatly involved in editing this document.

The following chapter has been published in the Journal of Chemical Physics, 2009, volume 131, page 114313. The paper has been modified substantially since this thesis was submitted. DOI: 10.1063/1.3230101

Resolving the role of Multiplet and Covalent Effects in the Near-Edge X-ray Absorption Fine Structure (NEXAFS) Spectroscopy of Ferrocene and Ferrocenium Compounds.

Edwige Otero and Stephen G. Urquhart†*

Department of Chemistry, University of Saskatchewan, 110 Science Pl., Saskatoon, Saskatchewan, S7N 5C9, Canada.

* Corresponding author. E-mail: stephen.urquhart@usask.ca

† Contribution prepared while on sabbatical leave at the Canadian Light Source (Saskatoon, SK).

Abstract: The NEXAFS spectra of organometallic compounds are typically interpreted within one of two contrasting models, an atomic multiplet model or a covalent bonding model. To determine the relative importance of these models, we have recorded the iron 2p and carbon 1s NEXAFS spectra of decamethyl ferrocene ($3d^6$) and ferrocenium hexafluorophosphate ($3d^5$), two low spin compounds with a closed and open shell electron configuration, respectively. These species have a similar covalent bonding environment but a different electron configuration, allowing us to examine the role of atomic multiplet effects in a controlled experiment. We have interpreted these spectra with the aid of extended Hückel molecular orbital theory and density functional theory calculations. Our results indicate that the covalent bonding model is effective for closed shell ferrocene molecules but is ineffective for open shell ferrocenium molecules.

6.1 Introduction

Near-Edge X-ray Absorption Fine Structure (NEXAFS) spectroscopy is frequently used to investigate the chemical, electronic and structural properties of organic and inorganic materials. The NEXAFS spectra of organometallic compounds are frequently examined to investigate bonding and metal-ligand interactions, as the excitation of a core electron to unoccupied or partially occupied orbitals is sensitive to electronic character of these valence states.[1-6]

However, two divergent models are commonly used to interpret the NEXAFS spectra of organoiron compounds such as ferrocene: atomic multiplet theory[7] and covalent bonding

theory, the latter frequently expressed through molecular orbital (MO) or density functional theory (DFT) calculations.[4,8,9] In order to use NEXAFS for the chemical analysis of organoiron species, it is essential to resolve the relevance of these models.

Ferrocene-based materials have found a wide application in polymer, molecular electronics and bioorganometallic materials.[10] For example, the redox activity of self assembled monolayer materials terminated by ferrocene can be used to study electron transfer processes.[11] Other researchers have proposed oxidation-state switching in ferrocene self-assembled monolayers used as a model for high density molecular devices.[12] Ferrocene moieties are often included in polymers to improve their processability as well as the polymer's electric, magnetic, optical, redox and mechanic properties.[13] We are interested in the use of NEXAFS spectroscopy to characterize UV-induced fragmentation in organoiron polymers,[14] where it is necessary to differentiate between ferrocene, ferrocenium and iron oxide photochemical products. For these studies, it is essential to understand the sensitivity of NEXAFS spectroscopy to chemical structure (via covalent bonding and electronic delocalization effects) and electronic structure (via atomic multiplet effects).

Bis(η^5-cyclopentadienyl)iron ($[Fe^{II}(C_5H_5)_2]$, common name ferrocene) is a d^6 low spin diamagnetic compound with closed shell electron configuration $(e_{2g})^4$ $(a_{1g})^2$. Its oxidized form, bis(η^5-cyclopentadienyl)iron(1+) ($[Fe^{III}(C_5H_5)_2]^+$, common name ferrocenium) is a d^5 low spin paramagnetic compound with the open shelled configuration $(a_{1g})^2$ $(e_{2g})^3$.[15] Ferrocenium is found as a salt, with common counter ions such as PF_6^- or BF_4^-.

Ferrocene and ferrocene derivatives have been studied by NEXAFS spectroscopy or Inner Shell Electron Energy Loss Spectroscopy (ISEELS) at the iron 1s, 2p and 3p core edges and at the carbon 1s core edge.[5,6,16-18] ISEELS is the electron scattering analogue to x-ray absorption (NEXAFS) spectroscopy, providing gas phase spectra with modest energy resolution (0.5 – 0.7 eV fwhm).[19] NEXAFS spectroscopy can be performed for solids, liquids and gases, where the accessible energy resolution can easily exceed the core-hole lifetime broadening. In this paper, we will use the label NEXAFS as a generic label for NEXAFS and ISEELS spectroscopy measurements, except where specificity is necessary.

The NEXAFS spectrum of ferrocenium has not been reported from a well defined model, although the spectra of oxidized ferrocene self assembled monolayers reported by Himpsel *et al.* have been interpreted as that of ferrocenium.[12] We re-interpret these data below, based on the results of this study.

Early experimental and theoretical studies on metallocenes and carbonyl complexes showed that the metal 2p NEXAFS spectra are sensitive to the ligand identity (e.g. cyclopentadienyl versus CO) but are less sensitive to chemical substitution on the ligand, as inferred from the similarity of the Fe 2p spectrum of ferrocene to the Fe 2p spectra of alkane and alkene functionalized ferrocene compounds (e.g. Cp-R).[5,17,18,20] Furthermore similar Fe 2p spectra were obtained for $Fe(CO)_5$ and $Fe_2(CO)_9$ and for the mixed ligand compounds $RFe(CO)_3$ (R = butadiene, cylcohexadiene, cyclooctatetraene), which indicated that Fe 2p spectra are relatively insensitive to molecular geometry. Recently, we examined the C 1s and Fe 2p NEXAFS spectra of a series of cyclopentadienyl (Cp) substituted ferrocene species at higher energy resolution than these previous ISEELS measurements. New spectroscopic features are observed when Cp rings are substituted by groups with π-bonding adjacent to the Cp ring (e.g. Cp-$CH=CH_2$; Cp-COOH, etc), arising from the conjugation of the Cp and substituent π* density.[21]

The NEXAFS spectra of ferrocene and derivatives are often interpreted within a covalent bonding model, using MO or DFT theory calculations. For example, the first transition in the Fe 2p NEXAFS spectra of ferrocene is assigned as a transition to a MO that is mostly localized on the iron atom (3d character), but mixed with some Cp π* MO character.[17,22] This description reflects the covalent bonding, symmetry, and electronic delocalization in the organometallic compound's MOs, perturbed by the creation of a core hole.

Atomic multiplet theory is an alternative approach used to interpret the NEXAFS spectra of organometallic compounds. This model is based on the atomic electronic structure, perturbed by angular momentum interactions and the crystal field environment of the metal atom. In an isolated atom, multiplet splitting arises from the lifting of atomic orbital (AO) degeneracies (e.g. d^4, d^6, etc) into states from intra-atomic interactions such as electron spin and orbital angular momentum. For example, a 3d atom with a d^2 configuration will have ^1S, ^1D, ^1G, ^3P and ^3F states. In an ionic compound, this atomic electron configuration is further perturbed by inter-atomic Coulombic interactions, described by crystal field theory. Core excitation in NEXAFS spectroscopy (e.g; 2p → 3d transitions) creates additional complications, as the unpaired electron in the core hole orbital and the optical orbital will lead to new spin-spin and spin-orbit interactions, and the repulsion between the core excited orbital electrons (e.g. $2p^5$) and the 3d electrons will decrease.[23]

De Groot *et al*. have predicted the "fingerprint" NEXAFS spectra of 3d metal cations in a wide range of crystal field splitting environments using atomic multiplet calculations.[24] This model has been extended to consider charge transfer and back-bonding effects in ferro- and ferri-cyanate complexes.[3,9] In these charge transfer calculations, multiplets are considered for the $3d^n$ state as well as for charge transfer states (e.g. $3d^{n+1}$; $3d^{n-1}$), where an electron has been transferred between the ligand and metal atom.[7]

The purpose of this paper is to examine the relevance of the atomic multiplet and the covalent bonding models for the accurate interpretation of the NEXAFS spectra of organoiron species such as ferrocene and ferrocenium. We have acquired experimental NEXAFS spectra of decamethyl ferrocene and ferrocenium hexafluorophosphate at the Fe 2p and the C 1s core edges, and compared these data to Inner Shell Electron Energy Loss Spectra (ISEELS) of gas phase ferrocene from the literature.[17] Ferrocene and ferrocenium differ by only the oxidation state of iron and the presence of the counter ion, and therefore will have nearly identical covalent bonding. This provides a controlled experiment for demonstrating the presence of atomic multiplet effects in the NEXAFS spectra of strongly covalent ferrocene compounds.

Density Functional Theory (DFT) and Extended Hückel Molecular Orbital (EHMO) theory calculations are used to aid the assignment of NEXAFS spectra. Neither method explicitly considers angular momentum interactions (e.g. spin orbit and spin-spin interactions that lead to atomic multiplet effects). We find that these calculations are effective at simulating the Fe 2p and C 1s spectra of ferrocene ($Fe^{II}(Cp)_2$) and decamethyl ferrocene ($Fe^{II}(Cp\text{-}(CH_3)_5)_2$), but the agreement between experiment and theory is poor for open-shelled ferrocenium hexafluorophosphate ($[Fe^{III}(Cp)_2][PF_6]$). Extra features are observed in the experimental spectra, indicating that multiplet effects are present and must be considered in combination with covalent effects when interpreting the NEXAFS spectra of open-shelled organoiron species.

6.2 Experimental Section

6.2.1 Reagents and Sample Preparation

Bis(pentamethyl-η^5-cyclopentadienyl)iron ($Fe^{II}(Cp\text{-}(CH_3)_5)_2$, 97%, also known as decamethyl ferrocene) and Bis(η^5-cyclopentadienyl)iron(+1) hexafluorophosphate

($[Fe^{III}(Cp)_2][PF_6]$, 97%, also known as ferrocenium hexafluorophosphate) were obtained commercially from Aldrich and used without further purification. Potassium hexacyanoferrate(II) ($K_4[Fe(CN)_6]$, 99%) was purchased from BDH and used as received. The spectrum for $Fe^{II}(Cp)_2$ was reproduced from the literature as it is too volatile for room temperature experiments in the solid state.

Samples were prepared by pressing milligram amounts of the compounds into indium foil (0.25 mm thick, 99.99% purity, Aldrich). Additionally $[Fe^{III}(Cp)_2][PF_6]$ was prepared by pressing milligram amounts of sample into conductive tape (Structure Probe Inc) and solid copper (cut from Conflat gaskets). $[Fe^{III}(Cp)_2][PF_6]$ was also measured in transmission mode, for which a suspension of $[Fe^{III}(Cp)_2][PF_6]$ in ethanol was cast onto 100 nm thick silicon nitride membrane window (Norcada Inc).

Gold samples used in the normalization process were prepared by successively depositing 20 angstroms of chromium (chrome plated tungsten rod; R.D. Mathis) and several hundreds of angstroms of gold on clean silicon wafer (N-type, P doped, orientation (100), 1-10 Ω/cm resistivity; Silicon Inc.), using a thermal evaporator (Datacomp Scientific).

6.2.2 NEXAFS Measurements

All Fe 2p NEXAFS spectra and the C 1s NEXAFS spectrum of $Fe^{II}(Cp\text{-}(CH_3)_5)_2$ were recorded using sample-current Total Electron Yield (TEY) mode, on the SGM beamline (11-ID.1) at the Canadian Light Source (University of Saskatchewan, Canada). This beamline is equipped with a Dragon – type spherical grating monochromator and was designed for high resolution soft X-ray spectroscopy studies.[25] The spectroscopic resolving power ($E/\Delta E$) for these measurements is estimated to be better than 3200.

The Fe 2p spectrum of $[Fe^{III}(Cp)_2][PF_6]$ were collected in Total Electron Yield (TEY) from a sample pressed into conductive carbon tape. This compound rapidly reacts with In and Cu substrates, changing in colour from dark blue to dark brown in less than 15 minutes. This rapid reaction was evident from considerable changes in the NEXAFS spectra (included in **Figure 6.5** of the supporting material). However, excellent spectroscopic reproducibility and stability was achieved using a conductive carbon tape substrate.

The carbon-tape substrate used for the Fe 2p NEXAFS spectra of $[Fe^{III}(Cp)_2][PF_6]$ would contaminate the C 1s spectra. Therefore, the C 1s NEXAFS spectrum of $[Fe^{III}(Cp)_2][PF_6]$ was recorded in transmission mode, using a Si_3N_4 membrane as a substrate.

These experiments were performed using the Scanning Transmission X-ray Microscope (STXM) on beam line 10-ID.1 of the Canadian Light Source (University of Saskatchewan, Canada), with 20 μm exit slits (dispersive and non-dispersive). This sample was cast onto a Si_3N_4 membrane, which was less reactive than the In and Cu substrates used for TEY measurements. The Fe 2p spectra acquired in the STXM microscope of this sample (see supporting material **Figure 6.5** spectrum f) shows only minor signs of sample deterioration.

Fe 2p edge NEXAFS spectra recorded by TEY were normalized using the double normalization method, following the procedure described elsewhere.[21,26] Here,

$$\text{normalized spectra} = [\, I / I_0 \,] / [\, I_R / I_{0R} \,] \qquad \textbf{Equation 6.1}$$

where (I) corresponds to the sample current and (I_0) the current from a mesh-monitor located upstream of the sample. The reference current (I_R) was recorded from a freshly evaporated gold coated silicon wafer, using the same scan parameters (energy range, energy step increments, slits position) as for the iron samples.

C 1s edge NEXAFS spectra recorded by TEY were normalized by taking the ratio [sample current, I] / [gold-reference current, I_R], where the gold reference spectrum was acquired in a separate scan. To remove normalization artifacts, the intensity of the gold reference spectrum was modified so that its intensity in the pre-edge region superimposed with that of the sample spectrum, as described elsewhere.[21] The transmission C 1s NEXAFS spectrum of $[Fe^{III}(Cp)_2][PF_6]$ was converted into optical density (O.D.), using the formula: $OD = -\ln(I/I_0)$.

The Fe 2p edge spectra were calibrated relative to the lowest energy, sharp feature in the Fe 2p NEXAFS spectrum of $K_4[Fe(CN)_6]$ at 710.25 eV.[21] This calibration was previously established using the well-calibrated F 1s spectrum of SF_6.[27] The C 1s TEY spectra were calibrated relative to the C 1s → π*(C=O) in urea, and reported at 289.53 eV by Urquhart *et al*., after an ISEELS absolute energy scale calibration.[28] The C 1s transmission spectrum of $[Fe^{III}(Cp)_2][PF_6]$ was calibrated to Carbon 1s → 3p(ν=0) transition in the NEXAFS spectrum of gaseous CO_2 (294.96 eV),[29] leaked into the STXM microscope.

6.2.3 Calculations

Fe 2p NEXAFS spectra were interpreted with the aid of Extended Hückel Molecular Orbital (EHMO) theory using the Computer Aided Composition of Atomic Orbitals (CACAO) program.[30] EHMO calculations can be used to explore the effects of covalent

bonding, as this method is well parameterized for organoiron species and is effective for qualitative studies of the effect of π-conjugation in the NEXAFS spectra of organic and organometallic species.[31] DFT calculations are also appropriate for organoiron compounds;[22] however, our version of the DFT code could not perform Fe 2p edge calculations at the time of this investigation.

The Cartesian coordinates of $Fe^{II}(Cp)_2$, $Fe^{II}(Cp\text{-}(CH_3)_5)_2$ and $[Fe^{III}(Cp)_2][PF_6]$ were obtained from the literature and correspond approximately to D_{5d} symmetry.[32] The equivalent ionic core virtual orbital model (EICVOM)[33] is used to account for electronic relaxation due to the creation of the core hole. In the EICVOM model, the core excited atom is replaced by the atom with one greater nuclear charge (e.g. Z+1 approximation), and the molecule is given a +1 charge to correct the valence electron count. The atomic propensity approximation is used to calculate the intensity of the spectroscopic features. Within the Linear Combination of Atomic Orbital – Molecular Orbital (LCAO-MO) description, the states accessed by the highly localized core excitation transitions are well described by the unoccupied AOs on the core excited atom. Transitions to these unoccupied AOs on the core excited atom can be described by the Laporte selection rule for atomic electronic transitions ($\Delta l = \pm 1$; e.g. 2p → 3d or 2p → 4s). Spectroscopic intensities are assumed to be proportional to the sum of the square of the LCAO coefficients for the unoccupied AOs centered on the core excited atom, for each virtual MO. Simulated spectra were obtained by calculating a Gaussian line shape for each transition using the program SIMILE2.[34] Line widths with a 0.36 eV FWHM were used for the low energy, based on the Fe $2p_{(3/2)}$ core hole lifetime.[35] We use Gaussian lineshapes for simplicity, particularly as we use these calculations for a qualitative analysis and not for a quantitative shape comparison. The actual experimental line shape should be a Voigt function; a convolution of the natural Lorentizian lineshape (~0.36 eV fwhm) and a Gaussian lineshape for the estimated monochromator resolution (~0.2 eV fwhm). However, the natural lineshape is known to vary for different peaks in the metal 2p spectra, from different lifetime effects and from vibrational broadening.[23]

The C 1s NEXAFS spectra were simulated using the Stockholm-Berlin version 2.1 of deMon (StoBe2005, dated 12/9/2005).[36] This program is based on self-consistent solutions of the Kohn-Sham DFT. The NEXAFS calculations presented here were performed using the methods from the Wilks *et al*. study of ferrocene-labeled peptides.[22] NEXAFS spectra are simulated by calculating the transition probabilities between half-occupied core hole and optical orbital optimized in the potential of this half-occupied core-hole excited molecule. For

all atoms triple zeta plus valence polarization (TZVP) orbital basis sets were used as well as TZVP derived A5 auxiliary basis sets. For the atom from which the core excited electron originates, iii-igol basis set has been employed. The core potential model was applied on all other carbon atoms in order to avoid mixing with the core excited carbon atom. NEXAFS curves were obtained by Gaussian convolution of the stick spectra generated by StoBe. Full-width at half-maximum (FWHM) of 0.4 eV was used below 290 eV, FWHM of 2 eV above 300 eV and a linear increase from 0.4 eV to 2 eV between 290 eV and 300 eV. These line widths are selected to approximately match the linewidths observed in the experimental spectra, increasing at higher energy with the trend to greater lifetime broadening. The lower energy C 1s → π* features will be broadened beyond lifetime broadening (~80 meV) by vibrational effects. For example, the high resolution C 1s NEXAFS spectrum of benzene has a vibrational features with an energy of ~0.42 eV (C-H stretch) and ~0.18 eV (non-totally symmetry C-C stretch) above the adiabatic transition.[37] These vibrational features are difficult to resolve in the high resolution NEXAFS spectra of complex molecules and polymers,[38] hence a simple Gaussian is justified for this qualitative comparison.

6.3 Results and Discussion

6.3.1 Fe 2p edge NEXAFS Spectra

Figure 6.1 presents the Fe $2p_{3/2}$ and $2p_{1/2}$ spectra of $Fe^{II}Cp_2$ (reproduced from Wen *et al.*[17]), $Fe^{II}(Cp\text{-}(CH_3)_5)_2$ and $[Fe^{III}(Cp)_2][PF_6]$. The transition energies and assignments for these compounds are presented in **Table 6.1**.

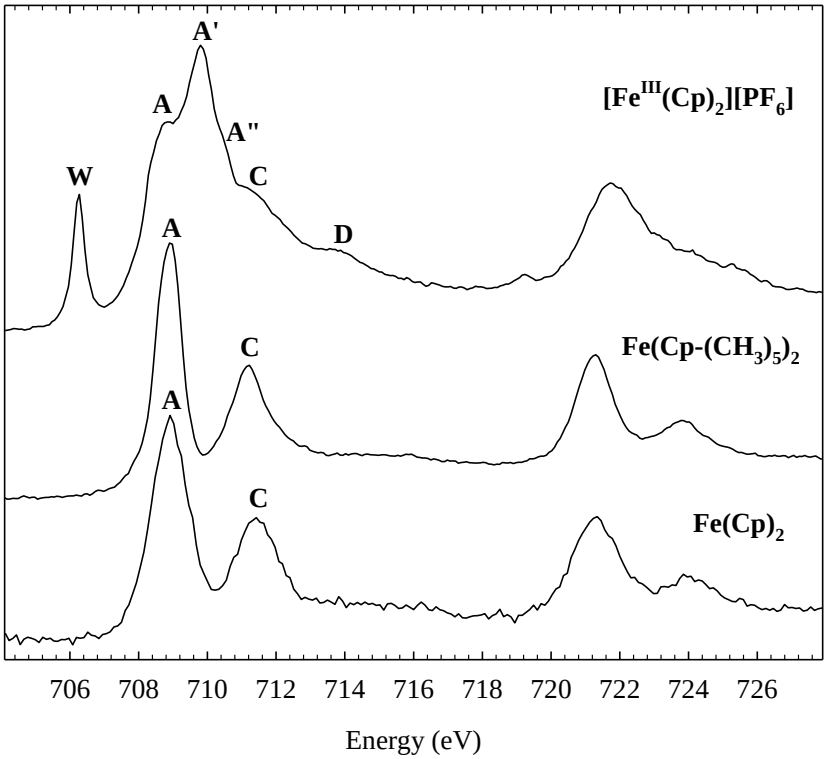

Figure 6.1 Fe 2p NEXAFS spectra of $[Fe^{III}(Cp)_2][PF_6]$, $Fe^{II}(Cp\text{-}(CH_3)_5)_2$ and $Fe^{II}(Cp)_2$.[17] The spectra have been offset by a constant for clarity.

Peak Labels	$Fe^{II}(Cp)_2$	$Fe^{II}(Cp\text{-}(CH_3)_5)_2$	$[Fe^{III}(Cp)_2][PF_6]$	Assignments	
				Fe $2p_{3/2}$	Fe $2p_{1/2}$
W			706.25	3d / Cp π* SOMO (e_{2g})	
A	708.9	708.87	708.84	3d / Cp π* (e_{1g})	
A'			709.80	Multiplet	
A"			710.45	Multiplet	
C	711.5	711.18	711.5	3d / Cp π* (e_{2g})	
D			713.8	Multiplet	
W			719.23		3d/Cp π* SOMO (e_{2g})
A	721.2	721.27	721.76		3d/Cp π* (e_{1g})
C	723.9	723.82			3d/Cp π* (e_{2g})

Table 6.1 Transition energies (eV) and Assignments for the Fe 2p NEXAFS spectra of $Fe^{II}(Cp)_2$, $Fe^{II}(Cp\text{-}(CH_3)_5)_2$ and $[Fe^{III}(Cp)_2][PF_6]$. Transition energy values for $Fe^{II}(Cp)_2$ were reproduced from Wen *et al.*[17]

The Fe 2p spectra of $Fe^{II}Cp_2$ and $Fe^{II}(Cp\text{-}(CH_3)_5)_2$ are dominated at the Fe $2p_{3/2}$ and $2p_{1/2}$ edges (707-713 and 720-726 eV, respectively) by a two features, a strong peak at low

energy and a weaker peak ~2.5 eV higher. The spectrum of $[Fe^{III}(Cp)_2][PF_6]$ is substantially different from $Fe^{II}(Cp)^2$, even though this species only differs by +1 oxidation state. At the low energy side (~706.25 eV), a narrow feature labeled W is observed; this feature is nearly absent at the Fe $2p_{1/2}$ edge. The most intense peak (A') occurs at 709.80 eV, and series of weaker peaks and shoulders occur up to ~714 eV; these features do not occur in the spectra of the Fe(II) species. At the Fe $2p_{1/2}$ edge, only a broad feature is observed above 720 eV.

The simulated Fe 2p edge spectra of $Fe^{II}(Cp)_2$, $Fe^{II}(Cp\text{-}(CH_3)_5)_2$ and $[Fe^{III}(Cp)_2][PF_6]$ are presented in **Figure 6.2**. Detailed peak assignments are presented in **Table 6.2**. Only one band is represented because EHMO does not consider the spin-orbit splitting that leads to the $2p_{3/2}$ and $2p_{1/2}$ edges. These spectra are presented on an orbital energy scale (term value (TV) = Ionization Potential – Excitation Energy) and therefore show only valence electronic effects.

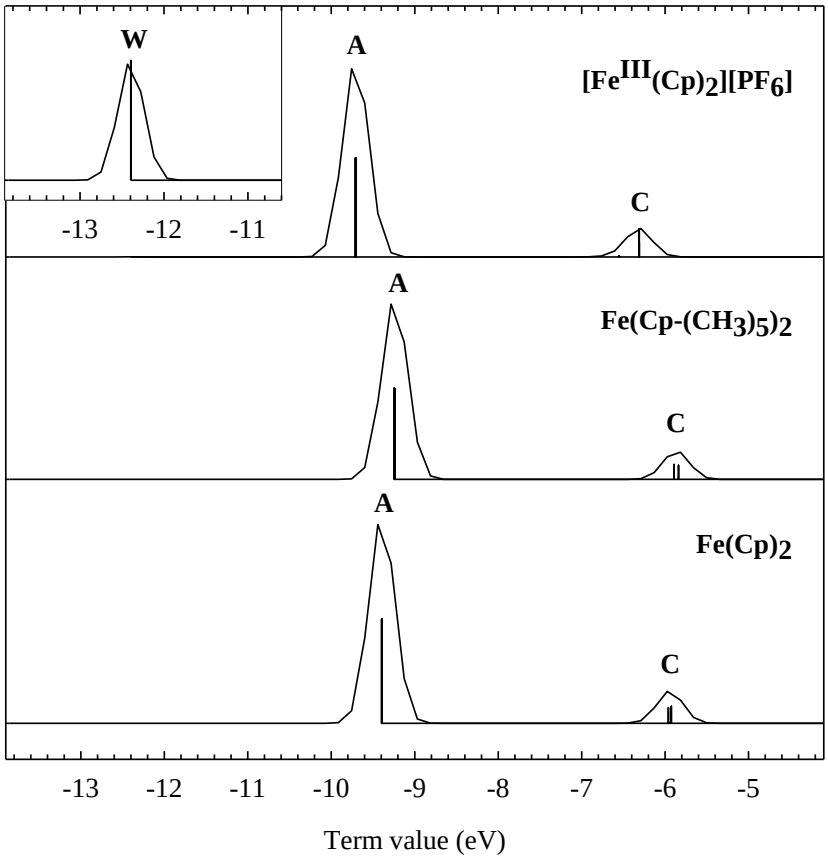

Figure 6.2 Simulated Fe 2p edge x-ray absorption spectra of $[Fe^{III}(Cp)_2][PF_6]$, $Fe^{II}(Cp\text{-}(CH_3)_5)_2$ and $Fe^{II}(Cp)_2$ calculated using EHMO theory (CACAO program). The spectra have been offset by a constant for clarity.

Peak Labels	$Fe^{II}(Cp)_2$	$Fe^{II}(Cp\text{-}(CH_3)_5)_2$	$[Fe^{III}(Cp)_2][PF_6]$
W			Fe 3d /**Cp π***
A	Fe $3d_{xz}$ (e_{1g})/Cp π*	Fe $3d_{xz}$ (e_{1g}-like)/Cp π*	Fe $3d_{xz}$ (e_{1g}) /Cp π*
	Fe $3d_{yz}$ (e_{1g})/Cp π*	Fe $3d_{yz}$ (e_{1g}-like)/Cp π*	Fe $3d_{yz}$ (e_{1g}) /Cp π*
Forbidden	Cp π* (e_{2u})	Cp π* (e_{2u}-like)	Cp π* (e_{2u})
	Cp π* (e_{2u})	Cp π* (e_{2u}-like)	Cp π* (e_{2u})
C	Fe $3d_{xy}$/**Cp π* (e_{2g})**	Fe $3d_{xy}$/**Cp π* (e_{2g}-like)**	Fe $3d_{xy}$/**Cp π* (e_{2g})**
	Fe $3d_{x^2-y^2}$/**Cp π* (e_{2g})**	Fe $3d_{x^2-y^2}$/**Cp π* (e_{2g}-like)**	Fe $3d_{x^2-y^2}$/**Cp π* (e_{2g})**

Table 6.2 Assignment of CACAO simulated Fe 2p NEXAFS spectra of $Fe^{II}(Cp)_2$, $Fe^{II}(Cp\text{-}(CH_3)_5)_2$ and $[Fe^{III}(Cp)_2][PF_6]$. Localization of the molecular orbital on the metal or ligand is indicted by bold scripts.

In early studies performed on manganese, iron and cobalt complexes with carbonyl and cyclopentadienyl ligands, Hitchcock *et al*. assigned the low energy feature (A) to a Fe 2p → 3d (e_{1g}) orbital, and the weaker band (C; 2.5 eV higher) to a Fe 2p → Cp π* (e_{2u}) orbital.[5,17] Fronzoni *et al*. used ab inito calculations to simulate Fe 2p XAS spectra of $Fe^{II}(Cp)_2$ and metal carbonyl complexes.[18] For $Fe^{II}(Cp)_2$ they assigned the strong low energy feature to essentially metal 3d (e_{1g}) orbital mixed with some ligand orbital. However they assigned the second resonance as a transition to a ligand π* (e_{2g}) orbital mixed with iron 3d (e_{2g}-like) orbital. The assignment of Hitchcock *et al*. is clearly mislabeled, as Fe 3d orbitals cannot transform as the e_{2u} representation in the D_{5d} point group.

Our simulated Fe 2p spectra of $Fe^{II}(Cp)_2$ and $Fe^{II}(Cp\text{-}(CH_3)_5)_2$ reproduce the two features, labeled A and C. Feature (A) originated from transitions to doubly degenerate MOs that have a large Fe $3d_{xz}$ and $3d_{yz}$ contribution, mixed with Cp π* (e_{1g}) orbital character. The second peak (C) also originates from a doubly degenerate Cp π* (e_{2g}) MO with a small Fe $3d_{xy}$ and $3d_{x^2-y^2}$ contribution (as indicated by smaller Fe 3d AO orbital coefficients and peak size). There is a third set of MOs with an energy between A and C, but these are exclusively ligand Cp π* (e_{2u}) character. As Fe 3d character is excluded by symmetry, these e2u MOs cannot contribute to the Fe 2p spectra (see supporting material **Figure 6.6** for MO drawings).

A covalent interpretation of the Fe 2p NEXAFS spectra of Fe(II) species is supported by our recent NEXAFS investigation of substituted ferrocene molecules. A new feature appears between features (A) and (C) in the Fe 2p NEXAFS spectra of some substituted ferrocene species.[21] When the cyclopentadienyl (Cp) group of ferrocene is substituted with a

group that contains a double bond immediately adjacent to the Cp ring (e.g. Cp-CH=CH_2; Cp-COOH), a new feature (B) is observed in the experimental NEXAFS spectra. When this substitutent is saturated (e.g. R = Cl, CH_3), this feature is not observed in the Fe 2p spectra. An example of the lack of feature (B) can be seen in the Fe 2p NEXAFS spectrum of Fe^{II}(Cp-$(CH_3)_5)_2$ (**Figure 6.1**). EHMO calculations clearly show that this peak (B) and a higher peak (D) arises from conjugation of the substituent π* character with the Cp π* character.[21] This is clearly a covalency effect, and provides clear evidence for the existence of covalent effects in the Fe 2p NEXAFS of ferrocene compounds. De Groot has acknowledged that the ISEELS spectrum of ferrocene bears little resemblance to the ligand field multiplet spectra, and noted that a better description of the covalence effects and of π-(back)bonding is required.[7]

The results of the Fe 2p EHMO calculations for $[Fe^{III}(Cp)_2][PF_6]$ are similar to that from $Fe^{II}(Cp)_2$, except for a weak, Singly Occupied MO (SOMO) at lower energy, labeled W (see inset window in **Figure 6.2**). The MO for this feature is predicated to be mostly Cp π*, with a very small 3d metal contribution. The EHMO calculations clearly do not reproduce the extra features (A', A", D) observed in the experimental Fe 2p spectrum of $[Fe^{III}(Cp)_2][PF_6]$. It is also interesting to notice the similarity between the Fe 2p NEXAFS spectrum of $[Fe^{III}(Cp)_2][PF_6]$ and the spectra of other d^5 low spin compounds.[2,3,9,39] A sharp peak similar to feature W in the Fe 2p spectrum of $[Fe^{III}(Cp)_2][PF_6]$ observed at low energy in other d^5 low spin iron compounds.

The order of top six occupied MOs and the SOMO for ferrocene and ferrocenium compounds are inconsistently reported in other theoretical studies.[40,41] We found that our EHMO calculations were very sensitive to small changes to the metal-ligand distance. Therefore, there is some uncertainty as to whether our EHMO calculation correctly predicts the orbital character of the SOMO. Nevertheless, a SOMO with 3d character will lead to a pre-edge Fe 2p → 3d transition, as observed in our experimental Fe 2p spectra (feature W).

In contrast to the Fe 2p NEXAFS spectra of Fe(II) species, the Fe 2p NEXAFS spectrum of $[Fe^{III}(Cp)_2][PF_6]$ shows numerous resonances that cannot be assigned based on the EHMO calculations. A list of potential electronic configurations for $Fe^{II}(Cp)_2$ and $[Fe^{III}(Cp)_2][PF_6]$ are presented in **Table 6.3**; there are clearly more microstates for core excited $[Fe^{III}(Cp)_2][PF_6]$ than for $Fe^{II}(Cp)_2$. While not all of the states depicted in **Table 6.3** will lead to a transition, it is legitimate to expect more multiplet features in the NEXAFS spectra of $[Fe^{III}(Cp)_2][PF_6]$ than $Fe^{II}(Cp)_2$.

	$Fe(Cp)_2$		$[Fe^{III}(Cp)_2][PF_6]$	
	Electron configuration	**States**	**Electron configuration**	**States**
Ground State	$(a_{1g})^2\ (e_{2g})^4$	$^1A_{1g}$	$(a_{1g})^2\ (e_{2g})^3$	$^2E_{2g}$

		$Fe(Cp)_2$		$[Fe^{III}(Cp)_2][PF_6]$	
	Core (2p) excited state	**Electron configuration**	**States[a]**	**Electron configuration**	**States[a,b]**
SOMO	$2p_x, 2p_y\ (e_{1u})^3$	N/A		$(a_{1g})^2\ (e_{2g})^4$	$^2E_{1u}$
	$2p_z\ (a_{2u})^1$			$(a_{1g})^2\ (e_{2g})^4$	$^2A_{2u}$
1st excited state	$2p_x, 2p_y\ (e_{1u})^3$	$(a_{1g})^2(e_{2g})^4(e_{1g})^1$	$^{1,3}A_{1u}, {}^{1,3}A_{2u}, {}^{1,3}E_{2u}$	$(a_{1g})^2\ (e_{2g})^3\ (e_{1g})^1$	$4x(^{2,4}A_{1u}, {}^{2,4}A_{2u}, {}^{2,4}E_{1u}, {}^{2,4}E_{2u})$
	$2p_z\ (a_{2u})^1$	$(a_{1g})^2(e_{2g})^4(e_{1g})^1$	$^{1,3}E_{1u}$	$(a_{1g})^2\ (e_{2g})^3\ (e_{1g})^1$	$4x(^{2,4}E_{1u}, {}^{2,4}E_{2u})^a$
2nd excited state	$2p_x, 2p_y\ (e_{1u})^3$	$(a_{1g})^2(e_{2g})^4(e_{2u})^1$	$^{1,3}E_{1g}, {}^{1,3}E_{2g}$	$(a_{1g})^2\ (e_{2g})^3\ (e_{2u})^1$	$4x(^{2,4}A_{1g}, {}^{2,4}A_{2g}, {}^{2,4}E_{1g}, {}^{2,4}E_{2g})$
	$2p_z\ (a_{2u})^1$	$(a_{1g})^2(e_{2g})^4(e_{2u})^1$	$^{1,3}E_{2g}$	$(a_{1g})^2\ (e_{2g})^3\ (e_{2u})^1$	$4x(^{2,4}A_{1g}, {}^{2,4}A_{2g}, {}^{2,4}E_{1g})$
3rd excited state	$2p_x, 2p_y\ (e_{1u})^3$	$(a_{1g})^2\ (e_{2g})^4\ (e_{2g})^1$	$^{1,3}E_{1u}, {}^{1,3}E_{2u}$	$(a_{1g})^2\ (e_{2g})^3\ (e_{2g})^1$	$4x(^{2,4}A_{1u}, {}^{2,4}A_{2u}, {}^{2,4}E_{1u}, {}^{2,4}E_{1u}, {}^{2,4}E_{2u})$
	$2p_z\ (a_{2u})^1$	$(a_{1g})^2\ (e_{2g})^4\ (e_{2g})^1$	$^{1,3}E_{2u}$	$(a_{1g})^2\ (e_{2g})^3\ (e_{2g})^1$	$4x(^{2,4}A_{1u}, {}^{2,4}A_{2u}, {}^{2,4}E_{1u})$

Table 6.3 Electron configuration and states of $Fe(Cp)_2$ and $[Fe^{III}(Cp)_2][PF_6]$ in ground and excited states. a.) Except for the doublet SOMO for ferrocenium, core excited state in ferrocene and ferrocenium can be singlet/triplet or doublet/quartet, respectively. The spin selection rule, $\Delta s=0$, is not strictly applicable where higher Z atoms such as Fe are present. b.) While some microstates of identical symmetry (e.g. $^2A_{1u}$, $^2A_{2u}$) for a core excited state may be degenerate, not all microstates will have the same energy; therefore additional features are to be expected in the core excited states of ferrocenium.

Other studies have indicated a greater incidence of multiplet effects in open-shell systems.[2] One should also expect that multiplet effects will be stronger for optical orbitals that are highly localized to the Fe 3d AOs (e.g. with smaller covalent interactions with the Cp rings).[7] The Fe 2p → 3d (e_{1g}) transition (feature A) is more strongly localized on the iron atom than feature C, which has greater Cp π*-character, and strong multiplet splitting (features A, A', A") are observed for feature A. However, definitive assignment of these features is beyond our capabilities.

Our EHMO calculations successfully reproduce the relative intensity of the two main features in the Fe 2p NEXAFS spectrum of $Fe^{II}(Cp)_2$ and $Fe^{II}(Cp\text{-}(CH_3)_5)_2$. The EHMO calculations of $[Fe^{III}(Cp)_2][PF_6]$ successfully predict the presence of the low energy feature W, but severely underestimate its intensity. These EHMO calculations do not predict the extra features (A', A", and D) observed in the Fe 2p NEXAFS spectrum of $[Fe^{III}(Cp)_2][PF_6]$. These differences between the EHMO simulation and the experimental Fe 2p spectrum of $[Fe^{III}(Cp)_2][PF_6]$ provide clear evidence for multiplet effects in the Fe 2p NEXAFS spectrum ferrocenium, as EHMO is only sensitive to covalent effects. In contrast, the similarity of the NEXAFS spectra of Fe(II) species to their EHMO simulations and the presence of strong π*-substituent effects in substituted ferrocene species points to a significant role for covalency effects in Fe 2p NEXAFS spectra in closed shelled ferrocene species.

6.3.2 Carbon 1s edge NEXAFS Spectra

The C 1s NEXAFS spectra of $Fe^{II}Cp_2$ (reproduced from Wen *et al.*[17]), $Fe^{II}(Cp\text{-}(CH_3)_5)_2$ and $[Fe^{III}(Cp)_2][PF_6]$ are presented in **Figure 6.3**. The transition energies and assignments are presented in **Table 6.4**. The spectrum of $Fe^{II}(Cp)_2$ and $Fe^{II}(Cp\text{-}(CH_3)_5)_2$ show two well resolved peaks A and C, with an intensity inversion relative to the Fe 2p NEXAFS spectrum. The simulated C 1s edge NEXAFS spectra of $Fe^{II}(Cp)_2$, $Fe^{II}(Cp\text{-}(CH_3)_5)_2$ and $[Fe^{III}(Cp)_2][PF_6]$ from DFT calculations are presented in **Figure 6.4**. Detailed peak assignments are presented in **Table 6.5**.

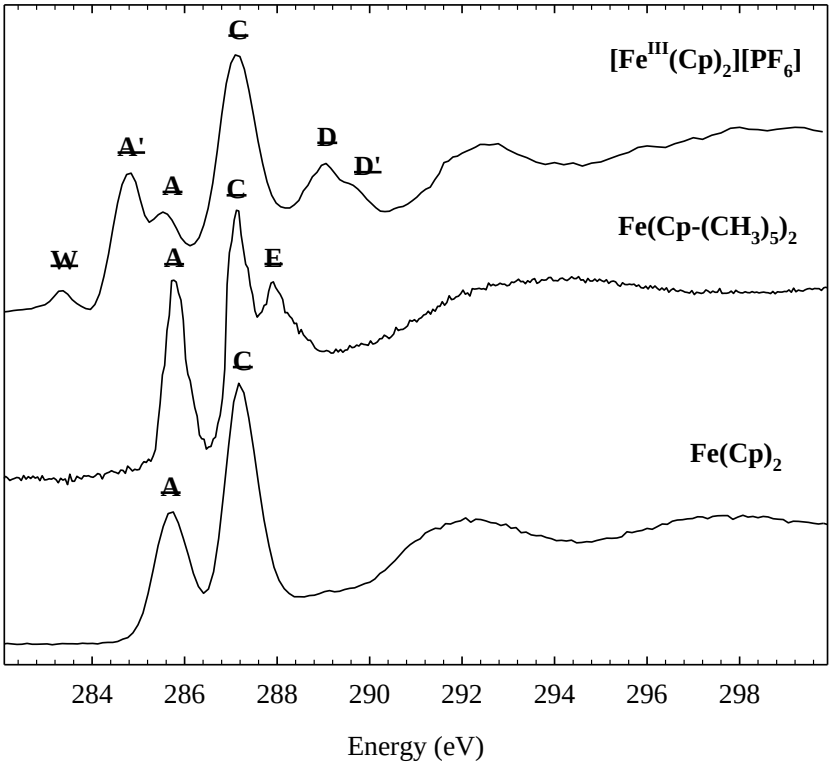

Figure 6.3 C 1s NEXAFS spectra of $[Fe^{III}(Cp)_2][PF_6]$, $Fe^{II}(Cp\text{-}(CH_3)_5)_2$ and $Fe^{II}(Cp)_2$.[6] The spectra have been offset by a constant for clarity.

Peak Labels	$Fe^{II}(Cp)_2$[6]	$Fe^{II}(Cp\text{-}(CH_3)_5)_2$	$[Fe^{III}(Cp)_2][PF_6]$	Assignments
W			283.35	3d / Cp π* SOMO
A'			284.81	Multiplet
A	285.72	285.81	285.54	3d / Cp π* (e_{1g})
C	287.19	287.14	287.12	Cp π* (localized by the core hole)
E		287.91		C1s→σ* (C-H)
D			289.04	Multiplet
D'			289.60	Multiplet

Table 6.4 Transition energies (eV) and Assignments for the C 1s NEXAFS spectra of $Fe^{II}(Cp)_2$,[6] $Fe^{II}(Cp\text{-}(CH_3)_5)_2$ and $[Fe^{III}(Cp)_2][PF_6]$. Transition energy values for $Fe^{II}(Cp)_2$ were reproduced from Wen *et al.*[17]

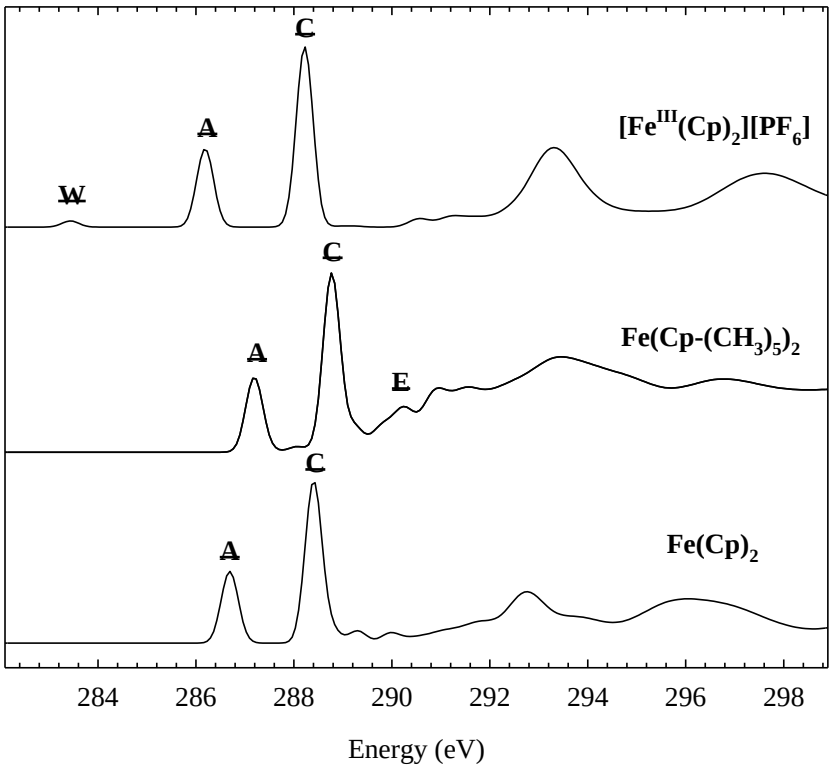

Figure 6.4 Simulated C 1s x-ray absorption spectra of $[Fe^{III}(Cp)_2][PF_6]$, $Fe^{II}(Cp\text{-}(CH_3)_5)_2$ and $Fe^{II}(Cp)_2$ calculated using DFT theory (StoBe program). The spectra have been offset by a constant for clarity.

Feature	$Fe^{II}(Cp)_2$	$Fe^{II}(Cp\text{-}(CH_3)_5)_2$	$[Fe^{III}(Cp)_2][PF_6]$
W			Fe $3d_{x^2-y^2}$ (e_{2g})
A	**Fe $3d_{xz}$ (e_{1g})**/Cp π*	**Fe $3d_{xz}$ (e_{1g}-like)**/Cp π*	**Fe $3d_{xz}$ (e_{1g})**/Cp π*
	Fe $3d_{yz}$ (e_{1g})/Cp π*	**Fe $3d_{yz}$ (e_{1g}-like)**/Cp π*	**Fe $3d_{yz}$ (e_{1g})**/Cp π*
C	Fe $3d_{x^2-y^2}$/**Cp π* (e_{2g})**	Fe $3d_{x^2-y^2}$/**Cp π* (e_{2g})**	Fe $3d_{x^2-y^2}$/**Cp π* (e_{2g})**
E		$\sigma^*_{(C\text{-}H)}$ CH_3	

Table 6.5 Assignment of StoBe simulated C 1s NEXAFS spectra of $Fe^{II}(Cp)_2$, $Fe^{II}(Cp\text{-}(CH_3)_5)_2$ and $[Fe^{III}(Cp)_2][PF_6]$. Localization of the molecular orbital on the metal or ligand is indicted by bold scripts.

The experimental C 1s NEXAFS spectra of $Fe^{II}(Cp)_2$ and $Fe^{II}(Cp\text{-}(CH_3)_5)_2$ are dominated by two peaks, labeled A and C. Our assignment of the C 1s spectrum of $Fe^{II}(Cp)_2$ is similar to previous assignments.[6] The DFT calculations show that lowest energy peak A is associated with two nearly-degenerate orbitals with Cp π* (e_{1g}) character mixed with the metal $3d_{xz}$ (LUMO) and $3d_{yz}$ (LUMO+1) orbital. The second strong feature labelled C

corresponds to a degenerate Cp π* orbital that is mostly localized on the Cp ring that contains the core excited carbon atom. We do not use the label e_{2g} for this state as the unoccupied molecular orbital is strongly localized to the Cp ring with the core hole. Feature E in the spectrum of $Fe^{II}(Cp\text{-}(CH_3)_5)_2$ is assigned to the C 1s → σ* (C-H) transition of the methyl group.

The experimental C 1s NEXAFS spectrum of $[Fe^{III}(Cp)_2][PF_6]$ is radically different from the C 1s NEXAFS spectrum of $Fe^{II}(Cp)_2$ and $Fe^{II}(Cp\text{-}(CH_3)_5)_2$. Specifically, a weak feature W is observed at low energy side, and a series of features are observed between 284 eV and 290 eV. A broad peak is observed above 292 eV.

The simulated C 1s NEXAFS spectrum of $[Fe^{III}(Cp)_2][PF_6]$ is similar to that of ferrocene and differs mostly by the presence of a low energy feature (W) assigned to the C 1s → SOMO transition, and a slight shift of features A and C to lower energy. The SOMO has Fe 3d (e_{2g}) character, as expected for $[Fe^{III}(Cp)_2][PF_6]$.[15,40,42] The C 1s DFT simulations reproduce the presence and the relative intensity of some features in the experimental spectrum (W, A and C), but the prominent features A', D and D' are not reproduced by DFT calculations.

The C 1s NEXAFS spectra simulated by DFT calculations are very effective at reproducing the experimental spectra of $Fe^{II}(Cp)_2$ and $Fe^{II}(Cp\text{-}(CH_3)_5)_2$, in particular the relative intensity of features A and C and the presence of C 1s → $\sigma_{C\text{-}H}$ character in $Fe^{II}(Cp\text{-}(CH_3)_5)_2$. This provides additional support for the conclusions drawn from our Fe 2p studies; that the spectra of closed shelled ferrocene species are dominated by covalent effects. In contrast, these DFT simulations are less effective at reproducing the C 1s spectrum of $[Fe^{III}(Cp)_2][PF_6]$; feature W is reproduced, but the shape of the rest of the π* band is not well reproduced. This results suggest that the C 1s spectrum of open shell $[Fe^{III}(Cp)_2][PF_6]$ is also sensitive to atomic multiplet effects, although the spectrum is clearly dominated by covalent π* transitions.

6.4 Conclusions

The goal of this study is to examine the applicability of the atomic multiplet model or the covalent bonding models for interpreting the NEXAFS spectra of metallocene species, in

particular ferrocene and ferrocenium. The strong covalent bonding between the iron atom and Cp rings suggests that covalent effects will be important in these NEXAFS spectra.

Our ability to successfully interpret the experimental spectra with EHMO and DFT calculations indicates that covalent bonding models are applicable for close shelled species. The following evidence indicates that covalent bonding models dominate the interpretation of the NEXAFS spectra of closed shelled ferrocene species:

- The similarity of the experimental C 1s and Fe 2p NEXAFS spectra of $Fe^{II}(Cp)_2$ and $Fe^{II}(Cp\text{-}(CH_3)_5)_2$ to the DFT and EHMO simulations and the dissimilarity of these NEXAFS spectra to the results of ligand field atomic multiplet calculations.[7]
- The observation of substituent effects in the Fe 2p NEXAFS spectra of substituted ferrocene molecules (e.g. Fe(Cp)(Cp-R), R = CH_3, COOH, $COCH_3$),[21] arising from covalent π-conjugation.

In contrast, these covalent bonding models are not effective in interpreting the spectra of open shelled species. In the case of $[Fe^{III}(Cp)_2][PF_6]$, the presence of additional features not reproduced by MO or DFT theory indicates that multiplet effects must be considered for $3d^5$ open shell systems.

Theory that can combine covalent bonding theory with atomic multiplet effects are required for the chemical characterization of covalently bonded organoiron species by NEXAFS spectroscopy. Recent developments in ligand field charge transfer methods provide some additional insight; however, the covalency is described in terms of a metal ↔ ligand charge transfer to form other atomic electronic configurations.[3,7] This method also relies on many adjustable parameters. This method forms alternative atomic configurations rather than a direct reflection of the covalent bonding, e.g. through shared electron density and orbital overlap between the metal and the ligand atoms. Fully relativistic configuration interaction calculations have been recently developed.[43,44] As these Dirac equation calculation use molecular orbitals, covalent effects are explicitly considered. Significant covalency effects were predicted for the V 2p NEXAFS spectrum of V_2O_3.[43] However, such methods have not yet been applied to organoiron compounds such as ferrocene and ferrocenium.

Our observations and conclusions are highly relevant for the accurate application of NEXAFS spectroscopy to chemical analysis. For example, in the Fe 2p spectra of an oxidized ferrocene functionalized self-assembled monolayers recorded by Himpsel at al, the low energy feature (W) was absent. This suggests that another iron species was present instead of the ferrocenium functionalized alkanethiols, as claimed by the authors.[12] The similarity of

their presumptive Fe^{III} spectrum with that of FeO(OH), a high spin oxide, supports an alternative interpretation where their sample decomposed prior to measurement, rather than the oxidative switching of the ferrocene group to ferrocenium.

Acknowledgements

This work is supported by Natural Sciences and Engineering Research Council, the Canadian Foundation for Innovation and the University of Saskatchewan. Spectroscopy measurements were performed at the Canadian Light Source, which is supported by NSERC, NRC, CIHR, and the University of Saskatchewan. We thank R.I.R. Blyth and T. Regier for their support on the CLS SGM beamline; C. Karunakaran, K. Kaznatcheev and M. Obst for their support on the Spectromicroscopy beamline; and R. Wilks for assistance with the DFT calculations.

6.5 References

(1) S.G. Urquhart, C.C. Turci, T. Tyliszczak, M.A. Brook, and A.P. Hitchcock, Organometallics **16**, 2080 (1997); S.G. Urquhart, A.P. Hitchcock, J.F. Lehmann, and M. Denk, Organometallics 17, 2352 (1998); E. I. Solomon and M.D. Lowery, Science 259 (5101), 1575 (1993).

(2) M.-A. Arrio, Ph. Sainctavit, Ch. Cartier dit Moulin, T. Mallah, M. Verdaguer, E. Pellegrin, and C.T. Chen, Journal of the American Chemical Society **118**, 6422 (1996).

(3) R.K. Hocking, E.C. Wasinger, F.M.F. De Groot, K.O. Hodgson, B. Hedman, and E.I. Solomon, Journal of the American Chemical Society **128**, 10442 (2006).

(4) E.I. Solomon, B. Hedman, K.O. Hodgson, A. Dey, and R.K. Szilagyi, Coordination Chemistry Reviews **249**, 97 (2005).

(5) A. P. Hitchcock, A.T. Wen, and E. Ruhl, Chemical Physics **147**, 51 (1990).

(6) E. Ruhl and A. P. Hitchcock, Journal of the American Chemical Society **111**, 5069 (1989).

(7) F. De Groot, Coordination Chemistry Reviews **249**, 31 (2005).

(8) G. Van der Laan, J. Zaanen, G.A. Sawatzky, R. Karnatak, and J.-M. Esteva, Physical Review B **33** (6), 4253 (1986).

(9) E.C. Wasinger, F.M. F. De Groot, B. Hedman, K.O. Hodgson, and E. I. Solomon, Journal of the American Chemical Society **125**, 12894 (2003).

(10) D.R. Van Staveren and N. Metzler-Nolte, Chemical Reviews **104**, 5931 (2004); H.B. Kraatz, Journal of Inorganic and Organometallic Polymers and Materials **15** (1), 83 (2005).

(11) D. Chen and J. Li, Surface Science Reports **61**, 445 (2006); M. Horie, T. Sakano, and K. Osakada, Journal of Organometallic Chemistry 691, 5935 (2006); Christoph Lambert, Volker Kriegisch, Andreas Terfort, and Bjorn Zeysing, Journal of Electroanalytical Chemsitry 590, 32 (2006).

(12) F. Zheng, V. Perez-Dieste, J.L. McChesney, Y.-Y. Luk, N.L. Abbott, and F.J. Himpsel, Surface Science **587**, L191 (2005).

(13) I. Manners, Synthetic Metal-Containing Polymers. (WILEY-VCH, Weinheim, 2004); A.S. Abd-El-Aziz and I. Manners, Journal of Inorganic and Organometallic Polymers and Materials **15** (1), 157 (2005).

(14) A.S. Abd-El-Aziz and E.K. Todd, Coordination Chemistry Reviews 246, 3 (2003); A.S. Abd-El-Aziz, E.K. Todd, and G.Z. Ma, Journal of polymer Science: Part A: Polymer Chemistry **39**, 1216 (2001); A.S. Abd-El-Aziz, E.K. Todd, R.M. Okasha, P.O. Shipman, and T.E. Wood, Macromolecules 38, 9411 (2005).

(15) R. Prins, Molecular Physics **19** (5), 603 (1970).

(16) K. Iwai, M. Iwai, K. Suto, S. Nakashima, I. Motoyama, H. Sano, I. Ikemoto, N. Kosugi, and H. Kuroda, Bulletin of the Chemical Society of Japan **59**, 2675 (1986); M.F. Ruiz-Lopez, M. Loos, J Goulon, M. Benfatto, and C.R. Natoli, Chemical Physics **121**, 419 (1988).

(17) A.T. Wen, E. Ruhl, and A. P. Hitchcock, Organometallics **11**, 2559 (1992).

(18) G. Fronzoni, P. Decleva, A. Lisini, and M. Ohno, Journal of Electron Spectroscopy and Related Phenomena **62**, 245 (1993).

(19) A. P. Hitchcock, Physica Scripta **T31**, 159 (1990).

(20) E. Ruhl, A.T. Wen, and A. P. Hitchcock, Journal of Electron Spectroscopy and Related Phenomena **57**, 137 (1991).

(21) Otero, E.; Wilks, R.; Regier, T.; Blyth, R. I. R.; Moewes, A.; Urquhart, S. G. Physical Chemistry A **112**, 624, (2008).

(22) R.G. Wilks, J.B. MacNaughton, H.B. Kraatz, T. Regier, and A. Moewes, Journal of Physical Chemistry B **110** (12), 5955 (2006).

(23) F.M.F. De Groot, J.C. Fuggle, B.T. Thole, and G.A. Sawatzky, Physical Review B **41** (2), 928 (1990).

(24) F. M. F. de Groot, J.C. Fuggle, B.T. Thole, and G.A. Sawatzky, Physical Review B **42** (9), 5459 (1990).

(25) T. Regier, J. Paulsen, G. Wright, I. Coulthard, K. Tan, T.K. Sham, and R.I.R. Blyth, presented at the Synchrotron Radiation Instrumentation: Ninth International Conference on Synchrotron Radiation Instrumentation, Daegu, Korea, 2006 (unpublished).

(26) B. Watts, L. Thomsen, and P.C. Dastoor, Journal of Electron Spectroscopy and Related Phenomena **151** (2), 105 (2006).

(27) J.T. Francis, C.C. Turci, T. Tyliszczak, G.G.B. De Souza, N. Kosugi, and A.P. Hitchcock, Physical Review A **52** (6), 4665 (1995).

(28) S.G. Urquhart, Adam P. Hitchcock, R.D Priester, and E.G. Rightor, Journal of Polymer Science: Part B: Polymer Physics **33**, 1603 (1995).

(29) Y. Ma, C. T. Chen, G. Meigs, K. Randall, and F. Sette, Physical Review A **44** (3), 1848 (1991).

(30) C. Mealli and D.M. Proserpio, Journal of Chemical Education **67** (5), 399 (1990).

(31) A. P. Hitchcock, S. G. Urquhart, and E. G. Rightor, Journal of Physical Chemistry **96** (22), 8736 (1992); A. P. Hitchcock, S. G. Urquhart, A. T. Wen, A. L. D. Kilcoyne, T. Tyliszczak, E. Ruhl, N. Kosugi, J. D. Bozek, J. T. Spencer, D. N. McIlroy, and P. A. Dowben, Journal of Physical Chemistry B **101** (18), 3483 (1997); S. G. Urquhart, A. P. Hitchcock, A. P. Smith, H. Ade, and E. G. Rightor, Journal of Physical Chemistry B **101** (13), 2267 (1997).

(32) C. P. Brock and Y. Fu, Acta Crystallographica Section B-Structural Science 53 (6), 928 (1997); A. Arrais, E. Diana, R. Gobetto, M. Milanesio, D. Viterbo, and P.L.

Stanghellini, European Journal of Inorganic Chemistry **6**, 1186 (2003); R. J. Webb, M. D. Lowery, Y. Shiomi, M. Sorai, R. J. Wittebort, and D. N. Hendrickson, Inorganic Chemistry **31** (25), 5211 (1992).

(33) W.H.E. Schwarz, Chemical Physics **11**, 217 (1975).

(34) B. Huo and A. P. Hitchcock, Simile2 (1996).

(35) M.O. Krause and J.H. Oliver, Journal of Physical and Chemical Reference Data **8**, 329 (1979).

(36) K. Hermann, L.G.M. Petterson, M.E. Casida, C. Daul, A. Goursot, A. Koester, E. Proynov, A. St-Amant, D.R. Salahub, V. Contributing authors: Carravetta, H. Duarte, C. Friedrich, N. Godbout, J. Guan, C. Jamorski, M. Leboeuf, M. Leetmaa, M. Nyberg, L. Pedocchi, F. Sim, L. Triguero, and A. Vela, StoBe Software, StoBe-DeMon Version 2.1 (2005).

(37) Y Ma, F. Sette, G. Meigs, S. Modesti, and C.T. Chen, Physical Review Letters. **63** (19), 2044 (1989).

(38) S.G. Urquhart, H. Ade, M. Rafailovich, J.S. Sokolov, and Y. Zhang, Chemical Physics Letters **322**, 412 (2000).

(39) G. Peng, J. Van Elp, H. Jang, L. Que, W.H. Armstrong, and S.P. Cramer, Journal of the American Chemical Society **117**, 2515 (1995); H. Wang, G. Peng, L.M. Miller, E.M. Scheuring, S.J. George, M.R. Chance, and S.P. Cramer, Journal of the American Chemical Society **119**, 4921 (1997).

(40) M.-M. Coutiere, J. Demuynck, and A. Veillard, Theoretical Chimica Acta **27**, 281 (1972); P.S. Bagus, U.I. Walgren, and J. Almlof, Journal of Chemical Physics **64** (6), 2324 (1976).

(41) R.F. Kirchner, G.H. Loew, and U.T. Mueller-Westerhoff, Theoretical Chimica Acta **41**, 1 (1976).

(42) R. Prins and F.J. Reinders, Journal of the American Chemical Society **91** (17), 4929 (1969); M.D. Rowe and A.J. McCaffery, Journal of Chemical Physics **59** (7), 3786 (1973).

(43) M.G. Brik, K. Ogasawara, T. Ishii, H. Ikeno, and I. Tanaka, Radiation Physics and Chemistry **74**, 1564 (2006).

(44) K. Ogasawara, T. Iwata, Y. Koyama, T. Ishii, I. Tanaka, and H. Adachi, Physical Review B **64**, 115413 (2001).

Supporting Information

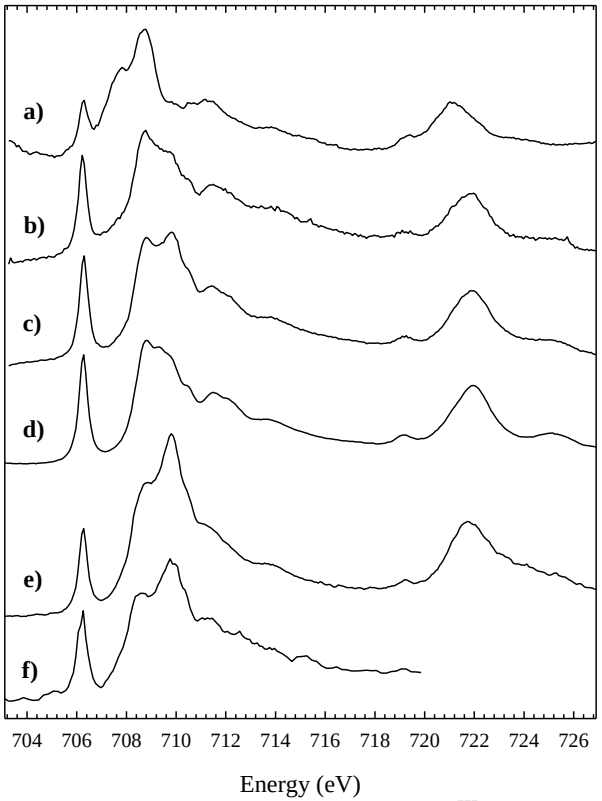

Figure 6.5 Fe 2p edges NEXAFS spectra of $[Fe^{III}(Cp)_2][PF_6]$ on different substrates and after various amounts of time.

Spectrum	Substrate	Elapsed time between sample preparation and measurement
a)	Indium foil	12 hours
b)	Indium foil	1 hour
c)	Indium foil	15 minutes
d)	Copper sheet	1 hour
e)	Carbon tape	1 hour
f)	Si_3N_4 window	6 hours

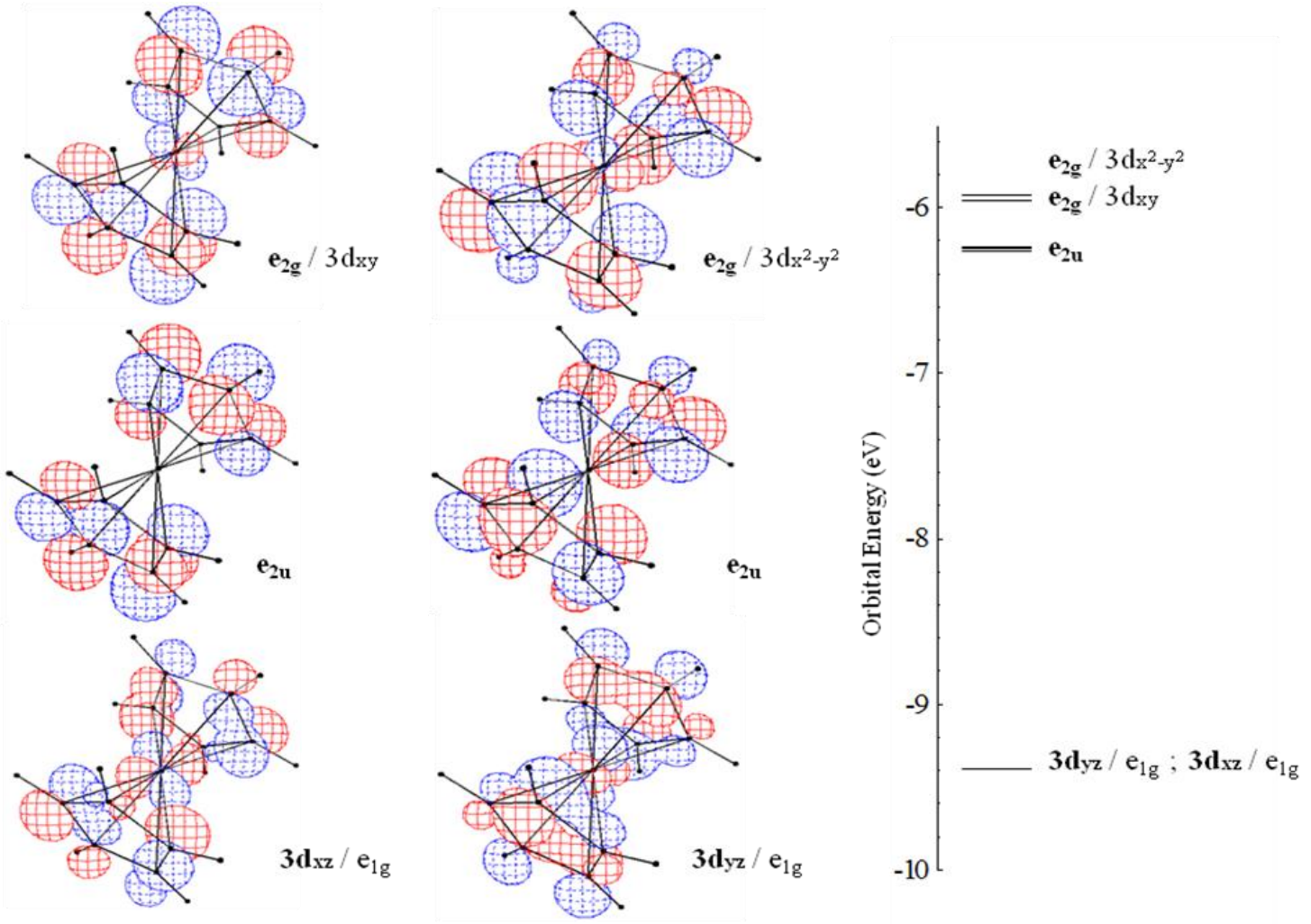

Figure 6.6 MO drawings generated from EHMO calculations using the program CACAO,[30] for the Fe 2p core excited state in $Fe^{II}(Cp)_2$, calculated using the Z+1 approximation.

CHAPTER 7 SUBSTITUENT EFFECTS IN THE IRON 2P AND CARBON 1S EDGE NEAR-EDGE X-RAY ABSORPTION FINE STRUCTURE (NEXAFS) SPECTROSCOPY OF FERROCENE COMPOUNDS.

Chapter 7 presents series of Fe 2p and C 1s edge NEXAFS spectra of closed shell substituted ferrocene complexes. The experimental spectra are assigned with the help of EHMO and DFT based computational programs. Both covalent bonding based programs simulate remarkably well the experimental spectra. Electron donating and withdrawing properties of the substituents leads to discreet shifts in energy while π^*-conjugation between substituent and cyclopentadiene ring leads to the presence of additional features. This study confirms the efficacy of the covalent bonding model over atomic multiplet effects in the interpretation of closed shell metallocene complexes spectra.

The experimental and theoretical work performed for this study is described and discussed below in the format of the manuscript published in the Journal of Physical Chemistry A. [Reproduced with permission from Journal of Physical Chemistry A, 112, E. Otero, R.G. Wilks, T. Regier, R.I.R. Blyth, A. Moewes and S.G. Urquhart, Substituent Effects in the Iron 2p and Carbon 1s Edge Near-Edge X-Ray Absorption Fine Structure (NEXAFS) Spectroscopy of Ferrocene Compounds, 624-634, Copyright 2008, American Chemical Society]

For this research paper I was the primary investigator in the conception of the study, the preparation of the samples, the acquisition of the experimental data, the execution of the computed simulations, the interpretation of the results and the writing of the document. R. Wilks provided indispensible support with the DFT calculations. T Regier and R.I.R. Blyth helped with the experimental set-up for the measurement of gaseous SF_6 used for energy scale calibration. S.G. Urquhart provided guidance throughout the experiments and data analysis process and was greatly involved in editing this document.

The following chapter has been published in the Journal of Physical Chemistry A, 2008, volume 112, pages 624-634.

DOI: 10.1021/jp074625w

CHAPTER 8 SUBSTITUENT EFFECTS IN THE IRON 2P AND CARBON 1S EDGE NEAR-EDGE X-RAY ABSORPTION FINE STRUCTURE (NEXAFS) SPECTROSCOPY OF METAL ARENE COMPLEXES AND POLYMER

Chapter 8 presents a series of Fe 2p and C 1s edge NEXAFS spectra of closed shell substituted metal arene complexes and polymers. The experimental spectra are assigned with the help of EHMO and DFT based computational programs. Both covalent bonding based programs simulate the experimental spectra remarkably well. Compared to ferrocene spectra, the substitution of one cyclopentadiene ring by a benzene ring leads to large changes in the principal spectral feature. Electron donating and withdrawing properties of the substituents on benzene affect the transition's energy while π^*-conjugation between substituent and benzene ring leads to the presence of additional spectral features. The experimental and theoretical work done for this study is described and discussed in the following section presented in the form of the manuscript to be submitted to the journal Organometallics.

For this research paper I was the primary investigator in the conception of the study, the preparation of the samples, the acquisition of the experimental data, the execution of the computed simulations, the interpretation of the results and the writing of the document.

P.O. Shipman and A.S. Abd-El-Aziz provided most of the metal arene compounds investigated in this study. S.G. Urquhart provided guidance throughout the experiments and data analysis process and was greatly involved in editing this document.

The following chapter has been published in the journal Organometallics, 2009, volume 28, pages 2160-2172.

DOI: 10.1021/om800769t

CHAPTER 9 NEAR-EDGE X-RAY ABSORPTION FINE STRUCTURE (NEXAFS) SPECTROSCOPY STUDY OF THE PHOTOLYTIC PROCESS IN POLY(PHENYL THIOETHER) WITH PENDANT IRON MOIETIES.

In **Chapter 9** we applied our understanding of metal-arene NEXAFS spectroscopy to interpret spectra of poly(phenyl thioether) polymers with and without pendent iron moieties (-Fe(Cp)). The Fe 2p NEXAFS spectrum of poly(phenyl thioether) indicates the presence of iron species trapped in the demetallated polymer. The photolytic study in solid phase of poly(phenyl thioeter)-Fe(Cp) shows that irradiation of the metallated polymer in air leads to formation of Fe_2O_3 while irradiation in vacuum leads to formation of iron species with lower oxidation state. Also, irradiation using different ultraviolet sources appears to have no significant effect on the outcome of the photolytic process in solid state. P 1s and P 2p NEXAFS spectra of poly(phenyl thioether) polymer indicated the presence of counter ion PF_6^- in the demetallated polymer. The characterization of iron and phosphorus species trapped in poyl(phenyl thioether) is discussed with respect to conducting and magnetic properties of these materials. The experimental and theoretical work done for this study is described and discussed in the following section presented in the form of the manuscript to be submitted to the journal Macromolecular Chemistry and Physics.

For this research paper I was the primary investigator in the conception of the study, the preparation of the samples, the acquisition of the experimental data, the interpretation of the results and the writing of the document. P.O. Shipman and A.S. Abd-El-Aziz synthesized the monomers and polymers investigated in this study. S.G. Urquhart provided guidance throughout the experiments and data analysis process and was greatly involved in editing this document.

The following chapter has been published in the journal Macromolecules, 2008, volume 41, pages 9532-9541.

DOI: 10.1021/ma801826p

CHAPTER 10 DISCUSSION AND CONCLUSION

The research described in this thesis demonstrate the complementarity of soft X-ray absorption spectroscopy and chemistry. In order to attempt to measure XNCD from small chiral organic molecules, tremendous progress in sample preparation and characterization has been made. On the other hand, the characterization of the organometallic polymers required improvement in the interpretation of NEXAFS spectra of transition metal complexes. For that reason, simpler systems, namely metallocene and meta arene compounds, were examined and the spectra were assigned with the help the EHMO and DFT calculations.

The first research objective was to observe the natural circular dichroism at X-ray wavelengths for small chiral organic molecules associated with the electric dipole - magnetic dipole interaction ($XNCD_{E1M1}$). Theoretical studies have estimated that for 1s absorption edge the intensity of $XNCD_{E1M1}$ does not exceed 10^{-3}, making it very difficult to observe. Additionally, this weak $XNCD_{E1M1}$ effect is expected to be observed only in amorphous samples while for oriented samples larger electric dipole – electric quadruple interferences dominate the process. Therefore a great amount of work has been invested in preparing randomly oriented samples. It was found that at a microscopic level, small chiral organic molecules (i.e.: less than 20 atoms) with low vapour pressure (required to satisfy the experimental conditions) have a great propensity to form oriented structures and were not suitable for $XNCD_{E1M1}$ measurements. Eventually amorphous thin films containing small chiral organic molecules were prepared using amino acid derivatives functionalized polymers.

In addition, considerable progresses in the data acquisition procedure were made in order to enhance spectral reproducibility, limit X-ray damage and lower noise levels.

Yet, despite the quality of the samples prepared and the outstanding spectra acquired, no $XNCD_{E1M1}$ measurement was successful. It is believed that the quality of the instrumentation at the time of the measurements was not sufficient enough for the timid $XNCD_{E1M1}$ effect sought.

The second research objective was to characterize a series of organometallic polymers and identify the products of the photolytic process aimed to remove the metallic fragment from metallated polymers. The assignment of NEXAFS spectra for transition metal complexes is quite difficult due to the complexity of the metal-ligand interactions. Two conflicting models are generally used, the atomic multiplet model and the covalent bonding

model. The examination of closed shell ferrocene and open shell ferrocenium compounds indicated that NEXAFS spectra of the former was effectively assigned using covalent bonding model while that of open shell ferrocenium suggested the contribution of multiplet effect as well. Studies of substituted ferrocene compounds confirmed the adequacy of the covalent bonding model to assign NEXAFS spectra of closed shell complexes. These findings were all supported by calculations.

Such advances in the understanding of the spectroscopy have thus allowed investigation of a series of substituted metal arene complexes and poly(phenyl thioether) and poly(phenyl ether) polymers with iron pendant groups. It was found that NEXAFS spectroscopy is moderately sensitive to the electron donating and withdrawing properties of the substituents on the arene ligand. On the other hand, the presence of characteristic resonances in several spectra were unambiguously assigned to π^*-conjugation between the substituent and the arene ligand. Such resonances were observed in the Fe 2p NEXAFS spectrum of poly(phenyl ether) polymers with iron pendant groups, suggesting electron delocalization between the arene and the oxygen bridging atom of the polymer back-bone. Again, all spectra assignments were supported by calculations.

Finally, the characterization of the products of the photolytic de-metallation process of poly(pheny thioether) with iron pendant groups indicated the presence of Fe_2O_3 and PF_6^- (counter ion in metallated polymer) embedded in the poly(pheny thioether) polymer in trace amounts.

The noteworthy outcomes of these studies were obtained because of the enhanced understanding of the spectroscopy achieved in part by the meticulous study of the metallocene and metal arene complexes.

Continuous improvement in core level excitation spectroscopy is the sequel of effective and concerted progress in instrumentation, theory and sample development.